



HAL
open science

Modelling and simulation of carbides in alpha-Fe alloys from first principles : alloying elements, diffusion and nucleation

Océane Buggenhoudt

► **To cite this version:**

Océane Buggenhoudt. Modelling and simulation of carbides in alpha-Fe alloys from first principles : alloying elements, diffusion and nucleation. Condensed Matter [cond-mat]. Université Paris-Saclay, 2021. English. NNT : 2021UPASP139 . tel-03565821

HAL Id: tel-03565821

<https://theses.hal.science/tel-03565821>

Submitted on 11 Feb 2022

HAL is a multi-disciplinary open access archive for the deposit and dissemination of scientific research documents, whether they are published or not. The documents may come from teaching and research institutions in France or abroad, or from public or private research centers.

L'archive ouverte pluridisciplinaire **HAL**, est destinée au dépôt et à la diffusion de documents scientifiques de niveau recherche, publiés ou non, émanant des établissements d'enseignement et de recherche français ou étrangers, des laboratoires publics ou privés.

Modelling and simulation of carbides in
 α -Fe alloys from first principles : alloying
elements, diffusion and nucleation

*Modélisation et simulation des carbures dans les alliages
de fer- α à partir des premiers principes : éléments
d'alliage, diffusion et germination*

Thèse de doctorat de l'université Paris-Saclay

École doctorale n° 576 : particules, hadrons, énergie et noyau :
instrumentation, imagerie, cosmos et simulation (PHENIICS)

Spécialité de doctorat : science des matériaux

Graduate School : Physique, Référent : Faculté des sciences d'Orsay

Thèse préparée dans l'unité de recherche **Service de Recherches de
Métallurgie Physique (Université Paris-Saclay, CEA)**, sous la direction de
Jean-Luc BÉCHADE, Directeur de recherche et le co-encadrement de
Chu-Chun FU, Docteur

Thèse soutenue à Paris-Saclay, le 17 décembre 2021, par

Océane BUGGENHOUDT

Composition du jury

Charlotte BECQUART

Professeure, Université de Lille

Philippe MAUGIS

Professeur, Université d'Aix-Marseille

Aurélie GENTILS

Directrice de recherche, Université Paris-Saclay

Jan WRÓBEL

Docteur, École polytechnique de Varsovie

Jean-Luc BÉCHADE

Directeur de recherche, Université Paris-Saclay

Chu-Chun FU

Docteur, Université Paris-Saclay

Présidente

Rapporteur & Examineur

Examinatrice

Examineur

Directeur de thèse

Co-encadrante

Titre : Modélisation et simulation des carbures dans les alliages de fer- α à partir des premiers principes : éléments d'alliage, diffusion et germination

Mots clés : Modélisation, Aciers, Carbures, Diffusion, Éléments d'alliage

Résumé : Les aciers faiblement alliés sont principalement constitués de fer et de carbone, avec quelques éléments d'alliage supplémentaires en faible quantité. Dans ces matériaux, des phases secondaires enrichies en carbone -des carbures- peuvent apparaître. La formation de carbures peut modifier radicalement les propriétés mécaniques des aciers. Elle peut par exemple favoriser l'apparition de fissures. En particulier, la présence de certains carbures dans les aciers ferritiques utilisés dans l'industrie nucléaire pourrait conduire à leur fragilisation. La cémentite (Fe_3C) et le carbure de molybdène Mo_2C sont deux carbures fréquents

dans les aciers. L'objectif de cette thèse est d'étudier les propriétés de ces deux carbures en utilisant la modélisation et des simulations numériques. Ces méthodes permettent d'aborder des données inaccessibles expérimentalement. Ainsi, nous avons étudié la diffusion du carbone dans la cémentite et comparé nos résultats avec des données expérimentales indirectes. Nous avons également quantifié les effets des éléments d'alliage sur les propriétés de la cémentite et du Mo_2C . De plus, nous avons développé une stratégie de modélisation afin d'étudier la précipitation de la cémentite.

Title : Modelling and simulation of carbides in α -Fe alloys from first principles : alloying elements, diffusion and nucleation

Keywords : Modelling, Steels, Carbides, Diffusion, Alloying-elements

Abstract : Low alloys steels are mainly made of iron and carbon, with additional alloying elements in low quantities. In these materials, secondary phases enriched in carbon -namely carbides- can appear. The formation of carbides can drastically change mechanical properties of steels. It may for example promote the appearance of cracks. In particular, the presence of carbides in ferritic steels used in the nuclear industry can raise some safety concerns. Cementite (Fe_3C) and the Mo_2C molybdenum carbide are two very common carbides in steels. The goal of this thesis is to investigate

properties of these two carbides via modelling and computer simulations. Various methods are useful to investigate atomic-scale properties that are difficult to access experimentally. This way, we studied carbon diffusion in cementite and compared with indirect experimental data. We also quantified effects of alloying elements on cementite and Mo_2C properties. Comparisons are made with experimental data available at this time. In addition, we developed a modelling approach in order to investigate the precipitation of cementite.

Resumé

La formation de carbures tels que le M_3C (cémentite) ou le M_2C peut affecter fortement les propriétés mécaniques des aciers. Ce phénomène a un impact significatif lorsque les aciers sont utilisés comme matériaux de structure pour diverses applications technologiques. En particulier, la présence de certains carbures dans les aciers ferritiques utilisés pour l'industrie nucléaire (par exemple les aciers de cuves des réacteurs à eau pressurisée 16MND5) pourrait conduire à leur fragilisation.

Les mécanismes d'agglomération et de diffusion du carbone ont un rôle essentiel lors des processus de nucléation et de croissance des carbures dans le fer- α , ou lors de la transition entre deux carbures de nature différente. Cependant, ces propriétés dépendantes de l'environnement chimique local sont encore mal connues. D'autre part, la présence d'éléments d'alliage (tels que le Mo, Cr ou Mn) dans les aciers peut favoriser la précipitation de certains types de carbures. Jusqu'à présent, beaucoup de choses restent encore peu ou mal connues sur les propriétés des carbures alliés.

L'objectif de cette thèse est d'aborder ces questions ouvertes, en utilisant des calculs basés sur la théorie de la fonctionnelle de la densité (DFT). Ce travail s'inscrit dans un projet multi-échelles basé sur un couplage entre théorie et expérience. Une attention particulière est donc portée sur la comparaison avec de nouvelles données expérimentales acquises dans le cadre de ce projet.

La première partie de la thèse est consacrée à l'étude de la diffusion du carbone dans la cémentite Fe_3C . En combinant les calculs des premiers principes avec des outils de physique statistique, nous avons déterminé les mécanismes de diffusion du carbone et les coefficients de diffusion associés dans la cémentite. Nous proposons une discussion approfondie sur les mécanismes de diffusion du carbone (C) dans la cémentite. Les coefficients de diffusion prédits dans Fe_3C sont en bon accord avec les mesures expérimentales du taux de carburisation dans les aciers ferritiques. L'effet d'un soluté de substitution (Mo, Cr ou Mn) dans la cémentite faiblement alliée sur la diffusivité du C est également étudié.

Dans un second temps, nous avons étudié les propriétés de la cémentite alliée et du carbure M_2C . Des calculs DFT ont été utilisés pour quantifier les effets du Mo, du Cr ou du Mn dans la cémentite et l'effet du Fe ou du Mn dans le M_2C . Nous nous sommes concentrés sur des propriétés comme le moment magnétique moyen ou le volume de ces carbures en fonction de la teneur en soluté. A partir des résultats DFT, nous avons également prédit la tendance à la (dé)mixion entre le soluté et les atomes de métal « hôte » dans le M_3C et le M_2C . La (dé)stabilisation de ces carbures par des éléments d'alliage a aussi été abordée. Nos résultats DFT sont confrontés avec les expériences et les données CALPHAD disponibles. De plus, nous avons discuté de l'effet du désordre magnétique et de l'entropie vibrationnelle sur les propriétés du M_3C et du M_2C .

Enfin, nous avons mis en place une stratégie de modélisation afin d'étudier la nucléation de la cémentite dans la ferrite. Nous avons d'abord identifié une structure Fe-C ordonnée, avec une organisation atomique similaire et la même stœchiométrie que la cémentite, mais avec des atomes de Fe résidant sur des sites de réseau cubique centré. En utilisant cette α -cémentite comme représentation du carbure de cémentite, nous avons paramétré des modèles d'interaction effective et de diffusion

à l'aide de données DFT afin d'effectuer des simulations Monte Carlo d'équilibre et de cinétique sur réseau pour l'étude de la précipitation de la cémentite dans le réseau α -Fe.

Abstract

The formation of carbides such as M_3C (cementite) or M_2C can drastically change mechanical properties of steels. This phenomenon has a fundamental impact when steels are used as structural materials for diverse technological applications. In particular, the presence of carbides in ferritic steels used in the nuclear industry (for example 16MND5 pressurized water reactor vessels steels) may cause some safety concerns.

Mechanisms of carbon agglomeration and diffusion play a central role in nucleation and growth processes of carbides in α -Fe, or on the transition from a carbide to another. However, these local-environment dependent properties are still poorly known. The presence of alloying elements (such as Mo, Cr or Mn) in steels can promote the precipitation of carbides. So far, very little is known about properties of alloyed carbides.

The objective of this thesis is to investigate some of these open questions, employing density functional theory (DFT) based calculations. This work is part of a multi-scale and coupled experimental-theoretical project. A particular attention is therefore paid to a comparison with the new experimental data acquired in this frame.

The first part of the thesis is dedicated to the study of carbon diffusion in Fe_3C cementite. Combining first principles calculations with statistical physics tools, we determined carbon diffusion mechanisms and the resulting diffusion coefficients in cementite. We provide an in-depth discussion regarding the mechanisms for carbon (C) diffusion in cementite. The predicted diffusion coefficients in Fe_3C are in good agreement with experimental measurements of carburization rate in ferritic steels. The effect of a substitutional solute element (Mo, Cr or Mn) in weakly-alloyed cementite on C diffusivity was also investigated.

Then, we studied the properties of alloyed cementite and the M_2C carbide. We used DFT calculations to quantify the effects of Mo, Cr or Mn alloying in cementite and the effect of Fe or Mn alloying in M_2C . We focused on properties such as the average magnetic moment or the volume of these carbides as functions of the solute content. Based on the DFT results, we also predicted the (un)mixing tendency between the solute and the host metal-atoms in M_3C and M_2C , as well as the (de)stabilization of these carbides upon alloying. A link is made between our DFT results and experiments and available CALPHAD data. In addition, we discussed the effect of magnetic disorder and vibrational entropy on the M_3C and M_2C properties.

Finally, we implemented a modelling approach in order to investigate the nucleation of cementite in ferrite. We first identified an ordered Fe-C structure, with similar atomic organization and the same stoichiometry as the cementite, but with Fe atoms residing on bcc-lattice sites. Employing this α -cementite as a representation of the cementite carbide, we parameterized effective-interaction and diffusion models using DFT data in order to perform equilibrium and kinetic on-lattice Monte Carlo simulations for the study of cementite precipitation in the α -Fe lattice.

Acknowledgements

First of all, I would like to thank the reviewers of this thesis, Charlotte Becquart and Philippe Maugis, for their time spend reading my work and for their insightful comments. I would also like to express my gratitude to Aurélie Gentils and Jan Wróbel for being part of my jury. I really appreciated our discussion.

I am extremely gratefully to my supervisor, Chu-Chun Fu, who introduced me to a whole new field of research when I knew almost nothing about carbides and DFT calculations. Thank you for all your time, all your advises and your patience. You always encouraged me to search further, dig deeper into my results, and I will really miss our discussions.

I would also like to express my deepest thanks to my thesis director and head of SRMP, Jean-Luc Béchade. Thank you for your support, for your very clear explanations regarding experimental procedures and for your time spent reviewing this manuscript. (And thank you for always encouraging me to run to relieve some stress.)

I am also very grateful to Thomas Schuler and Frédéric Soisson for their expertise and advises which contributed a lot to this work. Both of you, thank you for all the time you spent answering my many, many questions.

This thesis is part of a multi-scale and coupled project between applied metallurgy and fundamental researches. I therefore would like to acknowledge the work of the experimental team involved in this joint project. In particular, thank you to Anna Benarosch and Caroline Toffolon for all the stimulating discussions. Thank you also to Estelle Meslin, Bernard Marini and Ivan Guillot.

Thank you to everyone within the SRMP for their kindness and for all the good moments. I really enjoyed our meals together and the occasional discussions in the 'salle café'. Especially, thank you to Marie for our regular running outings and to Clovis for keeping me company when I was working late. Thank you to Fabrice -Kangming- for his help and our very interesting talks. I am also thankful to Elric and Anton, the first PhD students that I met at the SRMP, and who taught me a lot of things during my first weeks here.

Lastly, my deepest thanks goes to my family and especially my parents for their unconditional support. Shout out to my sister Lénora who proofread this manuscript while preparing her 'baccalauréat'. Maybe I'll do the same for you one day ?

Contents

Introduction	1
1 Methods	5
1.1 Density Functional Theory calculations	5
1.1.1 Principle	5
1.1.2 Calculation details	8
1.1.3 Kinetic cluster expansion (KineCluE)	10
1.2 Monte-Carlo Simulations	13
1.2.1 Principle	13
1.2.2 Metropolis Algorithm	14
1.2.3 Residence Time Algorithm	14
1.3 CALPHAD	15
2 Fe₃C cementite: point defects and diffusion.	17
2.1 State of the art	17
2.2 Stoichiometric Fe ₃ C	19
2.3 Point defects in Fe ₃ C	20
2.3.1 Vacancies in Fe ₃ C	20
2.3.2 C interstitials in Fe ₃ C	22
2.3.3 C Frenkel pairs in cementite	24
2.4 C diffusion in Fe ₃ C	25
2.4.1 C diffusion mechanisms and associated energy barriers	25
2.4.2 Determination of C diffusion coefficients	26
2.5 Effect of an alloying element on C interstitial diffusion in cementite	31
2.5.1 Interaction between an alloying element (Mo,Cr,Mn) and a C interstitial	31
2.5.2 C migration barrier in the vicinity of an alloying element	37
2.5.3 Effects of the substitutional solutes on C diffusion in cementite	39
2.6 Summary	41
3 Alloyed M₃C and M₂C carbides: structural, energetic, electronic and magnetic properties	43
3.1 State of the art	43
3.2 Interaction between Mo, Cr or Mn solutes in ferrite	44
3.3 Structural, magnetic and energetic properties of Mo, Cr or Mn alloyed cementite	46
3.3.1 Magnetism of Mo, Cr or Mn alloyed cementite	46
3.3.2 Volume of Mo, Cr or Mn alloyed cementite	51
3.3.3 Binding enthalpies between Mo, Cr or Mn atoms in cementite	53
3.3.4 Mixing enthalpy of Mo, Cr or Mn alloyed cementite	54
3.3.5 Enthalpy of substitution of Mo or Mn in Fe ₃ C	57
3.4 Structural, magnetic and energetic properties of Fe or Mn alloyed M ₂ C	58
3.4.1 Stoichiometric Mo ₂ C	58

3.4.2	Magnetism of Fe or Mn alloyed Mo_2C	61
3.4.3	Volume change in Fe or Mn alloyed Mo_2C	61
3.4.4	Binding enthalpy between Fe or Mn solutes in Mo_2C	62
3.4.5	Mixing enthalpy of Fe or Mn alloyed M_2C	63
3.4.6	Enthalpy of substitution of Fe or Mn in Mo_2C	65
3.5	Partitioning of Fe, Mo and Mn between M_3C and M_2C	65
3.6	Magnetic disorder and vibrational entropy at finite temperatures . . .	66
3.7	Summary	67
4	Modelling approach for the nucleation of cementite	71
4.1	State of the art	71
4.2	An ordered Fe-C structure for the representation of cementite in a bcc lattice: α -cementite	72
4.3	Effective interaction model (EIM) for carbon interactions and precipitation in ferrite	75
4.3.1	DFT calculations	75
4.3.2	Parameterization of the EIM from DFT data	77
4.3.3	Equilibrium properties	80
4.3.3.1	Characterization of the precipitates	80
4.3.3.2	Interface energy	81
4.3.3.3	Solubility limit of C in the matrix in equilibrium with α -cementite	82
4.4	Kinetics of α -cementite nucleation	83
4.4.1	C diffusion model in ferrite	83
4.4.2	Kinetic Monte-Carlo simulations	86
4.5	Summary	87
	Conclusions and perspectives	89
	Synthèse en français	93
	Bibliography	99

List of Abbreviations

AF	AntiFerromagnetic
BCC	Body-Centered Cubic
CALPHAD	CAL culat ion of PHA se Diagramms
CASTEP	CAM bridge SER ial TOT al EN ergy PA ckage
CEA	Com missariat à l'Énergie AT omique et aux Énergies AL ternatives
CPU	CE ntral P rocessing U nit
DACAPO	DFT software
DFT	D ensity F unctional T heory
ECEC	É tude A mont sur la C inétique d'Évolution des C arbures
EDS	E nergy D ispersive X -ray S pectroscopy
EIM	E ffective I nteraction M odel
FM	F erro M agnetic
GGA	G eneralized G radient A pproximation
GPAW	DFT software
HCP	H exagonal- C losed P acked
KineCluE	K inetic C luster E xpansion
KMC	K inetic M onte C arlo
LDA	L ocal D ensity A pproximation
MC	M onte- C arlo
MD	M olecular D ynamic
MEP	M inimum E nergy P ath
MIS	M etastable I ntermediate S tructure
NCPP	N orm C onserving P seudo- P otential
NEB	N udget E lastic B and
NM	N on- M agnetic
inn	N earest N eighbor (-ith)
Octa	O ctahedral
OR	O rientation R elationship
OS	O rdered S tructure
PAW	P rojected A ugmented W ave
PBE	P erdew- B urke- E ruzerhof
Pct	c onstant P ressure
PHONOPY	o pen source package for phonon calculations at harmonic and quasi-harmonic levels
PWR	P ressurized W ater R eactor
QE	Q uantum E spresso
RSPt	R elativistic S pin P olarized toolkit
RTA	R esidence T ime A lgorithm
SCMF	S elf- C onsistent M ean- F ield
SIESTA	S panish I nitiative for E lectronic S imulations with T housands of A toms
SQS	S pecial Q uasi- R andom S tructure
T1, T2, T3	n on-equivalent T etrahedral sites
TCFE	T CS S teel and F e- A lloys D atabase
TEM	T ransmission E lectron M icroscopy

USPP	Ultra-Soft Pseudo-Potential
VASP	Vienna Ab-Initio Simulation Package
Vct	constant Volume
wrt	with respect to

To my parents.

Introduction

Among materials, steels are iron-carbon based alloys that display useful properties and admit a wide range of applications. The addition of distinct alloying elements can significantly modify the properties of steels. Thus, the composition of a given steel is directly related to its intended use. In the nuclear industry, 16MND5 to 20MND5 steels are used for large components of the primary circuit of Pressurized Water Reactors (PWR), such as the reactor vessel, the pressurizer, or the steam generator. A schematic view of the PWR vessel is given Fig. 1. For safety and efficiency reasons, these materials should present appropriate mechanical properties and be sufficiently resistant to thermal aging and neutron irradiation. Also, each component must be as homogeneous as possible.

16MND5 steel is found in the vessel of PWRs. Its composition is given in Table. 1. Sulphur (S) and Phosphorus (P) are impurities. Low S and P concentrations steels show a better resistance to ductile fracture. In addition, low P concentrations increases the toughness in areas with large grain sizes. To prevent ductile tearing, the concentration of these impurities must be reduced to a minimum. The addition of Chromium (Cr), Manganese (Mn), Molybdenum (Mo), Nickel (Ni), Tungsten (W), Vanadium (V) and Titanium (Ti) hardens the ferritic phase [75]. Elements such as Mn, Si or Al can form oxides and neutralize oxygen. Mn also forms manganese sulphide (MnS) that acts as nucleation site for ductile fracture [21], effectively reducing the ductility. Cr is used to prevent corrosion, while Ni hardens steel and makes it resistant to failure [24]. The strong attraction between Mo and P can be used to control embrittlement caused by P segregation at the grain boundary. More importantly, carbon concentration strongly affects steels toughness. Increasing C concentration reduces steels toughness and leads to a higher ductile-brittle transition temperatures [158]. It also increases steels hardness and tensile strength. As a result, carbon concentrations above the required value (0.22 wt%) can cause issues.

TABLE 1: Composition of 16MND5 steel (values in wt%).[201]

C (max)	S (max)	P (max)	Mn	Si	Ni
0.22	0.008 or 0.012	0.008 or 0.020	1.15 to 1.60	0.15 to 0.30	0.5 to 0.85
Cr (max)	Mo	V (max)	Al (max)	Co (max)	Cu (max)
0.25	0.43 to 0.60	0.01	0.04	0.03	0.08 to 0.20

The 16MND5 steel has a bainitic structure. Bainite is an out of equilibrium state and a mixture of ferrite -a phase with a body-centered cubic (bcc) crystal structure- and cementite carbide (Fe_3C). In the presence of alloying elements, other carbides can also form in bainite. During the manufacturing process, this steel undergoes several heat treatments. It is first heated at 875°C to obtain austenite -a phase with a face-centered cubic (fcc) crystal structure- and quenched in water in controlled conditions. This process induces the formation of bainite. In order to get rid of any remaining austenite and prevent the occurrence of internal stresses, the bainite

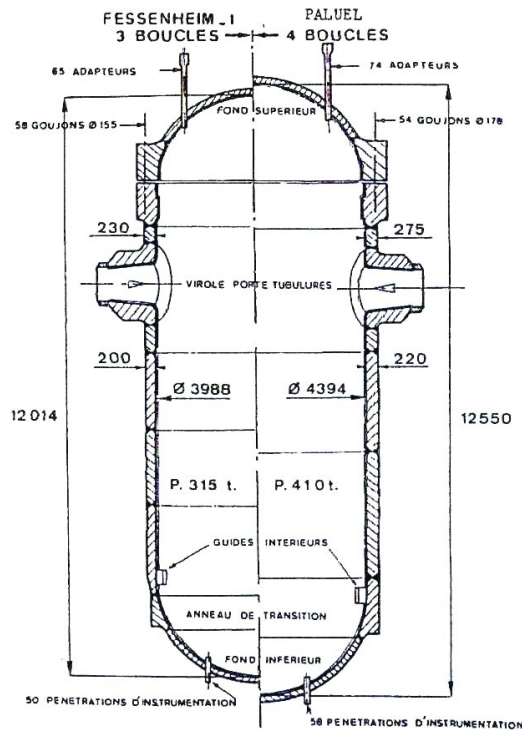


FIGURE 1: Schematic view of a PWR vessel.

is then tempered between 650°C and 700°C (depending on the grade) and cooled slowly. However, the thickness of the vessel parts (up to approximately 20 cm) may generate temperature gradient upon cooling, therefore producing an heterogeneous material. For example, it can lead to the emergence of C-rich phases and thus promote the formation of carbide phases.

The tempering can affect carbides already present in the bainite, or facilitate the precipitation of new carbides. This step plays a crucial role on the mechanical properties because it modifies significantly the steel microstructure. Bainitic 16MND5 structure have been studied after tempering by means of optical microscopy and extractive replica [73]. According to this study, cementite is located between ferrite laths, either as elongated particles or in a spherical form. Needle-shaped, M_2C molybdenum-rich carbides are also present within the laths. Cementite carbide (M_3C) admit an orthorhombic structure [44]. Cementite metallic contents is mainly iron, but alloying elements such as Mn, Mo or Cr can also be found [124, 182]. Depending on the temperature and the time of the tempering, cementite carbides can be elongated or spherical. M_2C carbides admit an orthorhombic [31, 73, 155] or a hexagonal structure [22, 115]. Their Mo concentration is very high, they are therefore often called Mo_2C . Other carbides could appear in steels with Mo, Mn or Cr and are worth mentioning. Face-centered cubic M_6C carbide [6, 99] is also rich in Mo, and might also contain some Fe or Cr. In the presence of Mo, its composition varies between Fe_4Mo_2C and Fe_3Mo_3C [99]. This carbide is either lenticular or globular shaped. M_7C_3 carbides are orthorhombic [25, 85] and can precipitate with Cr, Mn and Fe [131]. $M_{23}C_6$ often contains only Cr ($Cr_{23}C_6$), only Mn ($Mn_{23}C_6$) but also Cr and Mn ($(Mn,Cr)_{23}C_6$). It can also be made of Fe and a small quantity of Mo ($Fe_{21}Mo_2C_6$) [53, 185]. However, this $M_{23}C_6$ carbide preferentially precipitates for C concentration higher than the 16MND5 one. For long tempering times, hexagonal MoC carbides [151] can

also precipitate, as well as M_aC_b carbide [152]. M_aC_b , also called ξ -carbide or Kuo carbide, can be alloyed with Mo and form $(Fe,Mo)_3C$ with an orthorhombic [40] or monoclinic [200] crystal structure. Please note that this carbide is different from cementite (they have very different lattice parameters). The precipitation of carbon into carbides during the tempering modifies the mechanical properties of the steel. For example, small intra-granular carbides such as M_2C harden steel. On the other hand, big carbides located at grain boundaries are possible starting points for the brittle and ductile fracture.

16MND5 steels are used for the vessel of Flamanville 3, the third-generation PWR of Flamanville power plant located in Normandy (France). However, required toughness was not achieved for the closure head. According to FRAMATOME (formerly known as Areva), the company in charge of the PWR construction, this difference is due to the presence of areas with local carbon enrichment. In these segregated areas, the carbon concentration can reach up to 0.28 wt% [197, 199] and increases by approximately 50% with respect to the carbon content. This is not an isolated occurrence: recent studies also reported a higher carbon concentration than the required values in the bottom of steam generators made of 18MND5 steel [198]. As a result, a series of appraisals on sacrificial parts was launched. Meanwhile, little is known on segregation, in particular regarding the kinetics of carbides precipitation, carbides properties, nucleation mechanisms of carbides, etc. ... This is why the Commissariat à l'Énergie Atomique et aux Énergies Alternatives (CEA) started a research program to investigate the kinetics of carbides evolution and its impact on the mechanical properties of bainitic steel. This program is divided into two main axis: (i) a study in the manufacturing conditions (especially during tempering) and (ii) a study in operating conditions (in particular under irradiation).

This thesis is part of a multi-scale and coupled project between applied metallurgy and fundamental researches called ECEC (Étude amont sur la Cinétique d'Évolution des Carbures). ECEC project falls within the first axis of CEA research program introduced in the previous paragraph. Its goal is to better understand the link between the steel microstructure and its mechanical properties, starting with simplified systems (model steels). To that end, two thesis were initiated in 2018. The first one, conducted by Anna Benarosch, is based on an experimental approach, coupled with semi-empirical modeling (CALPHAD calculation) in order to build a thermokinetic model for the evolution of carbide precipitation in bainitic steels. This study was carried out on simplified model steels such as ternary Fe-C-Mo alloys or quaternary Fe-Mo-Mn-C alloys. Nonetheless, a lot of fundamental data are difficult or downright impossible to access experimentally. In particular, the volume fraction of carbides is small and difficult to isolate from the surrounding matrix. In addition, it is extremely challenging to observe directly atomic-scale phenomena such as diffusion, nucleation or property changes induced upon alloying in carbides phases. Computational modelling tools can be used to investigate such properties. For example, the structural, magnetic, electronic and elastic properties of cementite [13, 28, 35, 43, 60, 62, 79, 80, 117, 133], as well as Mo_2C [59, 71, 84, 110, 148, 161, 204, 209] (to cite a few works) have been extensively studied using density functional theory (DFT). However, many properties of these carbides are still unknown. In particular, mechanisms of carbon agglomeration and diffusion play a central role in nucleation and growth processes of carbides in α -Fe, or on the transition from a carbide to another. These local-environment dependent properties are still poorly known. Also, the presence of alloying elements (such as Mo, Cr or Mn) in steels can promote the

precipitation of carbides. So far, very little is known about properties of alloyed carbides. Therefore, the goal of this thesis is to investigate these open questions. To this end, we mainly employed DFT calculations coupled with statistical modelling. The modelling methods used during this thesis are presented in Chapter 1. This thesis work can be separated into three different subtopics. A detailed state of the art is given at the beginning of Chapter 2, Chapter 3 and Chapter 4.

In Chapter 2, we studied various point defects in Fe_3C cementite. Based on this knowledge, we investigated C migration mechanisms and determined C diffusion coefficients in Fe_3C and weakly-alloyed $(\text{Fe}_{1-x}\text{M}_x)_3\text{C}$ (with $\text{M} = \text{Mo}, \text{Mn}$ and Cr which are common alloying elements in ferritic steels). The predicted coefficients are compared with experimental data obtained indirectly through carburization experiments. In the weakly-alloyed cementites, we discuss the effect of a substitutional solute on C diffusion.

The goal of Chapter 3, is to investigate in detail several properties of alloyed cementite $(\text{Fe}_{1-x}\text{M}_x)_3\text{C}$ and $(\text{Mo}_{1-x}\text{M}_x)_2\text{C}$ with a wide range of alloying concentrations. We mostly focus on the effect of Mo and Mn alloying in cementite, as well as Fe and Mn alloying in $(\text{Mo}_{1-x}\text{M}_x)_2\text{C}$ because Mo and Mn are common alloying elements in ferritic steels. The enthalpy of substitution is used to predict the partitioning behavior of Mo, Mn and Fe between cementite, Mo_2C and ferrite. The effect of the vibrational entropy and the magnetic disorder at finite temperature is discussed. In this chapter, special attention is given to the comparison between DFT predictions and experimental data (from literature and obtained during Anna Benarosch's thesis).

In the last chapter (Chapter 4), we implemented a modelling approach in order to investigate the nucleation of cementite in ferrite. We first identified an ordered Fe-C structure, with similar atomic organization and the same stoichiometry as cementite, but with Fe atoms located on bcc-lattice sites. Employing this α -cementite as a representation of the cementite carbide, we parameterized effective-interaction and diffusion models using DFT data in order to perform equilibrium and kinetic on-lattice Monte Carlo simulations for the study of cementite precipitation in the α -Fe lattice.

In this introduction, we advertise the critical role of carbides in steels with a very specific case related to the nuclear industry. While this specific case is the motivation behind this thesis, carbides can also be found in a wide range of steels. For example, cementite is ubiquitous in low, medium and even high carbon steels. It can be found in carbon steels but also (white) cast iron or pearlitic steel wires. More surprisingly, cementite appears in meteorites that have cooled at a few degree per million year, or deep into the Earth core. A few studies also indicate that nanoparticules of cementite may be useful for the site-specific delivery of healing drugs. As for Mo_2C carbides, they display interesting catalytic properties. In particular, orthorhombic Mo_2C is a possible substitute for commercial Cu-based catalysts.

Chapter 1

Methods

In this chapter, we introduce the main tools used within this thesis. In particular, the fundamentals of Density Functional Theory calculations and Monte Carlo simulations are summarized. We also describe some specific methods and computational details. Finally, we give the expression of various physical quantities that will be used in the following chapters.

The goal of material modelling is to understand and predict with accuracy the key-properties of materials, using physical models and computational tools. It includes a wide range of techniques and applications, from atomistic simulations to finite elements methods. Since each method is usually limited to a given size and time scale, it can be of interest to combine complementary approaches in a multi-scale study.

During this thesis, density functional theory calculations were performed in order to quantify the energetic, electronic and magnetic properties of various systems. Some of the obtained data were combined with statistical tools in order to predict diffusion coefficients, while others were used to parameterize an effective interaction model in order to study the nucleation of cementite using Monte Carlo simulations. Our results are compared with experimental data, as well as CALPHAD data (if available). As explained in the introduction, particular attention is given to the comparison with Anna Benarosch experimental data (private communication within the ECEC project). The purpose of this chapter is to introduce the methods and technical features applied within this thesis.

1.1 Density Functional Theory calculations

1.1.1 Principle

In order to understand the properties of materials at the atomic scale, the first step is to acknowledge that they may be seen as a complex arrangement of electrons and nuclei. In 1926, Schrödinger discovered that in order to understand the behavior of a quantum particle, one needs to determine the corresponding wavefunction $\psi(r)$ for every point r in space, by solving the Schrödinger equation. For the case of stationary electronic states of a system, the Schrödinger equation is reduced to its time-independent form:

$$\hat{H}\psi = E\psi, \tag{1.1}$$

with \hat{H} the Hamiltonian operator and E the energy eigenvalue of the stationary state described by ψ . In the case of a set of atoms -i.e. many electrons and nuclei together-, we must introduce the many-body wavefunction Ψ depending on the positions of each electron and nucleus of the system. In the case of a system with N electrons with coordinates r_1, r_2, \dots, r_N and M nuclei of coordinates R_1, R_2, \dots, R_M , we have:

$$\Psi = \Psi(r_1, r_2, \dots, r_N; R_1, R_2, \dots, R_M) \quad (1.2)$$

Replacing ψ by Ψ in Eq. 1.1, we obtain the many-body Schrödinger equation:

$$\hat{H}\Psi = E\Psi, \quad (1.3)$$

The many-body Hamiltonian can be decomposed into the kinetic and potential energies contributions:

$$\hat{H} = \hat{T}_e + \hat{T}_n + \hat{V}_{ee} + \hat{V}_{nn} + \hat{V}_{en}, \quad (1.4)$$

with \hat{T}_e and \hat{T}_n the kinetic energy of the electrons and nuclei, and with \hat{V}_{ee} , \hat{V}_{nn} and \hat{V}_{en} the electron-electron, nuclei-nuclei and electron-nuclei Coulomb interaction potential, respectively. In order to calculate the equilibrium properties of materials, we must solve this many-body Schrödinger equation and determine the eigenstate with the lowest energy -the *ground state* - of the system. However, with the exception of very simple systems, the resolution of this equation remains extremely challenging.

In order to solve this issue, many approximations have been introduced. Firstly, nuclei are far heavier and slower than the electrons. While in gases, liquids or plasma, the nuclei may travel long distances, in the case of solids, the nuclei remains at or near fixed positions. The Born Oppenheimer -or *clamped nuclei*- approximation consists in considering the nuclei as immobile (clamped). This approximation is particularly relevant in the case of metallic crystals where the nuclei positions can be provided through X-ray crystallography. This approximation implies that we can neglect the kinetic energy of the nuclei \hat{T}_n , and that the repulsion between nuclei \hat{V}_{nn} is a constant in Eq. 1.4. However, even within this approximation, a N-electrons system is still too complicated to solve.

In 1964, Hohenberg and Kohn [69] established the basics of Density Functional Theory (DFT) by reformulating the N-body problem in terms of the electronic density. The Hohenberg and Kohn theorems state that:

(i) the ground state energy of a many electron system is a unique functional of the electron density $n(r)$:

$$E = F[n] \quad (1.5)$$

(ii) the ground state energy can be obtained variationally: the electron density that minimises the total energy is the ground state electron density. However, these theorems do not give any indication on how to built such functional.

In 1965, Kohn and Sham [94] proposed an expression for the total energy of the system by breaking down the unknown Hohenberg and Kohn functional into the sum of known energy contributions of the independent electrons (including the external potential, the kinetic energy and the Hartree energy), and an unknown contribution called the exchange correlation energy E_{xc} containing everything left out. The Kohn-Sham energy E_{KS} is thus written:

$$E_{KS}[n] = \underbrace{\int dr n(r) V_n(r) + T[n] + E_H[n] + E_{nn} + E_{xc}[n]}_{\text{known contributions}}, \quad (1.6)$$

with V_n the Coulomb potential of the nuclei or any external source experienced by the electrons, T the kinetic energy of the independent electrons and E_{nn} the constant nuclei-nuclei Coulomb interaction energy. The Hartree energy E_H arises from the Coulomb repulsion between independent electrons using classical electrostatics:

$$E_H[n] = \frac{1}{2} \int d^3r d^3r' \frac{n(r)n(r')}{|r-r'|}. \quad (1.7)$$

DFT allows us to calculate the Kohn-Sham energy using a self-consistency scheme. For a given system of atoms, we propose an initial electron density $n(r)$. A simple choice for the initial electron density is often the linear combination of the densities of the corresponding isolated atoms, but arranged into the atomic positions of our system. The Kohn-Sham equation is solved in order to obtain the associated set of wavefunctions. The obtained wavefunctions are then used to update the electron density. The process is repeated until we achieve the self-consistency, i.e. until the new density matches the previous one within an accepted convergence.

As the exchange and correlation functional $E_{xc}[n]$ remains unknown, we must rely on approximate functionals. The simplest and widely used functional is the *Local Density Approximation* (LDA). LDA is based on a homogeneous electron gas model [36], and only depends on the value of the electron density for each point in space:

$$E_{xc}^{LDA}[n] = \int n(r) \epsilon_{xc}[n] dr, \quad (1.8)$$

with ϵ_{xc} the exchange correlation energy per particle of a homogeneous electron gas of charge density n . However, DFT calculation using LDA do not predict the ferromagnetic ground state of pure body-centered cubic (bcc) iron as observed experimentally [207, 221]. Therefore, LDA cannot be trusted for the study of iron-based alloys. Another widely-used functional is the *Generalized Gradient Approximation* (GGA). GGA takes into account the heterogeneity -the variation of the local electron density- of the electron gas. The exchange correlation energy depends on the local electronic density, but also on the gradient of this density:

$$E_{xc}^{GGA}[n] = \int n(r) \epsilon_{xc}[n, \nabla n] dr, \quad (1.9)$$

The GGA exchange correlation functional is much more robust for the study of iron based alloys [57]. In particular, GGA correctly predicts the ferromagnetic ground state of bcc iron [221].

All-electrons DFT methods treat core and valence electrons on an equal footing. But in practice, the effect of core electrons on the chemical bonds is usually negligible, while all-electrons wavefunctions exhibit rapid oscillations in the core region, which increases drastically the computational cost. The *pseudo-potential* approximation aims to reduce this cost by replacing the core electrons and the corresponding Coulomb potential by a *pseudo-potential* that acts on a set of pseudo wavefunctions. An important point regarding *pseudo-potentials* is the degree of hardness. A *pseudo-potential* is considered 'soft' when it requires a small number of Fourier

components for its accurate representation and ‘hard’ otherwise. Among all the existing *pseudo-potentials*, the most commonly used are the norm-conserving *pseudo-potentials* (NCPP), ultra-soft *pseudo-potentials* (USPP) and the projector augmented wave method (PAW). In the case of NCPP and USPP *pseudo-potentials*, core electrons are represented by smoother potentials and wavefunctions while beyond a given cut-off radius pseudo wavefunctions are identical to all-electrons wavefunctions. The PAW approach is a bit different: below the cut-off radius, the wavefunction is defined as a linear transformation of the all-electrons wavefunction in the frozen core approximation. The PAW method is more robust than the NCPP or USPP while staying more efficient than all-electrons potentials in terms of computational cost.

Finally, in order to calculate the Kohn-Sham energy, wavefunctions are represented as a linear combination of a basis functions. Usually, we either use localized basis functions (for example Gaussian or pseudo-atomic orbitals) as in the SIESTA (Spanish Initiative for Electronic Simulations with Thousands of Atoms) code, or plane-waves basis functions as in the VASP (Vienna *ab-initio* simulation package) code. In this study, we use the latter.

DFT allows to determine the electronic, energetic and magnetic ground-state properties of a given atomic configuration. The associated forces and stresses can also be obtained (using the Hellmann-Feynman theorem). They can be for example relaxed in order to find equilibrium configurations.

1.1.2 Calculation details

In this work, we performed DFT calculations with the Projected Augmented Wave (PAW) method [23, 98] as implemented in the VASP code [96–98]. 3d and 4s electrons are considered as valence electrons for Fe, Cr and Mn atoms, and 4d and 5s electrons for Mo, while 2s and 2p states are considered for C. We employed the Generalized Gradient Approximation (GGA) with the Perdew-Burke-Eruzerhof (PBE) scheme [145]. As explained in Sec. 1.1.1, DFT calculation using LDA do not predict the ferromagnetic ground state of pure body-centered cubic (bcc) iron. Lv *et al.* [117] compared Fe₃C lattice constants predicted by GGA and LDA and showed that the GGA lattice constants matched fairly well the experimental results, but that the error on LDA ones is more important. Therefore, LDA cannot be trusted for the study of cementite. All the calculations were spin polarized within the collinear approximation. The plane-wave basis cut-off was set to 500 eV. The convergence cut-off for the electronic self-consistency loop was set to $\Delta E = 10^{-6}$ eV.

Except when otherwise mentioned, all the results presented below are obtained using supercells. In the case of cementite and α -cementite (see Chap. 4), we used a $2 \times 2 \times 2$ supercell and a $5 \times 4 \times 5$ k-point grid, following the Monkhorst-Pack scheme [130]. Mo₂C carbide admits hexagonal, orthorhombic or cubic structures [32, 143, 214]. As a first step, we chose to focus on orthorhombic Mo₂C since it was found to be energetically most favorable by previous *ab-initio* studies [1, 110, 161]. For orthorhombic Mo₂C, we used a $2 \times 2 \times 2$ supercell and a $5 \times 5 \times 5$ k-point grid. Calculations for pure bcc Fe were performed in a $4 \times 4 \times 4$ supercell, while the size of the supercell used for the calculations of bcc Fe with various local C concentrations is sometimes $3 \times 3 \times 3$, but mostly $4 \times 4 \times 4$. The associated k-point grid are equivalent to a $16 \times 16 \times 16$ k-point grid for the bcc unit cell. Atomic positions, cell shape and size were fully relaxed to ensure a maximum residual force of 0.02 eV/Å

and a maximum residual stress of 3 kbar.

In order to estimate formation free energies, we also determined vibrational entropies in cementite, α -cementite and Mo_2C . Vibrational properties can be obtained via DFT calculations using the *frozen phonons* method. Phonons are quantized modes of vibration of oscillating atoms in a lattice (e.g. a crystal). The frozen phonons method consists in slightly displacing one atom in a given supercell, and calculating the forces induced by this displacement, using the Hellmann-Feynman theorem. This procedure performed on all the atoms, in the three spatial directions, allows us to build the force constants matrix and the dynamical matrix, which lead to the vibration modes of the system. Considering phonon modes as independent harmonic oscillators, the vibrational entropy can be obtained from:

$$S_{\text{vib}} = k_B \sum_1^{3N} \left\{ \frac{\beta \epsilon_i}{e^{\beta \epsilon_i} - 1} - \ln(1 - e^{-\beta \epsilon_i}) \right\}, \quad (1.10)$$

with k_B the Boltzmann constant, $\beta = (k_B T)^{-1}$ (T the temperature) and $\epsilon_i = \hbar \omega_i$ (\hbar the reduced Planck constant, ω_i the phonon frequency).

Vibrational entropies were obtained within the harmonic approximation from the frozen phonon calculations using VASP and PHONOPY [189]. Before the phonon calculations, all the supercells were first fully relaxed with a maximum residual force of 0.001 eV/Å and a maximum residual stress of 1 kbar. Using the symmetries of the system, we can drastically reduce the required number of displacements. In the case of pure bcc iron, or bcc iron with an isolated C interstitial, we used a $4 \times 4 \times 4$ supercell. However, compared to common crystal structures such as bcc or fcc, carbides admit less symmetries. Therefore, in order to reduce the computational cost, we only used a $2 \times 1 \times 2$ supercell for cementite and α -cementite, while we kept the $2 \times 2 \times 2$ supercell for Mo_2C .

The Curie temperatures of carbides are generally much lower than in bcc Fe. The estimation of certain properties were calculated in paramagnetic cementite by using a random distribution of collinear spins.

Lastly, we studied carbon diffusion properties in cementite and alloyed cementite (see Chap. 2), but also in α -Fe and α -cementite with various C local concentrations (Chap. 4). To that end, we calculated the energy barriers between given initial and final configurations using the Nudged Elastic Band (NEB) method [82], as implemented in the VASP code. With this method, an approximation of the reaction path is built: a set of intermediate configurations (or 'images') is created (often by performing a linear interpolation between the initial and final configurations). The images are bonded together by spring constants so that they are constrained and do not end in the closest stable state, while the atomic forces (relaxed in the hyperplane orthogonal to the reaction path), as well as tangential forces between the images are minimized. This way, the NEB method allows us to find the minimum energy path (MEP) taken by the jumping atom(s). In our NEB calculations, we use at least three images between two given energy minima. These NEB calculations were performed at constant volume, adopting the lattice vectors of the fully relaxed cementite, α -cementite with a given carbon stoichiometry or bcc Fe with a C interstitial supercell. At this point, there is not guarantee that we sampled the saddle-point configuration (especially if we used few images). This is why we systematically used the

so-called climbing NEB method [61] to refine our NEB calculations. In the climbing NEB method, the image with the highest energy is freed from its spring constant and moved along the reaction path to further maximize its energy.

In Chap. 2, we investigated thoroughly the diffusion coefficient of carbon in cementite and alloyed cementite. In solids, the diffusion coefficient usually follows an Arrhenius law:

$$D = D_0 \exp\left(\frac{-Q}{k_B T}\right), \quad (1.11)$$

with Q the activation energy, T the temperature and k_B the Boltzmann constant. For all the C jumps, the diffusion coefficient pre-factor D_0 was approximated by that of an octahedral C migration in bcc-Fe, the saddle-point configuration being the C at a tetrahedral site. D_0 can be expressed as:

$$D_0 = \frac{na^2}{6} \nu_0 f, \quad (1.12)$$

with a the jump length, n a geometrical factor for the number of equivalent jump paths and f the correlation factor. Since carbon diffusion in bcc Fe is random, we have $n = 4$ and $f = 1$. The energy barriers appearing in the expression of D , as well as the attempt frequency ν_0 are calculated with DFT. In the framework of the Vineyard transition-state theory [203], the attempt frequency (ν_0), is given by:

$$\nu_0 = \frac{\prod_1^{3N-3} \nu_i}{\prod_1^{3N-4} \nu_i^*}, \quad (1.13)$$

with ν_i the i -th vibration mode of the initial configuration (C in an octahedral site) and ν_i^* the i -th vibration mode in the saddle-point configuration (C in a tetrahedral site). For both configurations, the three vibration modes associated with the translation of the system are not considered (they are almost equal to zero because of the invariance with respect to translation). The imaginary mode (negative ν_i^*) of the saddle point is also excluded.

1.1.3 Kinetic cluster expansion (KineCluE)

We want to estimate the diffusivity of carbon in cementite. DFT calculations provide valuable information about migration paths and formation energies. However, in most cases, this data alone is not sufficient to evaluate mass-transport properties at the macroscopic scale, because the average mobility of a species is the result of all possible kinetic trajectories with their respective statistical weight.

In out-of-equilibrium systems near equilibrium, the flux \vec{J}_α of a species α under a chemical potential gradient $\vec{\nabla} \mu_\beta$ of species β is given by the Onsager equation [138]:

$$\vec{J}_\alpha = - \sum_\beta L_{\alpha\beta} \vec{\nabla} \frac{\mu_\beta}{k_B T}, \quad (1.14)$$

where $L_{\alpha\beta}$ are the Onsager coefficients, also called transport coefficients. These macroscopic coefficients are equilibrium properties depending on the temperature and local composition. Transport coefficients are independent of the driving forces. The relation between transport coefficients and the displacements of atoms under a

potential gradient is given by the Allnatt formula [8]:

$$L_{\alpha\beta} = \lim_{\tau \rightarrow \infty} \frac{\langle \Delta \vec{R}_\alpha(\tau) \Delta \vec{R}_\beta(\tau) \rangle}{6\tau N_s V_{at}}, \quad (1.15)$$

with N_s the number of sites, V_{at} the atomic volume and $\Delta \vec{R}_\alpha(\tau)$ the total displacement of α atoms during time-step τ . The total displacement is the sum of the displacements of the N_α atoms belonging to the species α : $\Delta \vec{R}_\alpha(\tau) = \sum_{k=1}^{N_\alpha} \vec{r}_k(\tau)$, $\vec{r}_k(\tau)$ being the displacement of atom k during time-step τ . The brackets denote an equilibrium average over an ensemble of realizations. Using the Allnatt formula is the standard way to measure transport coefficients in atomistic simulations such as molecular dynamics or atomic kinetic Monte Carlo (KMC). $L_{\alpha\alpha}$ represents the average mobility of a group of particles belonging to the same atomic species (it can be seen as the mobility of the center of gravity of this group). They are related to the atomic jump frequencies and the kinetic correlations arising from the integration of all possible trajectories. For a dilute solid solution, i.e. when atoms of species α can be considered non-interacting, the diffusion coefficient of the α species is written:

$$D_\alpha = \frac{L_{\alpha\alpha}}{C_\alpha}, \quad (1.16)$$

where C_α is the nominal concentration in α atoms.

In the dilute approximation, the system can be divided into clusters. Clusters are well-separated sub-spaces of the configuration space defined by an interaction range called the kinetic range. Trajectories involving configurations where the cluster is considered dissociated with respect to this cut-off distance are not considered (they are associated with a zero probability). The kinetic range is necessarily higher than the cut-off distance for the thermodynamic interactions. In this framework, it is assumed that each cluster reaches its equilibrium state before merging with another cluster or dissociating into separate sub-clusters. Consequently, the total transport coefficients of a system can be expressed as the sum of each cluster transport coefficients:

$$L_{\alpha\beta} = \sum_c [c] L_{\alpha\beta}^{eq}(c), \quad (1.17)$$

with $L_{\alpha\beta}^{eq}(c)$ the transport coefficient of cluster c and $[c]$ the site concentration of cluster c . The expression of a system kinetic properties (such as the transport coefficients) as a weighted sum of cluster contributions is called the *kinetic cluster expansion* method [168].

During this thesis, we used the kinetic cluster expansion method to investigate the diffusivity of carbon in cementite. The integration of all possible trajectories for a carbon atom is performed using the open-source code KineCluE (Kinetic Cluster Expansion) [166, 168] which automates the *self-consistent mean-field (SCMF) theory* [132] to compute transport coefficients from the knowledge of the crystal structure, the available jump mechanisms for the C interstitial and information about the energetic landscape of the system. The input data were calculated using DFT. Then, the KineCluE code performs the complete analysis of the system and jump mechanism, explores the configuration space of the cluster, applies a chemical potential gradient to the system, sets up the mathematical problem and finally solves it to compute the resulting average fluxes. Transport coefficients are then identified from

Eq. 1.14. Within the KineCluE framework, the competition between various jump mechanisms as well as the interaction between C and other alloying elements are included [17, 26, 126, 168].

We also investigated the influence of an alloying element on C diffusivity in cementite. Under the approximation that the system is dilute in interstitial C and substitutional solute M ($M = \text{Cr}, \text{Mo}, \text{Mn}$), we used the kinetic cluster expansion formalism to compute the effect of cementite alloying on carbon diffusivity to first order in alloying elements concentration:

$$\bar{D}_C([\bar{M}]) = \frac{[C]D_C + [MC]D_p}{[\bar{C}]}, \quad (1.18)$$

where \bar{D}_C is the average C diffusion coefficient, $[\bar{M}]$ and $[\bar{C}]$ are the nominal solute and interstitial carbon concentrations, respectively, $[C]$ is the concentration of isolated (i.e. far from alloying elements) interstitial carbon, $[MC]$ is the concentration of solute-interstitial carbon pair, D_C is the diffusion coefficient of a single interstitial C atom in Fe_3C cementite and D_p is the diffusion coefficient of an interstitial carbon atom around a solute M . All concentrations are given per cementite unit formula Fe_3C . These concentrations were obtained by using an approximation of the low-temperature expressions for dilute system [126, 169], and solving the following coupled equations for given nominal concentrations:

$$\begin{aligned} [\bar{C}] &= [C] + [MC] = Z_C Y_C + Z_{MC} Y_C Y_M, \\ [\bar{M}] &= [M] + [MC] = Z_M Y_M + Z_{MC} Y_C Y_M, \end{aligned} \quad (1.19)$$

where the $Y_\alpha = \exp(\mu_\alpha/k_B T)$ variables are the unknown of this system of equations, and the chemical potentials are taken as the energy required to create an interstitial carbon atom at an octahedral site or a M_{II} substitutional solute (the structure of cementite is detailed in Chap. 2). With these references in mind, the monomer partition functions read:

$$\begin{aligned} Z_C &= 1 + \exp(-\Delta E_C/k_B T), \\ Z_M &= 2 + \exp(-\Delta E_M/k_B T), \end{aligned} \quad (1.20)$$

where ΔE_C is the energy difference between a carbon atom forming a dumbbell at a cementite carbon site and a carbon atom being at an interstitial octahedral site. ΔE_M is the energy difference between configurations where M is inserted at a M_{II} or M_{I} substitutional site. For Z_{MC} in Eq. 1.19, we chose a pair partition function to encompass all configurations that were computed ab-initio, which means all configurations where the distance between the solute and the carbon atom are below 5.83 Å. This choice makes sense as long as carbon-solute binding energies can be assumed to be zero beyond this distance.

If we pick the same definition of the pair cluster in KineCluE (setting the kinetic range to the same cutoff distance) we would not have converged diffusion coefficients because kinetic correlations always extend beyond thermodynamic interactions. But if we extend the kinetic range to a larger value, we would have inconsistent definitions between the thermodynamic and kinetic definition of the cluster, and we would also include monomer contributions into the diffusion coefficient of C around the solute. To solve this issue, we consider that a calculation to a larger

kinetic radius (therefore a larger partition function) can be written as the sum of a pair contribution (defined by the 5.83 Å cutoff distance) and a monomer contribution. We can do the same calculation while setting all interactions between carbon and solute to zero, which will allow us to remove the monomer contribution with the same geometry. Under these considerations, we define the carbon diffusivity around a solute as:

$$D_p(r_k) = D_C + \frac{Z(r_k)}{Z_{MC}} (D_C(r_k) - \tilde{D}_C(r_k)), \quad (1.21)$$

where $Z(r_k)$ is the partition function obtained by setting the kinetic range to r_k , $D_C(r_k)$ is the C diffusion coefficient around a solute computed with kinetic range r_k , and $\tilde{D}_C(r_k)$ is similar except that all carbon-solute interactions are set to zero. The C diffusion coefficient around a solute $D_p(r_k)$ defined this way converges quickly with r_k and any r_k value larger than 9 Å will give the same value.

1.2 Monte-Carlo Simulations

1.2.1 Principle

Monte-Carlo simulations are numerical stochastic methods that describe the evolution of a given system. They admit a very wide range of application, from physics to chemistry, mathematics, finance or even medicine. In material science, Monte-Carlo (MC) simulation allows us to determine the properties of the equilibrium state and follow the evolution of the kinetics properties of a system.

The overall principle is simple: for each event that can modify a given system, we associate a probability of success. To determine if an event is accepted or not, its success probability is then compared to a random number. In our case, the system is an ensemble of atoms (Fe or C) arranged on a rigid lattice, while the events are diffusing atoms.

The probability for a system to be in the configuration $\{C_i\}$ is noted π_i , while the probability of transition from the configuration $\{C_i\}$ to a new configuration $\{C_j\}$ is given by $P_{i \rightarrow j}$. The detailed-balance condition states that:

$$\pi_i P_{i \rightarrow j} = \pi_j P_{j \rightarrow i}. \quad (1.22)$$

The detailed balanced condition ensures that the Monte-Carlo simulation tends to the thermodynamic equilibrium.

In our study, two types of Monte-Carlo algorithms were used to investigate cementite precipitation (see Chap. 4): the *Metropolis algorithm* and the *Residence Time Algorithm* (RTA). In the following sections, we summarize the principles behind these two algorithms.

1.2.2 Metropolis Algorithm

In the Metropolis algorithm, the probability of a random transition is a function of its energetic cost. All the possible configurations of the system are noted $\{C_k\}$. Each Monte-Carlo step executes the following process:

- The total energy E_i of the system in its current configuration $C_i \in \{C_k\}$ is calculated
- All the configurations $\{C_k\}_i$ accessible from C_i are listed. One of them, $C_j \in \{C_k\}_i$, is selected randomly. The transition ($i \rightarrow j$) between the two configuration is performed and the energy E_j of the chosen configuration C_j is computed.
- The probability of the transition $i \rightarrow j$ is given by:

$$P_{i \rightarrow j} = \exp\left(-\frac{\Delta E_{i \rightarrow j}}{k_B T}\right), \quad (1.23)$$

with $\Delta E_{i \rightarrow j} = E_j - E_i$ the energetic cost (see next paragraph), k_B the Boltzmann constant and T the temperature.

- A random number r ($0 \leq r < 1$) is generated. The transition is accepted if: $\Delta E_{i \rightarrow j} \leq 0$ or if $\Delta E_{i \rightarrow j} > 0$ and $r \leq P_{i \rightarrow j}$.
- If the transition is not accepted, the system is reversed to its initial state C_i .

The main advantage of the Metropolis algorithm is that for each Monte-Carlo (MC) step, we only need to determine one ΔE and its associated probability. In practice, $\Delta E_{i \rightarrow j}$ can either be the energy difference between C_j and C_i or the energy difference between a saddle point and the initial configuration C_i . In this work, we use the former to access thermodynamic properties of a system (equilibrium Monte-Carlo) and we use the latter for the study of the kinetic properties (kinetic Monte-Carlo). The main drawback of the Metropolis algorithm is that the success rate can be very low (especially at low temperature), sometimes generating a significant waste of computing time.

1.2.3 Residence Time Algorithm

Within the residence time algorithm (also called Bortz-Kalos-Lebowitz algorithm), the energetic cost and probability of each possible transition is calculated. Each MC step executes the following process:

- The total energy E_i of the system in its actual configuration $C_i \in \{C_k\}$ is calculated.
- All the configurations $\{C_k\}_i$ accessible from C_i are determined.
- The $\Delta E_{i \rightarrow j}$ and $P_{i \rightarrow j}$ of all $\{C_k\}_i$ are calculated. The attempt frequencies are given by:

$$\Gamma_{i \rightarrow j} = \nu_{i \rightarrow j} P_{i \rightarrow j}, \quad (1.24)$$

with $\nu_{i \rightarrow j}$ the jump frequency associated to the $i \rightarrow j$ transition. In our study of α -cementite precipitation, we consider that the attempt frequencies $\nu_{i \rightarrow j}$ are all equal to the attempt frequency of an isolated C interstitial in bcc iron. A random number is generated in order to pick a probability and its associated

transition in a way that transitions with higher probabilities are more likely to be selected.

- The selected transition is performed.
- The physical time is incremented by $\frac{1}{\Gamma_{tot}}$, with $\Gamma_{tot} = \sum_{C_j \in \{C_k\}_i} \Gamma_{i \rightarrow j}$. The energetically more stable C_i configurations are associated with lower probabilities of transition $P_{i \rightarrow j}$ and thus with higher time increments.

The advantage of the residence time algorithm is that a transition is performed at each MC step. However, this entails the calculation of all possible $\Delta E_{i \rightarrow j}$, $P_{i \rightarrow j}$ and $\Gamma_{i \rightarrow j}$ at each step, which can critically increase the computation time. In addition, if there is a large gap between probabilities of transition, the system can get trapped.

In both algorithms, these MC steps are performed in loops until the equilibrium state is reached. In our study, we performed equilibrium MC simulations with the Metropolis algorithm to investigate thermodynamic properties of cementite precipitation and we used the residence time algorithm to study the kinetics of our system. All the Monte Carlo simulations presented in this work were performed using the code written by Dominique Gendt [52] and latter modified by Thomas Schuler [170] during their respective PhD works.

1.3 CALPHAD

Throughout this work, our theoretical results are compared with experimental data (when available). As explained in the introduction, we pay a particular attention to the comparison with Anna Benarosch's experiments. In addition, both theoretical and experimental results obtained in our respective thesis are also compared with CALPHAD data. CALPHAD stands for *CAL*culat*ion of PH*ase *D*iagrams. This phenomenological method was introduced for the first time in Kaufman and Bernstein book [86] in 1970. It is based on the thermodynamic (free energy, composition, volume,...) and kinetic properties of phases in pure element, binary or ternary systems. The data of these simple systems can be obtained through experiments or theoretical calculations (such as ab-initio calculations). Appropriate mathematical models are then used to predict the properties of higher-order system. The accuracy of such prediction depends strongly on the completeness and the reliability of the databases.

In our study, we used the Thermo-Calc commercial software [12, 186] with the TCFE Steels/Fe-alloys version-10 database. Since we focus on carbide precipitates in ferritic steels, we systematically prevent the formation of more stable phases (such as diamond and graphite). In this thesis, we used CALPHAD data to investigate the equilibrium concentration of substitutional solutes in alloyed cementite (M_3C) and M_2C . We also studied the enthalpy and free energy of carbide phases.

Except when otherwise mentioned, all our concentrations are expressed in atomic percent. In particular, the concentration x of metallic alloying element in carbides is expressed as the concentration of metallic host sites occupied. Alloyed cementite and molybdenum carbides are written as $(Fe_{1-x}M_x)_3C$ or $(Mo_{1-x}M_x)_2C$, respectively. To simplify notations and facilitate the reading, they can also be found as M_3C or M_2C .

Chapter 2

Fe₃C cementite: point defects and diffusion.

In this chapter, we investigated various point defects (namely vacancies, Frenkel pairs and interstitial sites) in Fe₃C. Based on this knowledge, we present a detailed investigation of C migration mechanisms, and determine the C diffusion coefficients in Fe₃C and weakly alloyed cementite (Fe_{1-x}M_x)₃C, with M = Mo, Cr and Mn, which are common alloying elements in ferritic steels. The predicted coefficients in Fe₃C are in good agreement with experimental measurements of carburization rate in ferritic steels. In the alloyed cementites, the C diffusion can be slowed down due to the presence of a few Mn solutes up to 500 K, while it is mostly unaffected by the addition of Mo or Cr solutes.

2.1 State of the art

In order to better understand the kinetics of cementite growth, or the transition mechanism from this carbide to another one, it is essential to understand its atomic diffusion properties. Since interstitial diffusion generally requires a lower activation energy than the vacancy-mediated diffusion of the metallic atoms, as a first step, we address the carbon diffusion in cementite.

There are relatively few experimental studies on C diffusion in Fe₃C. All of them are carburization experiments, in which C diffusion coefficients in Fe₃C were indirectly obtained through the dependence of cementite growth rate on the carbon activity in the gas phase. Hillert and Sharp [66] first studied carbon diffusion in cementite at 1138 K by imposing a low C activity ($a_c=1.3$) at the cementite surface. They evaluated the carbon diffusion coefficient in Fe₃C at $D_C \approx 1.27 \times 10^{-14} \text{ m}^2\text{s}^{-1}$. Ozturk's group [140, 141] investigated the kinetics of cementite formation by carburizing fine iron powders at 723 K. They estimated the C diffusion coefficient in Fe₃C as a function of carbon activity (from $a_c = 4.3$ to $a_c = 20$), and obtained diffusion coefficients ranging from 10^{-20} to $10^{-19} \text{ m}^2\text{s}^{-1}$. More recently, Schneider and Inden [163] carburized pure iron samples at 773 K. They increased the carbon activity up to $a_c = 4580$. At carbon activities $a_c > 150$, Hägg carbides (Fe₅C₂) formed on top of cementite. They obtained $D_C \approx 6.05 \times 10^{-18} \text{ m}^2\text{s}^{-1}$ in Fe₃C cementite. Additional experimental results are cited in Ref. [104], as a private communication.

They were obtained from carburization experiments on pure iron, for temperature ranging from 843 K to 983 K. The corresponding C diffusion coefficients vary from 3.5×10^{-17} to $1.3 \times 10^{-15} \text{ m}^2\text{s}^{-1}$. Ozturk *et al.* suggested that the C atom migrates via interstitial or interstitialcy mechanism because its diffusion coefficient in Fe_3C increases with the C activity in the gas. Yet, such experimental studies cannot provide detailed information about the migration mechanism at the atomic scale. Moreover, the C diffusion coefficients are measured indirectly and only at rather high temperatures (above 723 K). In addition, the results rely on a cementite growth model which involves several assumptions. Therefore, accurate atomistic modelling provides useful and complementary insights into the diffusion coefficients of C in Fe_3C , and the underlying diffusion mechanisms.

On the theoretical side, Levchenko *et al.* performed a molecular dynamic (MD) simulation of carbon diffusion in cementite [104], employing empirical potentials. In their study, they distinguish C atoms forming the cementite structure (which we will refer to as intrinsic C atoms from now on) located on triangular prismatic sites, from interstitial C atoms in octahedral sites. Levchenko *et al.* found that, as thermally activated events, originally intrinsic C atoms move to nearby interstitial sites, this way creating C Frenkel pairs. Furthermore, the nearest distance between an intrinsic C site and an interstitial octahedral site in cementite (2.55 Å) is lower than the distance between two intrinsic C (3.02 Å), or two interstitial octahedral sites (3.36 Å- 3.37 Å). Therefore, they suggested that carbon diffusion in cementite results from sequences of C intrinsic - C interstitial - C intrinsic jumps. They calculated C diffusion coefficients in cementite between 1273 K and 1373 K and obtained values ranging between 1.66×10^{-12} and $4.19 \times 10^{-12} \text{ m}^2\text{s}^{-1}$. Assuming that the temperature dependence of these coefficients follows an Arrhenius law, these values are in reasonable agreement with an extrapolation of the experimental data to high temperatures. The formation energy found for the C Frenkel pairs was 0.3 eV/atom, while the migration energy was approximately 1.3 eV/atom for temperatures between 1273 and 1373 K. These MD simulations were performed at very high temperatures (between 1273 K and 1373 K), and employed empirical potentials. The obtained concentration of C Frenkel pairs was high: the authors predicted an equilibrium fraction of C atoms in interstitial sites (and thus the same fraction of intrinsic C vacancies) between 0.21 and 0.23. It is worth checking, via first-principles calculations, the efficiency of their proposed mechanism, and the possible occurrence of other mechanisms, in particular at lower temperatures (for instance in the temperature range of the carburization experiments).

On the other hand, previous first-principles study by C. Jiang *et al.* [79] investigated in detail the thermodynamic properties of point defects in pure-Fe cementite. They also calculated energy barriers of the jump of an isolated C vacancy and a C interstitial, which are the structural defects and the proposed diffusing species in C-depleted and C-rich regimes, respectively. However, diffusion coefficients involving long-range diffusion of C atoms were not computed in that study.

In Fe-alloys, metallic solutes commonly substitute certain Fe atoms in cementite precipitates. Experimental studies on the fabrication of bulk cementite through mechanical alloying and spark plasma sintering have shown that Cr, Mn, Mo and V form alloyed cementite and stabilize it [195]. It is therefore relevant to determine the influence of alloying elements on C diffusion in cementite. In this chapter, we focus on Mo, Cr and Mn, because they are common alloying elements in ferritic steels,

employed in nuclear reactors, for example.

2.2 Stoichiometric Fe_3C

Cementite (Fe_3C or $\theta\text{-Fe}_3\text{C}$) crystallises in the orthorhombic space group $Pnma$ (No.62) with 4 formulae unit per unit cell [44]. Its unit cell contains twelve Fe atoms divided in two non-equivalent sub-lattices. Four (4c) Fe atoms are in "special" position (Fe_s) and eight (8d) Fe atoms in "general" positions (Fe_g). The four (4c) C atoms are located in triangular prismatic sites, with six nearest Fe atoms. Both Fe_s and Fe_g are 14-coordinated with twelve Fe and two C nearest neighbors (nn) for Fe_s , and eleven Fe and three C nn for Fe_g . The results presented in this chapter were obtained using $2 \times 2 \times 2$ cementite supercells and a $5 \times 4 \times 5$ k-point grid. Theoretical and experimental lattice parameters are given in Table 2.2. The three lattice vectors (a , b and c) of the orthorhombic unit cell of cementite are respectively parallel to the $[11\bar{1}]$, $[112]$ and $[\bar{1}\bar{1}0]$ directions in a bcc-Fe cell. This orientation relationship will be discussed further in Chap. 4.

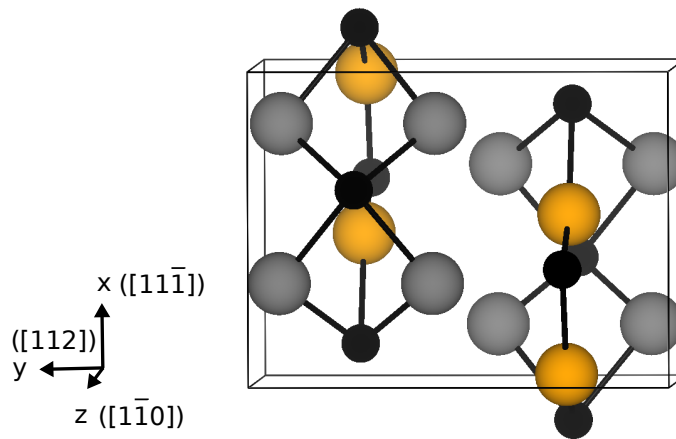


FIGURE 2.1: Crystal structure of Fe_3C cementite. Larger atoms are Fe atoms. Fe_s atoms are in orange, while Fe_g atoms are in grey. C atoms are in black.

The Fe_3C ground state is ferromagnetic. We obtained a magnetic moment of $1.96 \mu_B$ and $1.88 \mu_B$ for Fe_s and Fe_g , respectively. These results are in good agreement with previous ab-initio studies (see Table 2.2). It is well known that the insertion of a C interstitial in bcc Fe decreases the magnetic moment magnitude on the nearby Fe atoms [3, 19, 38]. Similarly, the Fe_g atoms admit a lower magnetic moment because they have one more C nn and one less Fe nn wrt Fe_s . In addition, Fe_g possess a lower Voronoi volume (see Table 2.1), which is consistent with the magneto-volume effect.

The experimental Curie temperature of Fe_3C is estimated to be 460 K [206] or 483-484 K [29, 191]. Older experimental studies also reported some values between 473 K and 513 K [68, 181]. Please note that carburization experiments described above were all performed above the Curie temperature, while, as an approximation, all our calculations are carried out at the magnetic ground state of cementite. An accurate atomistic prediction of the impact of magnetic transition on carbon diffusion

TABLE 2.1: Magnetic moments and Voronoi volumes of C and Fe atoms in Fe_3C cementite. In fully relaxed bcc Fe (constant pressure), the magnetic moment and Voronoi volume of Fe atoms are $2.21 \mu_B$ and 11.36 \AA^3 , respectively. In bcc Fe, an isolated C energetically most favorable interstitial site is an octahedral site with a 6.92 \AA^3 Voronoi volume.

Atom	magnetic moment (μ_B)	Voronoi volume (Å^3)
C	-0.12	7.34
Fe_s	1.96	10.43
Fe_g	1.88	10.06

requires a significant amount of additional work [165], therefore, it is beyond the scope of our study. This approximation will be discussed in Sec. 2.4.

2.3 Point defects in Fe_3C

Any deviation from cementite stoichiometry implies the presence of structural defects in cementite. The properties of Fe and C vacancies or interstitials in Fe_3C were studied from first-principles by Jiang *et al.* [79]. According to their study, C vacancies and C interstitials are the energetically most favorable defects in substoichiometric and C-rich cementite, respectively. In another study [80], Jiang and co-authors used a computational method to identify possible C interstitial in cementite. They predicted the existence of octahedral interstitial sites and three non-equivalent tetrahedral interstitial sites. They found that the octahedral interstitial sites admit the lowest formation energy. Using purely geometric and symmetry considerations, these interstitial sites were also predicted by other studies [108, 211].

2.3.1 Vacancies in Fe_3C

The formation energy of Fe_3C without interstitial is defined by:

$$E^f(n(Fe_3C)) = E(n(Fe_3C)) - 3n\mu_{Fe}(bcc) - n\mu_C(graph), \quad (2.1)$$

where $E(n(Fe_3C))$ is the total energy of the cementite cell. In our case, the DFT calculations were made in a 128 atoms cell, hence $n = 8$. $\mu_{Fe}(bcc)$ is the chemical potential of iron in ferromagnetic bcc iron and $\mu_C(graph)$ is the chemical potential of carbon in graphite. At 0 K, $\mu_C(graph)$ is the total energy per C atom in graphite and $\mu_{Fe}(bcc)$ is the total energy per Fe atom in bcc iron. We used $\mu_C(graph) = E_C(graph) = -9.226$ eV and $\mu_{Fe}(bcc) = E_{Fe}(bcc) = -8.238$ eV, obtained through DFT calculations. The graphite reference energy does not include Van der Waals corrections. For Fe_3C cementite, we obtained a formation energy value of 0.204 eV/f.u., in good agreement with previous studies (see Table 2.2).

The formation energy of a C vacancy in cementite, $E^f(C_v \text{ in } n(Fe_3C))$, is given by:

$$E^f(C_v \text{ in } n(Fe_3C)) = E(n(Fe_3C) + C_v) - E(n(Fe_3C)) + \mu_c, \quad (2.2)$$

$E(n(Fe_3C) + C_v)$ is the total energy of the cementite cell with a C vacancy and μ_c is the chemical potential of carbon in a given reference state. We calculated the formation energy of a C vacancy in cementite with respect to intrinsic C atoms in

TABLE 2.2: Non-exhaustive list of previous theoretical and experimental assessments of Fe₃C lattice parameters.

Method [ref]	Lattice parameters (a,b,c) (Å)	Fe magnetic moment (μ_B) Fe _s , Fe _g	formation energy (eV/f.u.*)
DFT:			
VASP, PAW, GGA, 0 K [this work]	5.036, 6.721, 4.479	1.96, 1.88	0.204 (Fe bcc, graphite)
VASP, PAW, GGA, 0 K [154]	5.0289, 6.7262, 4.4823	2.006, 1.909	0.194 (Fe bcc, graphite)
VASP, PAW, GGA, 0 K [171]	5.058, 6.703, 4.506	1.98, 1.93	0.21 (Fe bcc, graphite)
CASP, USSP, LDA, 0 K [117]	4.8190, 4.4774, 4.2805	1.990, 1.915	
CASP, USSP, GGA, 0 K [117]	5.0080, 6.7254, 4.4650	1.990, 1.915	
WIEN2K, FP-LAPW, GGA, 0 K [43]	5.0679, 6.7137, 4.5133	1.97, 1.96	
VASP, PAW, GGA, 0 K [80]	5.04, 6.72, 4.48	1.96, 1.89	
VASP, PAW, GGA, 0 K [133]	5.036, 6.724, 4.480	1.87	
VASP, PAW, GGA, 0 K [35]	5.035, 6.716, 4.480	1.92, 1.84	0.243 (Fe bcc, graphite)
VASP, PAW, GGA, phonon calc. 298 K [35]	5.053, 6.745, 4.4503	1.92, 1.84	
VASP, PAW, GGA, 0 K [62]	5.024, 6.754, 4.478	1.82	0.18 (Fe bcc, graphite)
LMTO, LDA, 0 K [58]	5.089, 6.743, 4.523	7.92 ^a , 13.92 ^a	
Experimental:			
X-ray diffraction, 298 K [63]	5.090, 6.748, 4.523		
X-ray diffraction, 298 K [106]	5.091, 6.7434, 4.526		
X-ray diffraction, 298 K [44]	5.0896, 6.7443, 4.5248		
Neutron diffraction, 4.2 K [213]	5.082, 6.733, 4.512		
Neutron diffraction, 298 K [213]	5.081, 6.753, 4.515		
Hight-temp calorimetry, 1473 ± 2 K [125]			0.165 ± 0.05

^atotal on-site moment, d contribution only.

* f.u.:formula unit

cementite. Therefore, $\mu_c = \mu_c(\text{Fe}_3\text{C})$. At $T=0$ K and zero pressure we have:

$$E(n(\text{Fe}_3\text{C})) = 3n\mu_{\text{Fe}}(\text{Fe}_3\text{C}) + n\mu_c(\text{Fe}_3\text{C}), \quad (2.3)$$

Assuming that the cementite precipitate is in equilibrium with the bcc iron matrix, ($\mu_{\text{Fe}}(\text{Fe}_3\text{C}) = \mu_{\text{Fe}}(\text{bcc})$), we combine the equations above, as well as Eq. 2.1 to get:

$$\begin{aligned} E^f(C_v \text{ in } \text{Fe}_3\text{C})_{\text{wrt } \text{Fe}_3\text{C}} &= E(n(\text{Fe}_3\text{C}) + C_v) \\ &- E(n(\text{Fe}_3\text{C})) + E^f(\text{Fe}_3\text{C}) + \mu_c(\text{graph}). \end{aligned} \quad (2.4)$$

With the same assumption for the μ_{Fe} , the formation energy of an Fe vacancy in cementite, $E^f(\text{Fe}_v \text{ in } n(\text{Fe}_3\text{C}))$, is given by:

$$E^f(\text{Fe}_v \text{ in } n(\text{Fe}_3\text{C})) = E(n(\text{Fe}_3\text{C}) + \text{Fe}_v) - E(n(\text{Fe}_3\text{C})) + \mu_{\text{Fe}}, \quad (2.5)$$

The formation energies of C and Fe vacancies in cementite are shown Table 2.3.

TABLE 2.3: Formation energy of vacancies in Fe_3C cementite, and Voronoi volumes of the associated sites in stoichiometric Fe_3C . The formation energies are compared with Jiang *et al.* values [79] calculated with ferromagnetic bcc Fe and diamond as the reference states.

Vacancy type	$E^f(V \text{ in } \text{Fe}_3\text{C})_{\text{wrt } \text{Fe}_3\text{C}}$ (eV)	Voronoi volume of the associated site in stoichiometric Fe_3C (\AA^3)
C	0.72 (0.63 [79])	7.34
Fe_s	1.45 (1.45 [79])	10.43
Fe_g	1.67 (1.66 [79])	10.06

Like Jiang and co-authors [79], we found that C vacancies are energetically more favorable than Fe vacancies in cementite, and that Fe_g vacancies are more favorable than Fe_s vacancies. Our Fe vacancies formations energies are in excellent agreement, while our C vacancy formation energy is superior. This can be explained by the different carbon reference states used between our two studies. The formation energy of a vacancy increases with the Voronoi volume of the associated site in stoichiometric Fe_3C . Regarding Fe vacancies relative stability, removing an Fe_g atom also breaks one less Fe-Fe bond than removing an Fe_s atom.

According to experimental and ab-initio studies [77, 190], vacancies on the non-metallic sub-lattices are also the responsible defects for under-stoichiometric carbides (NbC, TiN) and nitrides of early transition metal.

2.3.2 C interstitials in Fe_3C

In order to identify potential C interstitial sites in cementite, we searched for empty volumes in the Fe_3C structure. To do this, we created a grid of sampling points in the cementite unit cell, and determined the lowest distance between each point and an Fe or C atom in the cementite. The sampling points presenting large lowest-distances are likely low-energy C interstitials sites. As a result, we identified 5 types of interstitial sites: octahedral sites (Octa), three non-equivalent tetrahedral sites (labeled T1, T2 and T3) and square-based pyramidal sites. T1 interstitial sites (4c) do not follow the same symmetry as T2 and T3 sites (8d). T2 and T3 sites do not have

the same number of Fe_s or Fe_g nearest neighbors. These interstitial sites are represented in Fig. 2.2. Our octahedral, T1, T2 and T3 sites are the same as Jiang *et al.* [80]. To be fully comprehensive, we also considered the formation of C dumbbells. For the study of diffusion in cementite, relevant dumbbells are centered on intrinsic C-atom positions and oriented along the $[010]$ or $[101]/[\bar{1}01]$ directions. Table 2.4 summarizes energetic and geometric information about the investigated C sites in cementite.

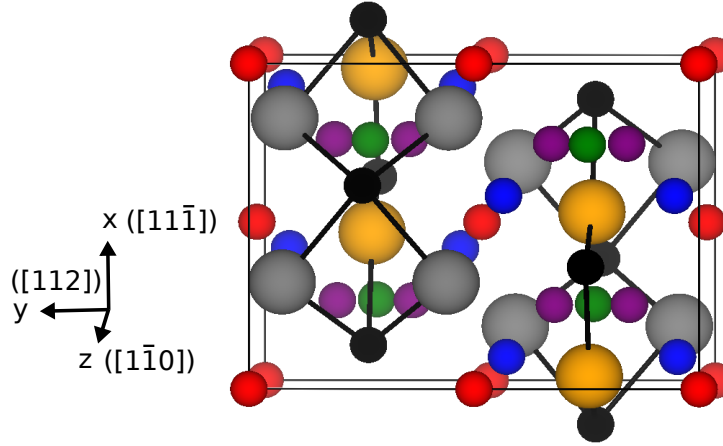


FIGURE 2.2: Crystal structure of Fe_3C cementite. Larger atoms are Fe atoms. Fe_s atoms are in orange, while Fe_g atoms are in grey. Smaller atoms are C atoms. C atoms forming the ideal cementite structure (C intrinsic atoms) are in black. Interstitial octahedral sites for C are in red. T1, T2 and T3 sites are in green, blue and purple, respectively.

TABLE 2.4: Formation energy with respect to cementite and geometrical characteristics of a C interstitial at various interstitial sites in Fe_3C cementite.

C site	$E^f(\text{C}_{\text{int}} \text{ in } \text{Fe}_3\text{C})$ (eV)	Lowest $\text{C}_{\text{int}}\text{-Fe}$ or $\text{C}_{\text{int}}\text{-C}$ distance before (after) relaxation(\AA)	$\text{C}_{\text{int}}\text{-C}$ distance before (after) relaxation (\AA)	C_{int} Voronoi volume in the Fe_3C relaxed cell (\AA^3)
Octa	0.64	1.79 (1.87)	2.55 (2.73)	6.05
T1	3.20	1.51 (1.79)	1.96 (1.99)	5.55
T2	2.62	1.51 (1.77)	1.96 (2.40)	5.40
T3	2.39	1.43 (1.77)	1.97 (2.32)	5.53
dumbbell A	2.34	1.51 (1.44)	1.51 (1.44)	5.88 / 5.59
dumbbell B	1.98	1.30 (1.42)	1.30 (1.42)	5.42

In order to investigate the relative energetic stability of a C atom in each of these interstitial sites, we relaxed each C interstitial configuration. The formation energy of a C interstitial in Fe_3C cementite, $E^f(\text{C}_{\text{int}} \text{ in } n(\text{Fe}_3\text{C}))$, is given by:

$$E^f(\text{C}_{\text{int}} \text{ in } n(\text{Fe}_3\text{C})) = E(n(\text{Fe}_3\text{C}) + \text{C}_{\text{int}}) - E(n(\text{Fe}_3\text{C})) - \mu_{\text{C}}, \quad (2.6)$$

with $E(n(\text{Fe}_3\text{C}) + \text{C}_{\text{int}})$ the total energy of the cementite cell with an additional C interstitial. As in Sec. 2.3.1, if we assume that cementite is in equilibrium with a bcc

TABLE 2.5: C-nearest Fe distances and average nearest Fe magnetic moments for a C atom at interstitial sites in Fe_3C . In Fe_3C without interstitial, Fe_s atoms and Fe_g magnetic moments are $1.96 \mu_B$ and $1.88 \mu_B$, respectively.

Interstitial site	number of nearest Fe neighbors Fe_s/Fe_g	C-Fe distances after relaxation (Å)	average magnetic moment of Fe nearest neighbors (μ_B)
Octa	2/4	[1.87-1.91]	1.63
T1	2/2	1.79-1.87 resp	1.13
T2	1/3	[1.77-1.92]	1.40
T3	2/2	[1.77,1.92]	1.33
dumbbell A	2/3 and 1/4	[1.89-2.05] and [1.87-1.99]	1.80 / 1.83
dumbbell B	2/3 and 2/3*	[1.84-2.03]	1.79

* The 2 Fe_s nearest neighbors are the same for both C forming a dumbbell.

iron matrix, combining Eq. 2.1, Eq. 2.3 and Eq. 2.6, we get:

$$E^f(C_{\text{int}} \text{ in } Fe_3C)_{\text{wrt } Fe_3C} = E(n(Fe_3C) + C_{\text{int}}) - E(n(Fe_3C)) - E^f(Fe_3C) - \mu_C(\text{graph}). \quad (2.7)$$

The formation energies of the C interstitial sites calculated with respect to Fe_3C are shown Table 2.4. Because of their very high formation energy (6.16 eV), the square-based pyramidal sites were not considered further. The octahedral sites were found to be the energetically most favorable, with a formation energy of 0.64 eV with respect to cementite. This result is in good agreement with Jiang *et al.* study mentioned previously [80]. Like us, they found that octahedral sites are energetically more favorable, followed by T3, T2 and T1 interstitial sites. In Levchenko *et al.* MD study of C diffusion in cementite [104], all the C interstitial sites considered are indeed the octahedral sites.

If we compare the properties of each interstitial sites (Table 2.4 and 2.5), C octahedral interstitial sites are associated with the larger lowest-distance to another atom of the structure, the highest Voronoi volume and the higher average magnetic moments of the nearest Fe neighbors. As explained in Sec. 2.2 the insertion of a C interstitial in bcc Fe decreases the magnetic moment magnitude on the nearby Fe atoms [3, 19, 38]. Similarly, there is also a magnetic moment reduction on the nearest-neighbor Fe atoms of a C interstitial in cementite. The resulting values are given in Table 2.5.

2.3.3 C Frenkel pairs in cementite

As explained in Sec. 2.1, Levchenko *et al.* performed a molecular dynamic (MD) simulation of carbon diffusion in cementite [104]. They found that, as thermally activated events, originally intrinsic C atoms move to nearby interstitial sites, this way creating C Frenkel pairs. For a comparison, we also considered the possible formation of C Frenkel pairs in cementite. To this end, we investigated all the possible pairs of a C intrinsic vacancy and a C in an octahedral site, for distances lower than the distance between two neighboring octahedral interstitial sites (3.36 Å). The

formation energy of a C Frenkel pair defect in cementite $E^f(C_{\text{int}} + C_{\text{v}} \text{ in } n(\text{Fe}_3\text{C}))$ is given by:

$$E^f(C_{\text{int}} + C_{\text{v}} \text{ in } n(\text{Fe}_3\text{C})) = E(C_{\text{int}} + C_{\text{v}} \text{ in } n(\text{Fe}_3\text{C})) - E(n(\text{Fe}_3\text{C})) \quad (2.8)$$

with $E(C_{\text{int}} + C_{\text{v}} \text{ in } \text{Fe}_3\text{C})$ the total energy of the simulation cell containing the C Frenkel pair and $E(n(\text{Fe}_3\text{C}))$ the total energy of the same Fe₃C cell without any defect. The lowest distances between an intrinsic site and octahedral interstitial site are 2.55 Å, 2.65 Å and 3.09 Å, with a formation energy of 1.01 eV, 1.10 eV and 1.22 eV, respectively. The 0.30 eV formation energy estimated in Levchenko *et al.* molecular dynamics study [104] is more than three times lower than our DFT values. Please note that this value does not correspond to the formation energy of an isolated Frenkel pair, but an average value on an arrangement of Frenkel pair.

Since the 0.3 eV formation energy was obtained from MD simulations at very high temperatures (between 1273 K and 1373 K), we investigated the effect of the vibrational entropy on the formation of C Frenkel pairs. To that end, we performed phonons calculations via DFT. Since such calculations are very CPU expensive in these low-symmetry systems, we focused on the case of the energetically most favorable Frenkel pair (with the lowest C intrinsic - C octahedral interstitial distance). As a result, the free energy of formation only decreases from 1.01 eV at 0 K to 0.89 eV at 1273 K, and 0.88 eV at 1373 K, compared to 0.3 eV from the MD study.

The C Frenkel pair concentration predicted by this MD study is quite high: the authors predicted an equilibrium fraction of C atoms in interstitial sites (and thus the same fraction of intrinsic C vacancies) between 0.21 and 0.23. The formation energy of several neighboring Frenkel pairs could be lower than the formation energy of a single Frenkel pair. However, the number of close Frenkel pairs configurations to explore is too large to provide a comprehensive DFT study. Nonetheless, we considered several configurations of 2 Frenkel pairs, and calculated formation energies (per pair) around 0.86 eV. This value is the average on three configurations where the $C_{\text{int}} - C_{\text{int}}$ distances (before relaxation) are 5.03 Å, 3.36 Å and 3.36 Å; and the $C_{\text{v}} - C_{\text{v}}$ distances (before relaxation) are 3.63 Å, 5.10 Å and 3.03 Å. The lowest calculated formation energy, 0.75 eV, corresponds to the configuration with the lowest $C_{\text{int}} - C_{\text{int}}$ and $C_{\text{v}} - C_{\text{v}}$ distances among the configurations tested.

Therefore, based on the present DFT results, Levchenko *et al.* interatomic potentials greatly underestimate the formation energy of C Frenkel pairs in cementite.

2.4 C diffusion in Fe₃C

2.4.1 C diffusion mechanisms and associated energy barriers

According to Levchenko and co-authors MD study [104], C diffusion in cementite comes from the formation of C Frenkel pair defects in cementite, inducing a chain of C intrinsic - C interstitial - C intrinsic jumps. This mechanism relies on a high concentration of C Frenkel pairs (or in other words, a low formation energy for various neighboring Frenkel pairs). However, according to our DFT prediction (Sec. 2.3.3), they greatly underestimate the formation energy of C Frenkel pairs, which leads

to a large overestimation of the number of Frenkel defects in cementite. Therefore, their diffusion mechanism should be less efficient, especially at intermediate temperatures. In fact, in the carburization experiments, the carbon activity in the vapor phase was tuned to provide interstitial carbon atoms in Fe_3C . In other words, we do not need to form C Frenkel pairs to have C atoms in interstitial sites in cementite. For these reasons, we chose to investigate another diffusion mechanism, based on C interstitial diffusion in cementite.

As shown in Sec. 2.3.2, octahedral sites are the energetically most favorable C sites in cementite. The octahedral interstitial sites form a slightly tetragonal network in cementite, with 3.37 Å between nearest-neighbor octahedral sites along the [101] and $[\bar{1}01]$ directions, and 3.36 Å between nearest-neighbor octahedral sites along the y direction. Diffusion of a C interstitial in Fe_3C is assumed to occur from one octahedral site to another, while the other interstitial sites are possible metastable or saddle-point positions. We investigated two migration mechanisms: (i) a direct-interstitial mechanism, and (ii) an indirect mechanism via successive exchanges between interstitial and intrinsic C atoms. In the direct migration mechanism, a C interstitial atom simply jumps from one octahedral site to another. In the case of an indirect mechanism, an interstitial C atom jumps to replace an intrinsic cementite C atom, and the "kicked-out" atom jumps to a nearby interstitial octahedral position. A schematic view of these two migration mechanisms is given in Fig. 2.3. The resulting migration barriers, given in Table 2.6, lie between 2.13 and 2.54 eV. The lowest migration barrier was found for a direct mechanism in the xz plane in cementite (see Fig. 2.4). The lowest-energy barrier for the indirect jump mechanism (2.16 eV) is associated with a jump along the y axis and involves the energetically most favorable dumbbell configuration (B dumbbell along y). Along the indirect migration path considered, the dumbbell configurations are intermediate local minima. Jiang *et al.* [79] attempted to determine the minimum energy path and migration barrier for C diffusion in cementite. They considered both vacancy and interstitial mechanisms. For the latter, they considered the jump of a C atom between two neighboring octahedral sites, in the y direction and in the xz plane. Using first-principles calculations in small 32-atoms supercells, they calculated a 2.29 eV and 2.27 eV barrier, respectively. The authors did not detail the corresponding migration paths, but these values are closed to our 2.16 eV and 2.13 eV barriers calculated in the same directions.

It is interesting to mention that, Kawakami *et al.* [87] investigated hydrogen (H) diffusion in Fe_3C . From their results, the relative stability of Octa, T1, T2 and T3 sites in the same for C or H interstitials. They investigated two migration paths associated with a direct interstitial diffusion mechanism (the Octa - T3 - T2 - Octa and Octa - T3 - T1 - T3 - Octa migration paths).

2.4.2 Determination of C diffusion coefficients

The DFT migration mechanisms and their associated energy barriers were used as inputs for the KineCluE code in order to compute the C diffusion coefficients in each direction, as shown in Fig 2.5. The KineClue code computes transport coefficients

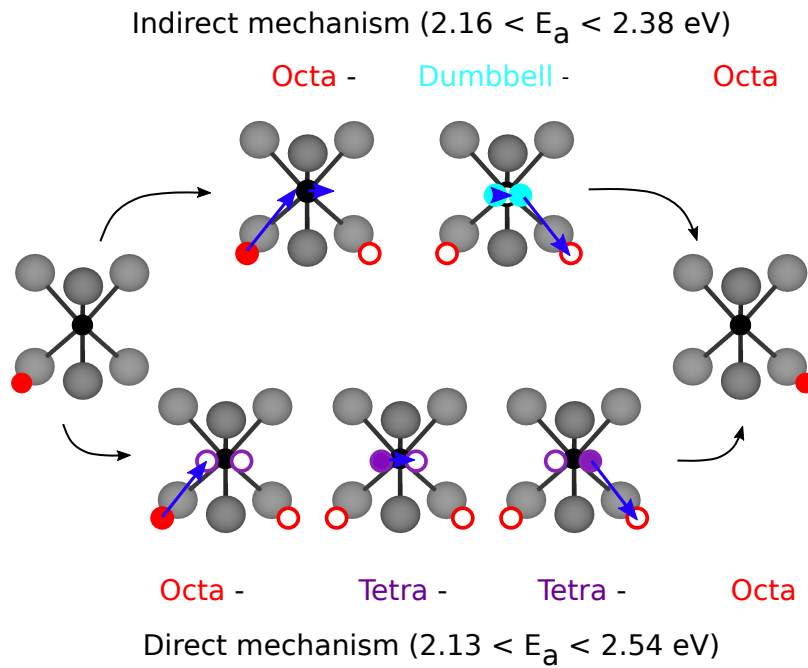


FIGURE 2.3: Schematic view of indirect and direct C interstitial migration mechanisms in Fe₃C. Filled circles denote occupied sites, empty circles are vacant sites. Intrinsic C sites are in black, Fe sites are in grey. C octahedral interstitial sites are in red, T3 interstitial sites are in purple and dumbbells are in cyan.

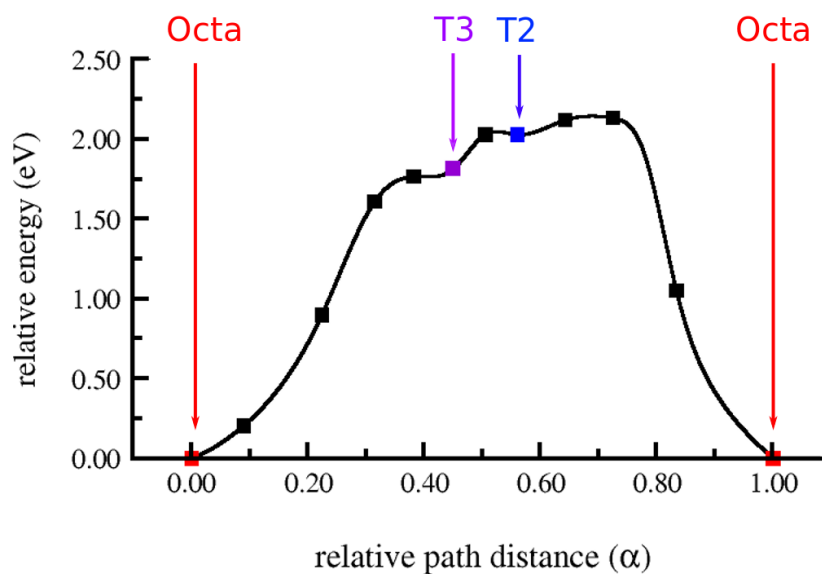


FIGURE 2.4: Minimum Energy Path for the Octa - T3 - T2 - Octa direct jump mechanism along the xz plane in Fe₃C. The C interstitial (in red) goes from an octahedral site to another octahedral site, passing through two tetrahedral sites.

TABLE 2.6: Summary of relevant jump mechanisms of a C interstitial and their associated energy barriers in Fe_3C cementite.

Jump mechanism	Path	Energy barrier (eV)
Indirect	Octa - B Dumbbell - Octa along y axis	2.16
	Octa - A Dumbbell - Octa along the xz plane	2.38
Direct	Octa - T3 - T2 - Octa along the xz plane	2.13
	Octa - T3 - T3 - Octa along y axis	2.46
	Octa - T3 - T1 - T3 - Octa along y axis*	2.54
	Octa - T1 - Octa along y axis*	2.54

*The Octa - T3 - T1 - T3 - Octa and Octa - T1 - Octa migration path along y are ultimately the same. Moreover, they are just a less likely variation of the Octa - T3 - T3 - Octa migration path and thus were not considered as inputs for the KineCluE code.

from the knowledge of the crystal structure, the available jump mechanisms for the C interstitial and information about the energetic landscape of the system. This code is based on methods described in Sec. 1.1.3. Our calculation details are also summarized in that section. At variance with Levchenko *et al.*, we do not consider any C interstitial formation energy, but just the C migration energies between octahedral interstitial sites, for the C diffusion activation energy. We assumed the same attempt frequency for all the C jumps to be the one of an isolated C octahedral jump in bcc Fe for which we obtained an activation energy of 0.86 eV and an attempt frequency of 30.64 THz (corresponding to a diffusion prefactor of $D_0 = 4.09 \times 10^{-7} \text{ m}^2 \cdot \text{s}^{-1}$) calculated with a 128 atom bcc cell. Previous ab-initio studies by Jiang *et al.* [81] and Domain *et al.* [38] calculated attempt frequencies of 10.79 THz and 15.69 THz ($D_0 = 1.44 \times 10^{-7} \text{ m}^2 \cdot \text{s}^{-1}$ and $D_0 = 2.13 \times 10^{-7} \text{ m}^2 \cdot \text{s}^{-1}$) using the Einstein approximation. Simonovic *et al.* [180] used both the dynamical matrix calculation and the Einstein approximation to obtain 12.44 THz and 16.18 THz ($D_0 = 1.66 \times 10^{-7} \text{ m}^2 \cdot \text{s}^{-1}$ and $D_0 = 2.16 \times 10^{-7} \text{ m}^2 \cdot \text{s}^{-1}$), respectively. However, Simonovic *et al.* used a small cell (32 + 1 atoms). Overall, our D_0 value is in good agreement with experimental studies (D_0 included between $1.67 \times 10^{-7} \text{ m}^2 \cdot \text{s}^{-1}$ and $2.0 \times 10^{-6} \text{ m}^2 \cdot \text{s}^{-1}$) [72, 101, 114, 119, 144, 179, 210]. The obtained C diffusion coefficients in cementite are in good agreement with the few carburization experimental data detailed in Sec. 2.1 (blue dots Fig. 2.5). C diffusion in cementite is found to be slightly anisotropic, with the lowest diffusion coefficient along the y -axis. In this direction, D_c is between approximately 2.5 and 4 times slower than in the other directions, for temperatures included between 500 K and 1000 K. C diffusion is faster in the x and z directions. This slight anisotropic behavior is due to a small difference between the lowest energy barrier in the xz plane (2.13 eV) and the lowest energy barrier along the y direction (2.16 eV). Even if the nearest distance between two C octahedral interstitials is slightly smaller along the y direction (3.36 Å instead of 3.37 Å), a C interstitial jumping in this direction must go through the C intrinsic atoms. As a result, the C interstitial migration in the y direction can either take place through an indirect mechanism, or an Octa - T3 - T3 - Octa direct mechanism. In both cases, the required energy is larger than for a direct migration path along the xz plane.

Levchenko and co-authors [104] also reported an anisotropic carbon diffusion, but

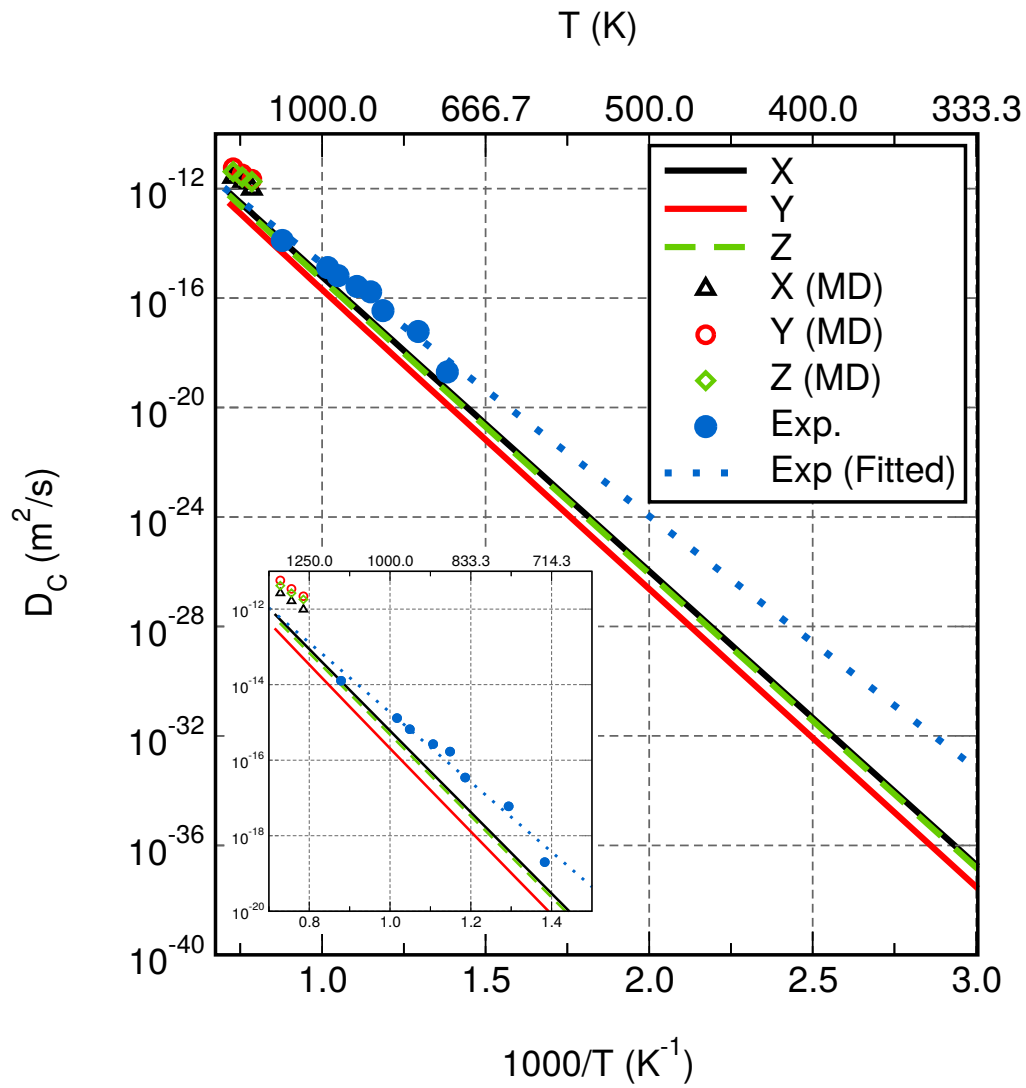


FIGURE 2.5: Arrhenius plot of diffusion coefficients of a C interstitial in Fe₃C cementite. The diffusion coefficients in all 3 cementite directions are plotted and compared with experimental data [66, 104, 140, 141, 163] (in blue). Empty symbols correspond to the values obtained by semi-empirical MD [104].

TABLE 2.7: Activation energy (Q) and pre-exponential factors (D₀) of carbon diffusion in cementite according to Arrhenius approximations of our study, Levchenko *et al.*'s MD study [104] and various experimental data [66, 104, 140, 141, 163]

direction	Our study			MD study [104]			Exp. studies ([66, 104, 140, 141, 163]) average
	x	y	z	x	y	z	
Q (eV)	2.13	2.17	2.13	1.50	1.45	1.26	1.83
D ₀ (m ² .s ⁻¹)	3.45.10 ⁻⁵	1.79.10 ⁻⁵	2.71.10 ⁻⁵	8.14.10 ⁻⁷	11.94.10 ⁻⁷	1.75.10 ⁻⁷	3.13.10 ⁻⁶

with the lowest diffusion coefficient in the x direction. Overall, Levchenko *et al.* with C diffusion via Frenkel pairs overestimates the diffusion coefficients of carbon in cementite (by a factor of 10 approximately), while with our interstitial diffusion mechanisms, the calculated diffusion coefficients are slightly lower than the experimental results (also by a factor of 10 approximately). A detailed comparison between the activation energies and the pre-exponential factors is given in Table 2.7. The experimental activation energy and pre-exponential factors are included between our values and the MD values. Please note that the kinetic correlation factors that we obtain range between 0.75 and 1.00 (see Fig. 2.6) which demonstrates the fact that C atoms are not performing a random-walk on the network of interstitial sites and that the relevance of correlation effects depends on the diffusion direction. Overall, there is no correlation effect in the y and z directions ($f \cong 1$), whereas the correlation factor is generally smaller along x .

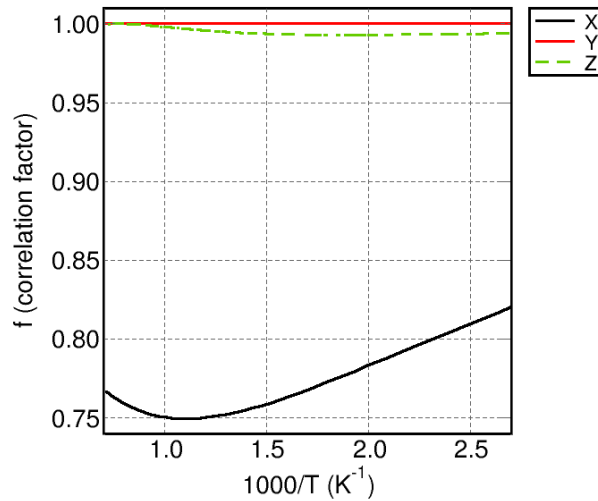


FIGURE 2.6: Correlation factors for C diffusion on interstitial octahedral sites calculated in the x , y and z directions.

As explained in Sec. 2.2, an atomistic study of cementite properties across the magnetic transition is beyond the scope of our study. Nevertheless, we estimated the impact of the paramagnetism in cementite on the formation energies of a C interstitial in an octahedral or a T3 site. To this end, we performed additional calculations using the previously relaxed ferromagnetic cementite structures (with and without a C interstitial), but with a special quasi-random structure (SQS) of Fe magnetic moments. Then, we replaced the total energies of the second and third terms of Eq. 2.7 by the total energies of the same cell, but with the Fe atoms in the paramagnetic state. Since the carburization experiments (with the exception of Hillert and Sharp work [66]) were performed below the Curie temperature of iron, we kept the chemical potential of iron in its ferromagnetic bcc state. We found an average formation energy of 0.75 eV for a C interstitial in an octahedral site and an average formation energy of 2.46 eV for a C interstitial in a T3 site in the paramagnetic (magnetic SQS) cementite. These formation energies are slightly above the ferromagnetic cases (0.64 eV and 2.39 eV respectively), but the energy difference between the two interstitial sites is negligible. This energy difference is involved in various migration barriers.

These results suggest that the present results on the C diffusion properties in the ferromagnetic cementite provide a rather satisfactory description of these properties in the paramagnetic cementite.

2.5 Effect of an alloying element on C interstitial diffusion in cementite

2.5.1 Interaction between an alloying element (Mo,Cr,Mn) and a C interstitial

Mo, Mn and Cr transition-metal solutes are known to favor the formation of carbides (for example the cementite, the $M_{23}C_6$, the M_2C etc.) in ferritic steels. The presence of an alloying element in Fe_3C can locally affect the energetic stability of the C octahedral interstitials and the migration energy barriers in the vicinity of the solute. This is why we also investigated the impact of a substitutional Mo, Mn or Cr in the metallic sub-lattice of cementite. As a first step, we focused on the rather dilute case.

In practice, we replaced one Fe atom by one solute in our supercell containing 96 metallic-atom sites. The binding energy of a carbon interstitial - solute (C_{int} -M) pair in $Fe_{3n-1}M_1C_n$ cementite is given by:

$$E^b(Fe_{3n-1}M_1C_{n+1}) = E(Fe_{3n-1}M_1C_n) + E(Fe_{3n}C_{n+1}) - E(Fe_{3n-1}M_1C_{n+1}) - E(Fe_{3n}C_n), \quad (2.9)$$

with $E(Fe_{3n-1}M_1C_n)$ and $E(Fe_{3n}C_{n+1})$ the total energies of cementite, with a substitutional M or with a C interstitial, respectively. $E(Fe_{3n-1}M_1C_{n+1})$ is the total energy of low-alloyed cementite with a C interstitial and $E(Fe_{3n}C_n)$ is the total energy of Fe_3C cementite. This formula can be seen as the total energy of each individual reactant, minus the total energy of each product of a reaction. According to this convention, positive binding energy means attraction. We examined all possible octahedral C sites around the solute up to a 4.20 Å distance, and calculated the corresponding binding energies. The results are presented Fig. 2.7. Mo_s and Mo_g solute configurations provide both repulsive and attractive C interstitial sites. Mn solutes configurations produce some attractive sites for short solute - C_{int} distances. All Cr - C_{int} configurations have zero or negative binding energies, with the exception of a Cr_g - C_{int} close (1.90 Å) pair. Overall, all the absolute values of the calculated binding energies are rather small (lower than 0.14 eV).

In order to rationalize the binding behavior, we first investigated the role of the solute atomic size on its interaction with the C interstitial. To this end, we compared the changes in the Voronoi volumes of the substitutional sites in cementite. The volume variation of a given site, due to the presence of a C_{int} and a substitutional solute (ΔV), is given by:

$$\Delta V = \Delta V_C + \Delta V_M \quad (2.10)$$

With ΔV_C the change of volume induced by the insertion of the C interstitial in Fe_3C and ΔV_M the change of volume induced by the substitution of a Fe atom by a solute M in a cementite cell containing a C interstitial. The results are shown in Fig. 2.8. The interaction of the Mo - C_{int} pairs is mostly governed by the size effect of the

Mo solute, which has a significantly larger atomic radius than Fe. In Fig. 2.8, we clearly observe that the binding energy of the Mo - C_{int} pair increases with ΔV_C . The substitution of Mo is favored in the dilatation sites caused by the C_{int} insertion. Overall, the Mo - C_{int} binding energy increases with ΔV_C and ΔV .

It is worth comparing these results with the effects of Mo in bcc Fe. Liu et al. [111] used DFT to systematically investigate the effect of dilute substitutional solutes on an interstitial carbon in α -Fe. They found that the interactions between Mo and a C octahedral interstitial up to the 4nn distance are repulsive, especially in the 1nn case. These results are also in agreement with Ref. [16]. In our study, we also found that at short distances C_{int} - Mo pairs in cementite are mostly repulsive, as in bcc Fe, and we obtained some attractive C - Mo pairs for larger distances (between 3 Å and 4 Å). At variance, in the case of a Mn solute, the binding energy of the solute - interstitial pair decreases with increasing ΔV_C . Finally, we did not observe a Voronoi volume dependence for a Cr solute. Please note that, as Mn and Cr atoms admit a size close to that of iron atoms and the change of volume induced by the substitution is not significant ($\Delta V \approx \Delta V_C$), and, the interaction between C and a Mn or Cr solute should be mostly governed by more complicated effects, such as magnetism or electronic charge redistribution.

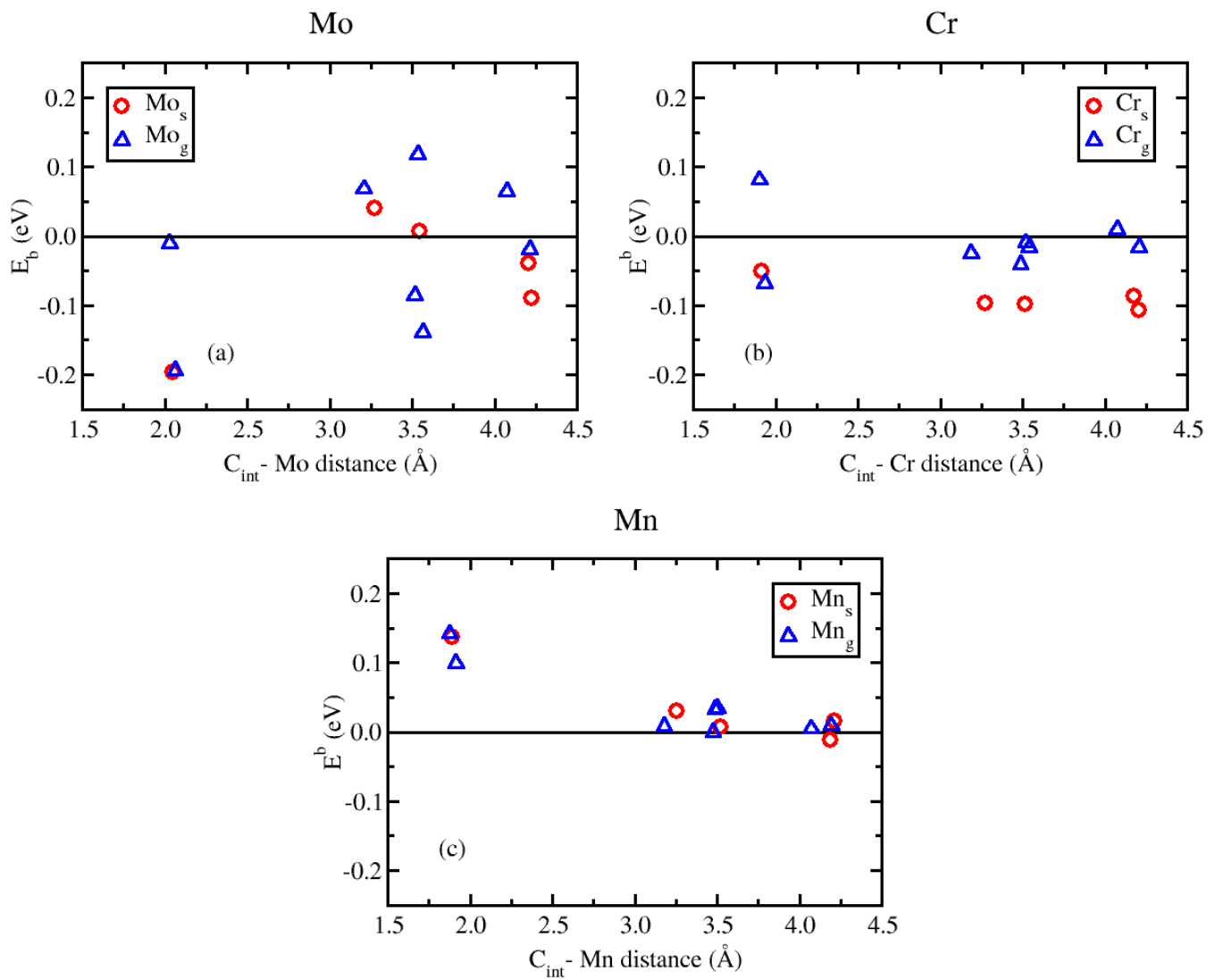


FIGURE 2.7: Binding energies of the carbon interstitial-metallic solute pairs, up to a 4.20 Å $C_{\text{int}} - M$ distance for $M=\text{Mo}$ (a), $M=\text{Cr}$ (b) and $M=\text{Mn}$ (c). The two metallic sub-lattices of cementite (M_s and M_g) are considered. According to the binding energy (E^b) defined previously, positive binding energies are associated with attractive pairs.

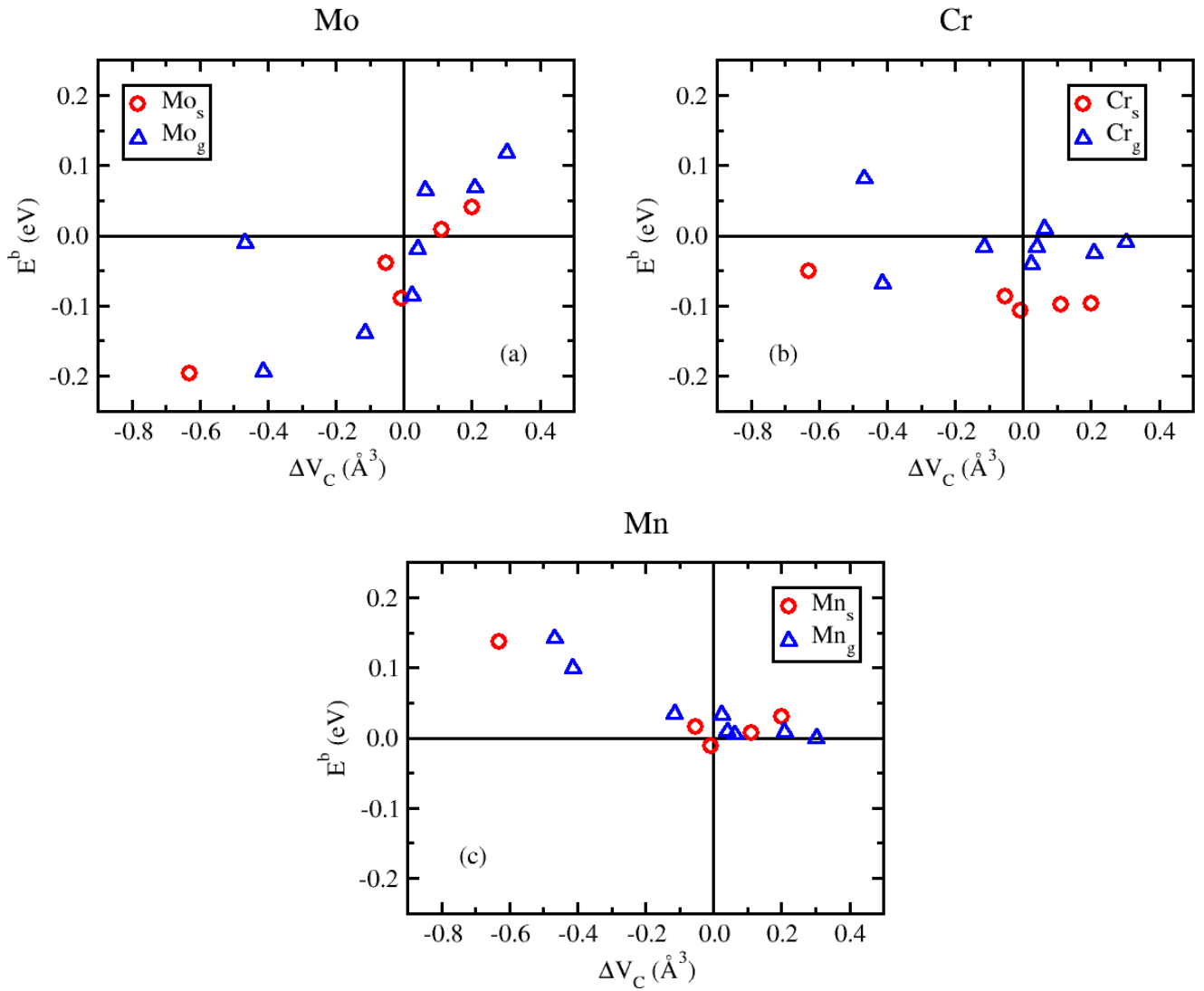


FIGURE 2.8:

(a), (b) and (c): Binding energies of a M (M=Mo, Cr and Mn respectively) metallic solute - C octahedral interstitial pair in $Fe_{95}M_1C_{33}$ versus the change in the substitutional site Voronoi volume induced by the insertion of the interstitial before the substitution (ΔV_C).

The two metallic sub-lattices of cementite (M_s or M_g) were considered. According to the binding energy (E^b) defined previously, positive binding energies are associated with attractive pairs.

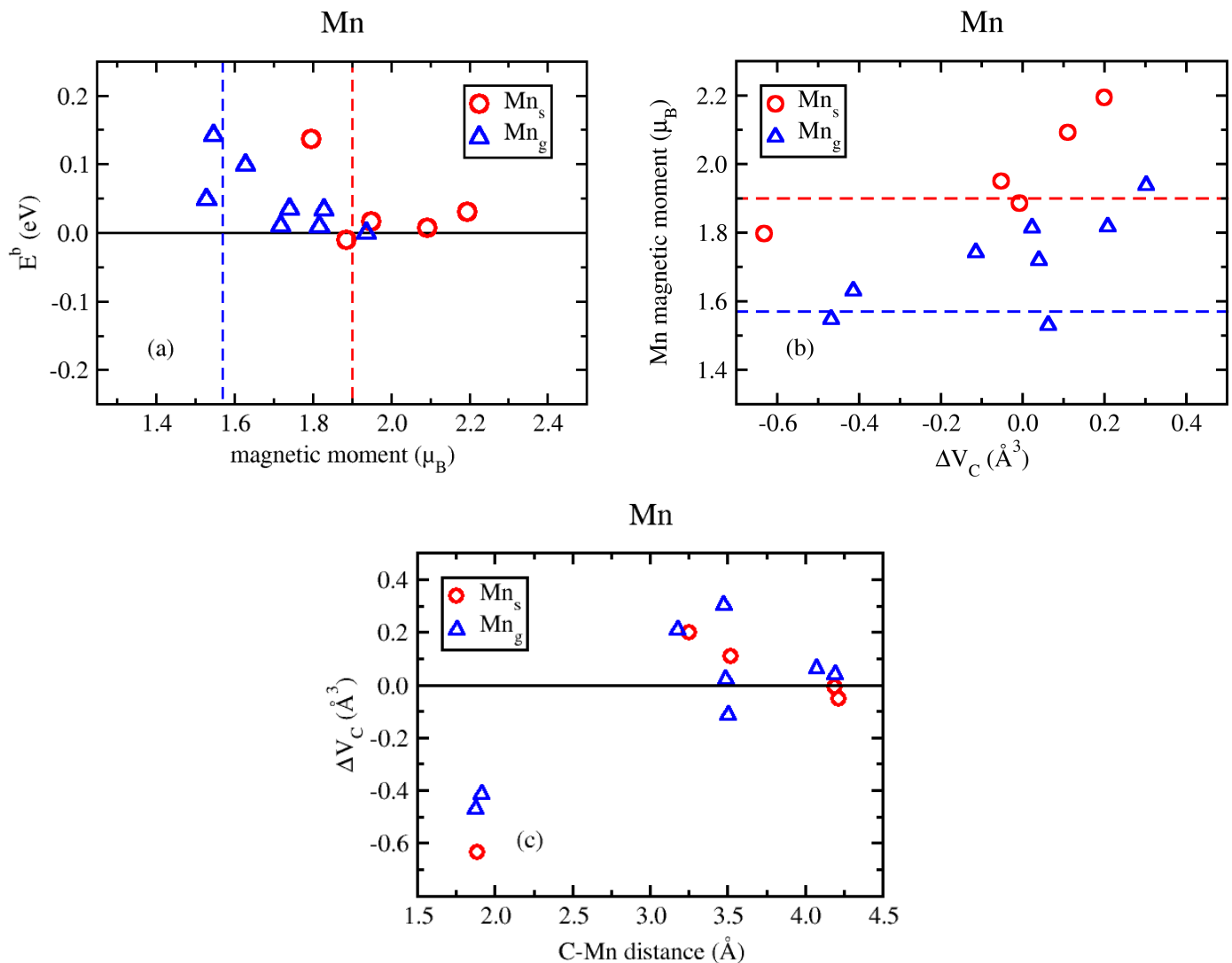


FIGURE 2.9:

- (a): binding energy of a C interstitial - Mn pair in $Fe_{95}Mn_1C_{33}$ according to the magnetic moment of the Mn solute.
- (b): magnetic moment of the Mn solute atom according to the change in the substitutional site Voronoi volume induced by the insertion of the C interstitial before the substitution (ΔV_C).
- (c): change in the substitutional site Voronoi volume induced by the insertion of the C interstitial before substitution (ΔV_C) as a function of the C interstitial - Mn solute distance.

The two metallic sub-lattices of cementite (Mn_s or Mn_g) were considered. According to the binding energy (E^b) defined previously, positive binding energies are associated with attractive pairs. The red and blue dashed lines represent the magnetic moment of the Mn_s and a Mn_g (energetically most favorable) solute in bulk cementite, respectively.

The magnetic moment of a Mn solute in $Fe_{95}Mn_1C_{32}$ is parallel to the Fe moments ($1.90 \mu_B$ and $1.57 \mu_B$ for Mn_s and Mn_g atoms, respectively). Cr solutes in the $Fe_{95}Cr_1C_{32}$ system has a $-0.82 \mu_B$ (Cr_s) and $-0.98 \mu_B$ (Cr_g) antiferromagnetic with respect to the Fe spins. These values are in good agreement with Ande *et al.* first-principle study [10]. We investigated the change in Mn and Cr magnetic moments induced by the introduction of a C octahedral interstitial. In the case of a Mn solute, we observed a correlation between Mn - C_{int} binding energy and the solute magnetic moment, as shown in Fig. 2.9: small Mn_s and Mn_g magnetic moments (which are closer to their respective moments far from the C interstitial) are associated with more significant binding energies, while higher Mn magnetic moments are associated with nearly-zero binding energy pairs. This trend is fully consistent with the binding energy dependency on the ΔV_C , because of the magneto-volume effect (see Fig. 2.9).

To further illustrate the relevant role of magnetism on the Mn - C_{int} binding, we performed additional DFT calculations for the short Mn - C_{int} distances ($< 2 \text{ \AA}$). We imposed the Mn solute magnetic moment to zero and relaxed the magnetic moments of all other atoms in cementite with or without a C interstitial. We replaced the total energies of the second and fourth terms of Eq. 2.9 by the total energies of the same cell with the zero-magnetic moment Mn. Overall, Mn magnetism enhances the Mn - C_{int} attraction: if we constrain the moment of Mn to zero, the binding energy decreases by 0.12 eV for a Mn_s solute and by 0.07 eV for a Mn_g solute. The Mn_s are more penalized by turning-off its magnetism because its fully relaxed magnetic moment is larger, due to a smaller number of intrinsic C nearest neighbors, and consistently, a larger Voronoi volume.

In bulk Fe, according to theoretical studies [16, 111, 121, 162], a Mn solute has a weak attractive interaction with its nearest C interstitial neighbor. This Mn - C_{int} attractive interaction was also predicted by experimental studies [2, 118]. In addition, nearest Mn - C_{int} neighbors are associated with the largest compression site (lowest ΔV_C) and the lowest Mn ferromagnetic moment. This lowest magnetic moment is close to the metastable moment of an isolated ferromagnetic Mn in bulk bcc Fe [162]. We find indeed some similar behavior in the Mn-alloyed cementite: high binding energies correspond to short Mn - C_{int} distances which themselves correspond to low Mn ferromagnetic moments.

Finally, in the case of a Cr solute, C_{int} - Cr pairs in cementite are all slightly repulsive or zero, with the exception of the shortest distance (Fig. 2.7). We did not evidence any clear trend of binding energy versus Cr magnetic moment. Cr solutes in the vicinity of a C_{int} ($Cr - C_{int} < 2 \text{ \AA}$) have very low magnetic moments (between $-0.22 \mu_B$ and $0.12 \mu_B$), while for larger distances, the Cr magnetic moment is close to the one in bulk $Fe_{95}Cr_1C_{32}$. In order to understand the attraction on the shortest Cr - C_{int} distance pair, we compared the partial density of state and differential charge density of various C - Cr distances. The study of the partial density of states of short ($< 2 \text{ \AA}$) Cr - C_{int} pairs established an hybridization between the solute $3d$ states and the C $2p$ states, as occurs for any close Fe - C pairs. However, in the only positive binding energy case (shortest Cr - C_{int} distance) we also observed an additional $4s$ - $2p$ hybridization between the Cr solute and the C interstitial. This difference in the solute - interstitial hybridization is also reflected in the differential electronic charge density $\Delta\rho$ induced by the C interstitial:

$$\Delta\rho = \rho(Fe_{95}M_1C_{32} + C_{int}) - \rho(Fe_{95}M_1C_{32}) - \rho(C), \quad (2.11)$$

with $\rho(Fe_{95}M_1C_{32} + C_{int})$ the total charge density of cementite with a C interstitial

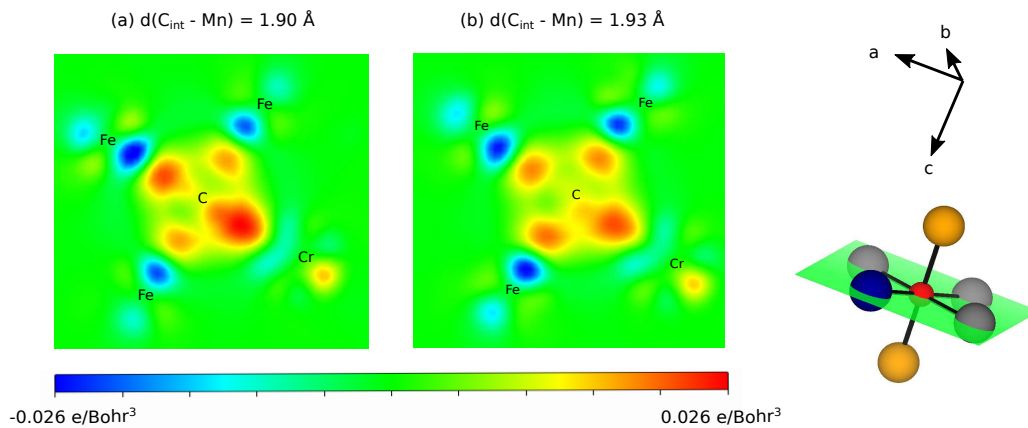


FIGURE 2.10: Charge density differences induced by the insertion of a C interstitial in $\text{Fe}_{95}\text{Cr}_1\text{C}_{32}$, for two close Cr solute - C interstitial pairs. Panel (a) is the lowest C interstitial - Cr solute distance possible in cementite, with an attractive binding energy. Panel (b) is a repulsive configuration. The corresponding plane of the octahedral cite is represented on the left. As in Fig 2.2, Fe_s atoms are in orange, while Fe_g atoms are in grey. The Cr solute is in blue, while the C interstitial octahedral site is in red.

and a substitutional atom M , $\rho(\text{Fe}_{95}M_1\text{C}_{32})$ the total charge density of cementite with a substitutional M , and $\rho(\text{C})$ the total charge density of the C interstitial isolated. In Fig. 2.10, we clearly see that in the configuration with the shortest Cr - C interstitial distance, the insertion of the interstitial induces an enhanced accumulation of charges in the Cr solute - C interstitial - Fe axis, in comparison with a repulsive Cr - C_{int} pair configuration. Regarding the C interstitial - Cr solute pairs in bulk bcc Fe, first principles studies [111, 160] all predicted repulsive Cr - C_{int} interactions.

To summarize, the Mo - C_{int} and Mn - C_{int} binding energies are dictated by the size effect and the solute magnetism, respectively, while the Cr - C_{int} interaction is rather due to a more subtle electronic hybridization effect.

2.5.2 C migration barrier in the vicinity of an alloying element

Although the binding energies found are not very large, the attractive sites may still act as traps for the diffusing C interstitials. The presence of the solutes could locally induce a change of the C migration barriers. The most relevant C migration barriers to investigate are:

- (i) barriers between two neighboring C attractive sites. If the barrier is rather low, the C interstitial can be caught in a cage movement. Such cage movements occur for instance during the migration of a C interstitial in α -Fe in the vicinity of a vacancy [19].
- (ii) the dissociation barriers for C to leave an attractive site.

To determine if cage movements can appear in cementite with a Mo, Mn or Cr solute, we calculated the energy barriers between two neighboring attractive C octahedral sites in the vicinity of a substitutional solute. For each set of initial and final positions with non-negligible binding energies ($E^b \geq 0.05$ eV), we considered the lowest energy migration path in pure Fe_3C cementite, and calculated the new energy barrier, impacted by the nearby substitutional solute. Results are shown in Table 2.8. Overall, the migration barriers associated with neighboring attractive sites in the alloyed cementite are never significantly lower than the corresponding migration barriers in pure Fe cementite. Therefore, no significant cage movement was identified. Since we found only one attractive site in the Cr-alloyed cementite case, we did not investigate cage movement in the vicinity of a Cr solute.

We also investigated the energetic barriers in the case of a dissociative migration. Due to the significant number of attractive sites induced by the presence of a Mo, Mn or Cr solute in cementite, as well as the numerous possible jumps from each attractive site to a non-attractive site, we could not compute all the migration barriers associated with a dissociation. We therefore chose to focus on dissociative migrations between the most attractive sites and a zero (or almost zero) binding energy sites. We prioritized the calculations of energy barriers linked with a direct migration path in the xz plane (the Octa - T3 - T2 - Octa migration described previously), because those are the lowest in Fe_3C . A non-exhaustive list of some possible energy barriers associated with dissociation movements is given in Table 2.9. Similarly to energy barriers associated with potential cage movement, the energy barriers associated with dissociative jumps in the case of Mo or Cr are approximately the same as in pure Fe cementite. However, in the case of a Mn solute, some energy barriers are slightly lower than in Fe_3C . Considering the calculated binding energies and barriers, we would not expect a significant effect of alloying elements on the C diffusion (at least in the dilute regime), except maybe in the presence of Mn, which is confirmed below.

TABLE 2.8: Migration energy barriers between two neighboring attractive C octahedral interstitials in cementite with a Mo or Mn solute. The binding energies before (initial) and after (final) the C jump are given at constant pressure (Pct) and at constant volume (Vct) at which the NEB calculations were performed.

Type of metallic solute	Binding energies (eV) initial/final Pct (Vct)	Jump mechanism (barrier in unalloyed Fe_3C)	Energy barrier in alloyed Fe_3C (forward/backward) (eV)
Mo _s	0.04/0.04 (-0.01/-0.01)	Indirect along y axis (2.16 eV)	2.25
Mo _g	0.12/0.07 (0.08/0.02)	Direct along the xz plane (2.13 eV)	2.14/2.08
Mn _s	0.10/0.10 (0.09/0.09)	Indirect along y axis (2.16 eV)	2.44
Mn _g	0.12/0.07 (0.08/0.05)	Direct along the xz plane (2.13 eV)	2.31/2.28

TABLE 2.9: Migration energy barriers associated with a dissociative jump in cementite around a Mo, Mn or Cr solute. The binding energies before (initial) and after (final) the C jump are given at constant pressure (Pct) and at constant volume (Vct) at which the NEB calculations were performed.

Type of metallic solute	Binding energies (eV) initial/final Pct (Vct)		Jump mechanism (barrier in unalloyed Fe ₃ C)	Energy barrier in alloyed Fe ₃ C (forward/backward) (eV)
Mo _g	0.12/-0.01	(0.08/-0.08)	Direct along the <i>xz</i> plane (2.13 eV)	1.92/1.76
Mo _g	0.12/0.00	(0.08/-0.05)	Indirect along <i>y</i> axis (2.16 eV)	2.28/2.16
Mo _g	0.12/0.00	(0.08/-0.15)	Indirect along <i>y</i> axis (2.16 eV)	2.25/2.01
Mn _s	0.14/0.01	(0.09/-0.04)	Direct along the <i>xz</i> plane (2.13 eV)	2.21/2.09
Mn _g	0.14/0.00	(0.08/-0.05)	Direct along the <i>xz</i> plane (2.13 eV)	2.19/2.05
Mn _g	0.14/-0.01	(0.08/-0.04)	Direct along the <i>xz</i> plane (2.13 eV)	2.12/1.99
Cr _g	0.08/-0.01	(0.02/-0.05)	Direct along the <i>xz</i> plane (2.13 eV)	2.14/2.07
Cr _g	0.08/0.01	(0.02/-0.04)	Direct along the <i>xz</i> plane (2.13 eV)	2.14/2.08

2.5.3 Effects of the substitutional solutes on C diffusion in cementite

In the previous sections, we have presented the binding energy between an interstitial C atom and a substitutional solute (Mo, Cr or Mn), as well as the carbon migration energies around the solutes. In this section, we use these data as inputs for the KineCluE code [167] to quantify the effect of the solute addition on carbon diffusion in cementite. Assumptions and calculation details for the determination of C diffusivity around solutes are explained in Sec. 1.1.3.

For each of the three solutes Mn, Mo and Cr, Fig. 2.11 shows the effect of their presence on the diffusivity of C atoms in cementite, as a function of temperature and the solute concentration. The quantity δD_C plotted on those graphs is the normalized difference between the carbon diffusion coefficients with and without the presence of the substitutional solute:

$$\delta D_C = \frac{\bar{D}_C([\bar{M}]) - D_C}{D_C}. \quad (2.12)$$

We considered solute concentrations up to a few at.%. Overall, the influence of the alloying elements on C diffusivity is small in weakly alloyed cementites. Mn is the solute with the most visible effect: C diffusion can be slowed down by a factor of 10 approximately at low temperatures (< 500 K) and in the presence of 1% of Mn and beyond. This can be expected because only the Mn solute has the most various attractive sites in its nearest-neighbor region, where the C interstitial can jump from one of these sites to another. This can induce some small trapping effects. In that respect, we found that dissociative jumps energy barriers are slightly higher in the case of Mn solute (see Table 2.9).

It is worth mentioning that, according to CALPHAD (CALculation of PHase Diagrams) data, cementite precipitates can indeed be present in Fe-Mn-C alloys. Using Thermo-Calc commercial software [12, 186] with the TCFE Steels/Fe-alloys version-10 database, we investigated the phases of Fe-Mn-C systems with a nominal Mn

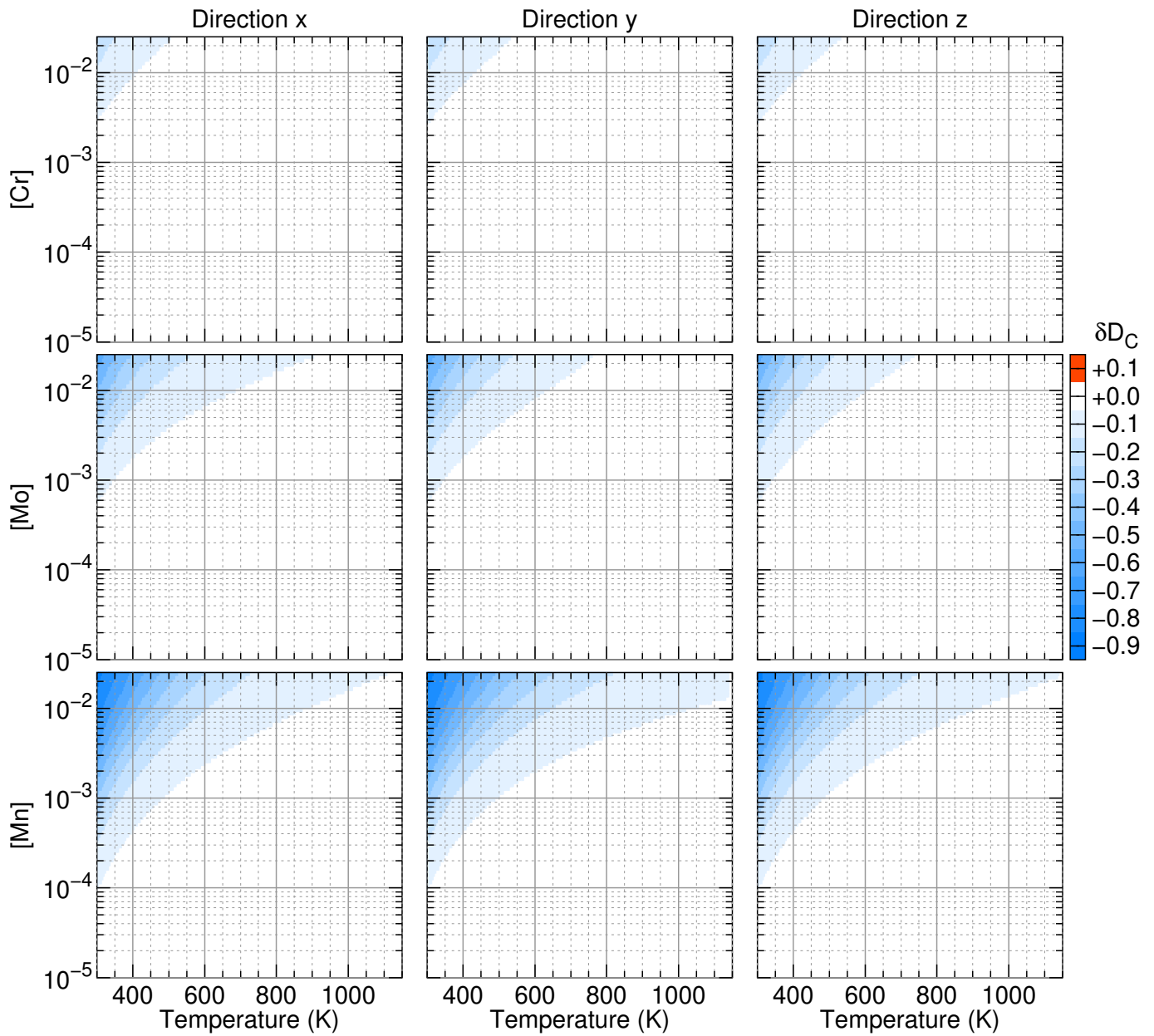


FIGURE 2.11: Effect of substitutional solutes Mo, Mn and Cr on the diffusion coefficient of carbon in cementite. The normalized difference between the carbon diffusion coefficients with and without the presence of the substitutional solute δD_C (defined in Eq. 2.12) is plotted as a function of the temperature and the solute concentration.

concentration up to approximately 5 at.%. For temperatures at which we predicted a visible influence of Mn on C diffusivity, the predicted Mn concentration in cementite phases is between 4 at.% and 23 at.% at 450 K and between 2 at.% and 30 at.% at 500 K, for Mn nominal concentrations below 2 %. Our current results suggest a decrease of C diffusion coefficients in these Mn-alloyed cementite. However, please note that our method used for the determination of C diffusion coefficients (with the KineCluE code) is only accurate for small alloying element concentrations (up to a few percents of metallic solute in cementite at most). For higher concentrations, interactions between Mn solutes would need to be considered.

2.6 Summary

We studied the relative stability of various defects (C vacancies, C interstitials, C Frenkel pairs) in stoichiometric Fe_3C .

We investigated the diffusion of carbon in pure and weakly-alloyed cementite, respectively Fe_3C and $(\text{Fe}_{1-x}\text{M}_x)_3\text{C}$ with $M = \text{Mo}, \text{Cr}$ or Mn . Systematic DFT calculations were performed to determine the formation energy of all identified single C interstitials, as well as the energy barrier of a large variety of jumps between the lowest-energy C interstitial configurations. Then, the KineCluE code was used to compute carbon diffusion coefficients in cementite using the DFT energetics as input data.

The obtained values in Fe_3C are in satisfactory agreement with experiments measuring the growth rate of cementite. Indeed, in such experiments, carbon diffusion was assumed as the rate-limiting mechanism governing the growth of cementite. The present study provides information on carbon migration mechanisms at the atomic scale, which is not directly accessible by experiments. We highlighted two elementary diffusion mechanisms: either a direct jump of a C interstitial from one octahedral site to another one, or an indirect jump where the C interstitial moves and takes the place of an intrinsic C, and the latter migrates towards an interstitial site.

It is interesting to note that although our predicted diffusion coefficients are comparable to the values from the previous semi-empirical MD simulation, the mechanisms at their origin are different. Indeed, the mechanism previously inferred from MD simulations relies on a high concentration of C Frenkel pairs (at least locally). With a higher C Frenkel pair formation energy, the MD based mechanism has a lower probability to occur. Alternatively, the present study proposes C to diffuse via interstitial mechanisms, involving jumps between octahedral interstitial sites. Please note that in those carburization experiments, the vapor phase acts as a source to provide C interstitials leading to the growth of cementite, the formation energy associated with the creation of interstitial C atoms is not involved in the activation energy of this process.

In order to investigate possible effects of the alloying elements (Mo, Cr and Mn) on the diffusion properties of C, we first calculated and analyzed the interaction energy between a C interstitial and one of the three substitutional solutes. Some energetically-favorable sites are found for a C interstitial around the solutes. The location of these sites are governed by the solute size effect, the solute magnetism

and the electronic charge redistribution, for the Mo, Mn and Cr case, respectively.

Regarding the influence of substitutional solutes on the C diffusion coefficients, we found that Mn decreases C diffusion coefficients by at most a factor of 10 at temperatures up to 500 K and solute concentrations up to a few at%. In the case of Mo and Cr, we predict no visible effects within the considered weakly alloyed conditions.

As a first step in the investigation of diffusion in cementite, this study considers stoichiometric cementite (M_3C). However, according to both experimental and theoretical studies [88, 102], C vacancy concentration in cementite could reach up to a few percent. The vacancies might play a significant role on C diffusion, which is undeniably an interesting perspective for a future study. For example, there may be a competition between our interstitial diffusion mechanism and Levchenko *et al.* C Frenkel pair mechanism for under-stoichiometric cementite and/or at high temperatures.

Most of these results are published in Physical Review Material [26].

Chapter 3

Alloyed M_3C and M_2C carbides: structural, energetic, electronic and magnetic properties

In this chapter, we investigate several properties of alloyed cementite (M_3C) and M_2C with a wide range of alloying concentrations. We mostly focus on the effect of Mo and Mn alloying in cementite, as well as Fe and Mn alloying in Mo_2C because Mo and Mn are common alloying elements in ferritic steels (for example in 16MND5 steels used in PWR vessels). The enthalpy of substitution is used to predict the partitioning behavior of Mo, Mn and Fe between cementite, Mo_2C and ferrite. The effect of the vibrational entropy and the magnetic disorder at finite temperature is discussed. Special attention is given to the comparison between DFT predictions and experiments. In particular, the variation of cementite volume upon alloying is compared in detail with Benarosch et al. experimental data.

3.1 State of the art

The precipitation of carbide phases can significantly modify steels properties. It is therefore crucial to control carbides population in steels in order to prevent premature aging and security issues. Two of the most common carbides in low-alloyed steels (for example 16MND5 steels) are cementite (Fe_3C) and a molybdenum carbide called Mo_2C . The addition of alloying elements is an easy way to (de)stabilize carbides. Stabilization of a carbide by an alloying element implies that this element preferentially moves from ferrite into the carbide phase, while destabilization implies that it is energetically more favorable for the alloying element to remain in ferrite.

Various experimental studies investigated the partitioning of alloying elements between ferrite and cementite. It is well-known that Cr and Mn are strong cementite stabilizer [5, 14, 15, 27, 93, 109, 113, 127, 129, 142, 147, 153, 157, 183, 187, 188, 195, 220]. Mo [93, 177, 187, 188, 195], V [93, 142, 195] and W [93, 177] also dissolve in cementite. On the other hand, Si [4, 14, 15, 93, 109, 127, 129, 183, 187, 195, 220], Al, Cu [127] and Co [93] prefer to stay in the ferrite. According to the processing, composition and concentrations, alloying element such as Nb, V, Ti and Ni can also

form other carbides phases or promote the emergence of fcc phases [93, 142, 195]. Efforts have been made to evaluate the effect of alloying elements in cementite from experiments. For example, properties such as the lattice parameters [83], Curie temperature and thermal expansion of alloyed cementite have been studied. However, it is difficult to access bulk cementite properties experimentally, because it is still challenging to obtain single-phases cementite samples [196]. First-principles methods are a good way to overcome these experimental difficulties. Various DFT studies investigated alloyed cementite stability and physical properties [9, 10, 30, 76, 95, 107, 116, 117, 122, 123, 134, 154, 171, 205, 209, 215, 219]. Nonetheless, previous calculations were limited to very dilute limit element concentrations, corresponding to the case of a single alloying element in cementite unit cell or supercell, as well as ordered configurations where all the alloying elements occupy the special or general sublattices (Fe_2MC) or FeM_2C). The only exception is VonAppen et al. study on the phase diagram of $(Fe_{1-x}Mn_x)_3C$ [205]. However, only cementite 16 atoms unit-cells were considered.

There are very few experimental data on Mo_2C (de)stabilization by alloying elements. To our knowledge, there is only one DFT study on Cr and Nb alloyed Mo_2C [112]. As in most DFT studies on alloyed cementite, this study only covers the case of a single solute in the carbide.

In first-principles study, conclusions on the (de)stabilization of carbides phases by alloying elements are usually based on the enthalpies of formation of the alloyed carbide with respect to the pure-element phase. However, Ande et al. [9, 10] have shown that carbide (de)stabilization should rather be described using the partitioning enthalpy, or *enthalpy of substitution* as we will call it from now on. Contrary to the formation enthalpies, the enthalpy of substitution takes into account the competition between the carbide and the bcc-Fe matrix.

As explained in the previous chapter, Fe_3C admits a low Curie temperature (approximately 473 K). Dick et al. [35] evaluated the magnetic free energy up to 1500 K using a spin quantum Monte-Carlo scheme. They also described the electronic and vibrational excitation in Fe_3C based on DFT calculations. However, to our knowledge, there is no study on the effect of the vibrational entropy or magnetic disorder of alloyed cementite at finite temperature. De Oliveira et al. [135] calculated the Helmholtz free formation energy of Mo_2C with Mo or C vacancy but so far, the entropy of alloyed Mo_2C is still unknown.

In the introduction, we mentioned that this work is part of a coupled project between applied metallurgy and fundamental research involving two thesis. In this chapter, a special attention is therefore being paid to the comparison between our results and data obtained by Benarosch et al. within the experimental part of our project [20]. Benarosch et al. results are sometimes emphasised, or discussed apart from previous experimental studies.

3.2 Interaction between Mo, Cr or Mn solutes in ferrite

In order to investigate the partitioning behavior of alloying elements in carbides, we must first understand their properties in ferrite (theoretically represented as bcc Fe with C atoms). Several DFT studies investigated the effect of a substitutional solute

in bcc Fe. It is widely known that the ground state of pure bcc Fe is ferromagnetic (FM). Using a $4 \times 4 \times 4$ Fe bcc supercell, we calculated a $2.21 \mu_B$ /atom magnetic moment and a lattice parameter of 2.833 \AA , in good agreement with previous ab-initio and experimental studies [64, 81, 91]. Then, we substituted a Fe atom by a Mo, Cr or Mn atom in the supercell.

In their ground state, Mo atoms are non-magnetic (NM). However, a single Mo solute admits a very small, negative magnetic moment in bcc iron induced by the interaction with neighboring Fe atoms. The ground state of a single Cr in bcc Fe is antiferromagnetic (AF) with respect to the lattice Fe moments [16, 34, 92, 137, 149]. In our study, we calculated a $-1.87 \mu_B$ magnetic moment for a Cr solute. Other DFT studies reported values included between $-2.36 \mu_B$ and $-1.29 \mu_B$ [34, 137]. Experimental data are included between $-1.29 \mu_B$ and $-0.55 \mu_B$ [7, 33, 178]. The magnetism of a single Mn solute has been a controversy. The reported Mn magnetic moment ranges from $-3.0 \mu_B$ (AF with respect to Fe moments) to $1.0 \mu_B$ (FM with respect to Fe moments) [34, 90, 137, 149, 162]. The value of this ground state magnetic moment is very sensitive to the DFT approximations such as the parametrization of the exchange-correlation functional or the choice of pseudopotential, as illustrated by Olsson et al. [137]. Recently, Schneider et al. [162] and King et al. [90] established (using PAW-PBE) that the real ground state of a single Mn in bcc Fe is AF with respect to the Fe lattice, with a very close flat local minima associated with a FM coupling. The magnetic moments of the AF ground states range between $-1.98 \mu_B$ and $-1.86 \mu_B$ [162] or $-2.08 \mu_B$ and $-1.89 \mu_B$ [90]. The estimated energy barriers between the AF and FM states are 0.07 eV [162] and 0.10 eV [90]. Based on these results, we chose the AF ground state for our Mn substitutional solute in bcc Fe and obtained a $-2.01 \mu_B$ moment.

The interaction between two close-pair solutes in bcc Fe has also been studied in the literature. All DFT studies predict repulsive Mo-Mo and Cr-Cr interactions, especially for the 1nn distance [16, 34, 54, 105, 137]. On the other hand, most DFT studies suggest that two Mn solutes can attract each other. Using the AF ground state of a single Mn in bcc Fe as the energy reference, Bakaev et al. [16] and Schneider et al. obtained a small attractive Mn-Mn binding energy for the 1nn. Olsson et al. obtained attractive Mn-Mn interactions for the 1nn and 2nn. King et al. compared the binding energies of Mn solutes using the AF or FM states as the energy reference for an isolated Mn solute in bcc Fe. They reported small attractive interactions up to the 6nn (FM reference state) and repulsive interactions (AF reference state). Finally, Vincent et al. [202], Gorbатов et al. [54] and Devi et al. [34] reported repulsive Mn-Mn binding energies for the 1nn, 2nn and/or 3nn. The disagreement between all these results is probably due to the different potentials and more generally to the different setup used for the calculations. Bakaev et al. predicted that the magnetic moments on two 1nn Mn are antiferromagnetic with respect to the moments of Fe atoms, with a total value reduced to $-0.6 \mu_B$. To our knowledge, they did not consider the possibility of a Mn dimer with one AF-Mn and one FM-Mn. On the other hand, Schneider et al. took into account all the possible magnetic states for the Mn-Mn pair and showed that Mn moments tends to be AF with respect to each other for the 1nn and 2nn distances, while they are AF with respect to the Fe lattice for larger distances. Similarly, King et al. obtained almost zero average magnetic moments for Mn-Mn 1nn. The Mn-Mn attraction for the first neighbors can be explained by the flexibility of the Mn magnetic moment, which can easily change and adapt according to its local environment.

Beyond the solute-solute pair in bcc Fe, the average binding energy (the attraction) of Mn clusters increases with the number of Mn involved [162]. In addition, Schneider et al. detailed magnetic analysis suggests that the Mn-Mn AF coupling is generally dominant over the Fe-Mn AF coupling. The average magnetic moment of the Mn atoms in bcc Fe tends to be AF to lattice Fe moments for Mn concentrations lower than a few atomic percents of Mn and FM to Fe moments for larger Mn concentrations [42, 162]. The mixing energy of Fe and Mn in bcc Fe reveals an unmixing tendency [163], in agreement with experimental values [128]. As for Cr solutes in bcc Fe, they display a magnetic behavior opposite to the Mn one: Fe-Cr AF interactions prevail over the Cr-Cr antiferromagnetism [42, 49]. Several DFT studies [92, 105, 136] noted a change of sign of the mixing enthalpy of Cr in bcc Fe, showing mixing tendency for low Cr concentrations and unmixing tendencies for higher Cr concentrations. This is consistent with the repulsive Cr-Cr binding energies: at low concentration, Cr atoms in Fe repel each other, causing ordering. There are less studies on the behavior of Mo solutes in bcc Fe. According to Lejaeghere et al. [103] and Udovsky et al. [192] ab-initio studies, Mo solutes display an unmixing tendency, in agreement with CALPHAD data [150]. In $Fe_{1-x}Mo_x$ bcc solid solution, Mo solutes admits a small induced moment, AF coupled with Fe magnetic moments [42, 172].

Steels contain carbon atoms. Many DFT studies investigated the behavior of a C atom in bcc Fe. It is well known that the insertion of a C interstitial in bcc Fe decreases the magnetic moment magnitude on the nearby Fe atoms [3, 19, 38]. The effect of a C interstitial on a dilute substitutional solute in bcc Fe was also studied. Theoretical results were discussed in the previous chapter (Sec. 2.5.1). To summarize, Liu et al. [111] and Bakaev et al. [16] found that the interactions between a Mo solute and a C octahedral interstitial in bcc Fe are repulsive up to the 4nn distance. First-principles studies also predict repulsive Cr - C interactions in bcc Fe [111, 160]. On the other hand, according to theoretical studies [16, 111, 121, 162], a Mn solute admits a weak attractive interaction with its nearest C interstitial neighbor. This Mn - C attractive interaction was also predicted by experimental studies [2, 118]. Interestingly, for this attractive 1nn distance, the magnetic moment of the Mn solute becomes FM with respect to Fe moments, while it stays antiferromagnetically coupled with Fe atoms for larger Mn - C distances [111, 162]. The magnetic moment of Cr atoms involved in a Cr - C pair in bcc Fe is always AF with respect to Fe atoms [111].

Cementite and Mo_2C carbides can form in ferrite. Understanding the interaction between alloying elements and carbon in this phase is the first step to study the partition of these elements between ferrite and carbides. It is therefore necessary to compare the properties of the alloying elements in each phase.

3.3 Structural, magnetic and energetic properties of Mo, Cr or Mn alloyed cementite

3.3.1 Magnetism of Mo, Cr or Mn alloyed cementite

Fe_3C ground state is ferromagnetic with a Fe magnetic moment of $1.96 \mu_B$ (Fe_s) and $1.88 \mu_B$ (Fe_g). As a first step for the study of alloying effect on cementite magnetism, we investigated the magnetic ground state of a single M (M=Mo, Cr or Mn) atom in cementite ($\approx 1\%$ of metallic sites). In its lowest-energy magnetic state, a single

Cr solute moment is antiferromagnetically coupled with the Fe moments in cementite. Conversely, in its ground state, a single Mn solute in cementite is ferromagnetic with respect to the Fe moments. Table 3.1 shows the Mo, Cr or Mn moments in $1 \times 1 \times 1$ and $2 \times 2 \times 2$ cementite cells. Our calculated magnetic moments are in good agreement with previous DFT studies [10, 122, 171, 215, 219] in the 16 atoms unit-cell ($\approx 8\%$ of metallic sites). The magnetic moment of a Mo solute in cementite is slightly AF with respect to the Fe magnetic moments. As for Fe atoms in pure Fe_3C , the amplitude of Mn or Cr magnetic moments is lower in general positions (noted Mn_g and Cr_g). Mn_g and Cr_g magnetic moments admit a lower amplitude because they have one more C nn and one less Fe nn with respect to solutes in special positions. In addition, Cr_g (Mn_g) presents a lower Voronoi volume than Cr_s (Mn_s), which is consistent with the magneto-volume effect. The magnetic behavior of a solute in cementite can be compared to the magnetic behavior of this solute next to a C atom in bcc Fe. As in cementite, the magnetic moment of a Cr atom either isolated or with a C neighbor in bcc Fe is antiferromagnetically coupled with the Fe moments (see Sec. 3.2). On the other hand, a Mn solute next to a C atom is only FM with respect to Fe moments if the C atom is very close (1nn). For larger Mn - C distances, the Mn solute is antiferromagnetically coupled with the Fe moments, which is not the case in cementite. Lastly, the small AF moment of Mo solutes is induced by the interaction with its Fe neighbors, as in bcc Fe.

To go beyond the case of a dilute solute in cementite, we study the change in cementite magnetization according to its Mo, Cr or Mn alloying content. Results are presented Fig. 3.1. Since Mo atoms are NM, we observe a magnetic dilution in $(\text{Fe},\text{Mo})_3\text{C}$ which increases with Mo concentration. The case of Cr and Mn solutes in cementite is less trivial. Beyond a given concentration, Cr solutes experience a competition between Cr-Fe AF coupling and Cr-Cr AF coupling. On the other hand, Mn solutes experience a magnetic frustration between the Mn-Fe FM coupling and the Mn-Mn AF coupling. As a result, for more than a few Cr or Mn solutes in cementite, there are a large number of magnetic configurations to consider, and the determination of the precise magnetic ground state is beyond our reach. In the scope of this study, as we are mainly interested in the dilute regime, we chose to initialize $(\text{Fe},\text{Cr})_{3k}\text{C}_k$ and $(\text{Fe},\text{Mn})_{3k}\text{C}_k$ calculations with Cr atoms antiferromagnetically coupled with Fe atoms and Mn atoms ferromagnetically coupled with Fe atoms (as predicted in the case of a single Cr or Mn solute in cementite). We assume that the results for high Mn or Cr concentrations in cementite will not strongly differ from the magnetic ground states and that the energetic trends presented in this study are overall correct. Up to roughly 50 percent of Cr in cementite, Cr atoms preserved their AF coupling with Fe atoms upon relaxation and lower the average magnetic moment. This is similar to the behavior of Cr solutes in bcc iron, for which the Fe-Cr antiferromagnetic coupling prevails [42, 49]. Beyond this concentration, the magnetic moment of Cr solutes becomes almost zero, probably because of subtle electronic effects due to the interplay between Cr - Cr and Cr - C interactions. An experimental data indicate a sharp decrease in Cr-alloyed cementite magnetic moment from $1.9\mu_B$ in Fe_3C to $0.4\mu_B$ in $(\text{Fe}_{0.80}\text{Cr}_{0.20})_3\text{C}$ [176]. This magnetic moment is significantly lower than our DFT predicted magnetic moment for 20% of chromium in cementite ($1.08\mu_B$). Nevertheless, DFT-GGA calculations also give a higher value for Cr magnetic moment in bcc iron [137]. The model Cr_3C cementite was found to be NM, in agreement with previous ab-initio studies [78, 95, 123, 134, 154, 215, 219]. Mn solutes magnetic behavior is very sensitive to their chemical environment. Up to approximately 10 % of Mn in cementite, all Mn solutes stay FM with respect to

Fe atoms. Beyond 10 % of Mn, the initial FM ordering is not maintained as some Mn solutes spins 'flip' and become AF with respect to Fe atoms to accommodate their environment. The presence of Mn solutes lead to a diminution of the average magnetic moment in Mn alloyed cementite with the increase in Mn concentration. In Jang *et al.* study [76], Mn_3C is defined as a NM structure. However, Razumovskiy *et al.* and VonAppen *et al.* [205] proposed two different antiferromagnetic ground states for Mn_3C . According to Razumovskiy and co-authors, each Mn sublattice admits an almost-zero magnetic moment in Mn_3C . On the other hand, Von Appen *et al.* describe Mn_3C ground state as an antiferromagnetic ordering for Mn_g and a ferromagnetic ordering for Mn_s , with a slightly positive total magnetic moment ($0.33 \mu_B$ per metallic atom). We calculated the total energy of FM, NM and both AF Mn_3C . We found that the energetically most favorable magnetic state is the AF ground state described by VonAppen *et al.*. Interestingly, during our calculation, Razumovskiy *et al.* AF structure relaxed toward VonAppen *et al.* AF magnetic ordering. This antiferromagnetic ordering is only slightly energetically more favorable (-25 meV/f.u.) than the NM state. Our calculated magnetic moment is in excellent agreement with Von Appen *et al.* value (see Figure. 3.1(c)) and fits nicely with the $0.37\mu_B$ magnetic moment per metallic atoms observed at higher temperature [39]. Other experimental data predict the existence of long-range antiferromagnetic ordering in Mn-rich cementites between 2 and 290 K [182]. We can see from Fig. 3.1 that the magnetic moment decreases upon Mo, Cr or Mn alloying is roughly linear in the dilute regime. The diminution of the average magnetic moment upon Mo, Cr or Mn alloying suggests a diminution of the Curie temperature of alloyed cementite. This Curie temperature change was experimentally observed in Mn [175, 193, 194] and Cr [175, 193, 195] alloyed cementite. In order to compare qualitatively the evolution of the Curie temperature and the evolution of the magnetic moment upon alloying, we measured the ratio between experimental data on alloyed cementite Curie temperature and Fe_3C Curie temperature and confronted it with the ratio between our predicted total magnetic moments. In particular, Shigemastu *et al.* [175] predicted that the Curie temperature of $(Fe_{0.97}Cr_{0.03})_3C$ is 1.14 times the Curie temperature of $(Fe_{0.94}Cr_{0.06})_3C$ cementite and the Curie temperature of $(Fe_{0.97}Mn_{0.03})_3C$ is 1.15 times the Curie temperature of $(Fe_{0.91}Mn_{0.09})_3C$. According to our DFT results, the magnetic moment of $(Fe_{0.97}Cr_{0.03})_3C$ is approximately 1.08 times the magnetic moment of $(Fe_{0.94}Cr_{0.06})_3C$ and the magnetic moment of $(Fe_{0.97}Mn_{0.03})_3C$ is 1.13 times the magnetic moment of $(Fe_{0.91}Mn_{0.09})_3C$. The correlation between our DFT magnetic moment and experimental Curie temperature is less good with respect to Umemoto *et al.* studies [194, 195]. For example, Umemoto *et al.* observed that the Curie temperature of Fe_3C is 1.23, 1.51 and 3.22 times higher than the Curie temperature of $(Fe_{0.95}Mn_{0.05})_3C$, $(Fe_{0.90}Cr_{0.10})_3C$ and $(Fe_{0.80}Cr_{0.20})_3C$. However, we calculated that the magnetic moment of Fe_3C is 1.23, 1.26 and 1.70 times the magnetic moment of $(Fe_{0.95}Mn_{0.05})_3C$, $(Fe_{0.90}Cr_{0.10})_3C$ and $(Fe_{0.80}Cr_{0.20})_3C$, respectively.

There is an interplay between the magnetism and the volume change in crystals (it is the so-called magneto-volume effect). In order to better understand the change of magnetization of cementite with Mo, Cr or Mn substitutional solutes, we studied the volume change upon alloying. This property is also compared with experimental data.

	solute type	reference	solute magnetic moment (μ_B)
Fe ₁₁ Mo ₁ C ₄	Mo _s	[this work]	-0.35
		[171]	-0.34
		[10]	-0.30
Fe ₉₅ Mo ₁ C ₃₂	Mo _s	[this work]	-0.31
Fe ₁₁ Mo ₁ C ₄	Mo _g	[this work]	-0.39
		[171]	-0.38
		[10]	-0.34
Fe ₉₅ Mo ₁ C ₃₂	Mo _s	[this work]	-0.39
Fe ₁₁ Mn ₁ C ₄	Mn _s	[this work]	1.94
		[171]	2.02
		[10]	1.87
Fe ₉₅ Mn ₁ C ₃₂	Mn _s	[this work]	1.90
Fe ₁₁ Mn ₁ C ₄	Mn _g	[this work]	1.51
		[171]	1.55
		[10]	1.30
Fe ₉₅ Mn ₁ C ₃₂	Mn _g	[this work]	1.57
Fe ₁₁ Cr ₁ C ₄	Cr _s	[this work]	-1.07
		[219]	-1.89
		[171]	-1.04
		[215]	-1.66
		[10]	-0.83
		[122]	-0.58
		[116]	-1.37
[134]	-1.25		
Fe ₉₅ Cr ₁ C ₃₂	Cr _s	[this work]	-0.82
Fe ₁₁ Cr ₁ C ₄	Cr _g	[this work]	-0.96
		[171]	-0.93
		[215]	-1.80
		[10]	-0.84
		[122]	-0.51
		[116]	-0.03
[134]	-0.01		
Fe ₉₅ Cr ₁ C ₃₂	Cr _g	[this work]	-0.98

TABLE 3.1: Magnetic moment of a Mo, Mn or Cr solute in $1 \times 1 \times 1$ (Fe₁₁M₁C₄) or $2 \times 2 \times 2$ (Fe₉₅M₁C₃₂) cementite cell (M=Mo, Cr or Mn).

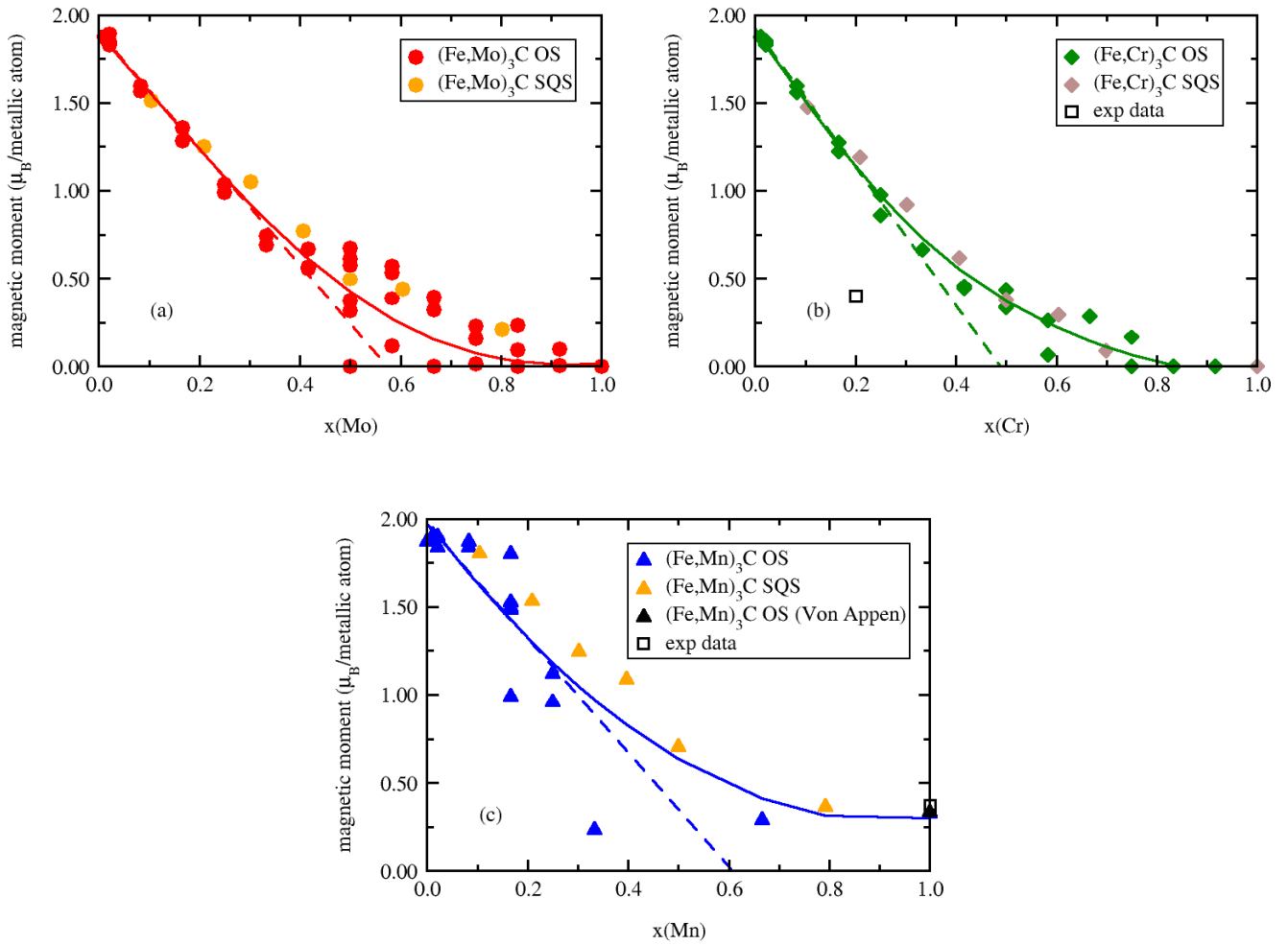


FIGURE 3.1: (a), (b) and (c): Average magnetic moment of metallic atoms in alloyed cementite according to the Mo, Cr or Mn alloying element concentration, respectively. We differentiate $(Fe,M)_3C$ configurations with ordered structures or solute clusters (OS) from configurations with a completely random distribution of solutes (SQS configurations). We performed linear regressions (dashed lines) for alloying elements concentrations below 30 percent to show that the decrease in magnetic moment is roughly linear in this concentration range. The experimental data for Cr alloyed cementite and Mn alloyed cementite are from Shigamestu *et al.* [176] and Von Appen [205] *et al.* studies, respectively.

3.3.2 Volume of Mo, Cr or Mn alloyed cementite

Since all our DFT calculations were performed at constant pressure, we investigated the volume change induced by the substitution of Fe atoms of cementite by an alloying element. According to our results, the volume of 'pure' Fe₃C is 12.633 Å³/metallic atom at 0 K. Previous first-principles studies predicted values included between 12.340 and 12.933 Å³/metallic atom [28, 35, 43, 51, 58, 62, 70, 76, 80, 95, 116, 117, 133, 154, 171, 215, 216, 219]. Please note that when a reference only gives the lattice parameters of cementite, we multiplied them to obtain the volume of the orthorhombic unit cell. By comparison, experimental data obtained at room temperature vary between 12.865 and 12.949 Å³/metallic atom [37, 44, 63, 106, 195, 213]. This is slightly above our predicted value. However, when fully relaxing our supercell, we assume that the supercell experiences no external stress. This might be true in massive bulk material, but it is still complicated to obtain single-phase samples of Fe₃C. In most of the experiments cited above, the carbides precipitates in a matrix and their volume may depend on their environment and the fabrication procedure. For example, Yelsukov *et al.* showed that the average cementite grain size increases with the annealing temperature [217]. Recently, Umemoto *et al.* [195] achieved the fabrication of bulk cementite by combining mechanical alloying with spark plasma sintering. They reported a Fe₃C volume of 12.949 Å³/metallic atom. A few experimental studies also investigated the lattice parameters of Mn₃C and Cr₃C [47, 74, 100]. Such phases can for example be fabricated through rapid quenching in binary M-C samples. The volume per atom of Mn₃C and Cr₃C observed experimentally are 12.986 Å³/atom and 13.288 Å³/metallic atom, respectively. As for Fe₃C, these volumes are higher than our theoretical values.

Fig. 3.2 shows the volume per atom of all our (Fe,M)₃C configurations (with M=Mo, Cr and Mn) according to the alloying element concentration. Because the absolute values of the volume depends on the approximation of the calculation scheme, we also checked the change in volume versus solute concentration. Mo has a significantly larger atomic radius than Fe, Cr and Mn. As a result, the volume change in Mo alloyed cementite is much higher than the volume change in Cr or Mn alloyed cementite. The volume of Mo alloyed cementite increases linearly with the Mo concentration. This behavior closely follows the Vegard's law. The volume of (Fe,Mn)₃C also seems to decrease linearly up to intermediate Mn concentration (more or less 30% of Mn) in cementite. However, the calculated volume of Mn₃C does not follow the Vegard's law extrapolation. With increasing Mn contents, Mn alloyed cementite undergoes a change of magnetic behavior which could explain the deviation from the linear tendency predicted at lower concentrations. The volume of Cr alloyed cementite does not evolve linearly with the Cr concentration. Fe_{1-x}Cr_xC volume decreases up to $x = 0.33$ and increases for Cr concentration above this value. The diminution of the volume upon Cr alloying is roughly linear up to approximately 25% of Cr in cementite. Our Fe_{1-x}M_xC volumes are in good agreement with data from previous DFT studies.

The volume change in Mo alloyed cementite is linear. It is also roughly the case up to 30% of Mn and 25% in M₃C. According to these results, one could estimate the concentration in Mo or moderately Cr or Mn alloyed cementite phases observed experimentally from their volumes. Kagawa *et al.* [83] measured experimentally the lattice parameters and volume of cementite in Fe-C-X (X=Cr, Mn, Mo, and Ni) alloys. After annealing, they obtained cementites phases with alloying contents up to 2at%,

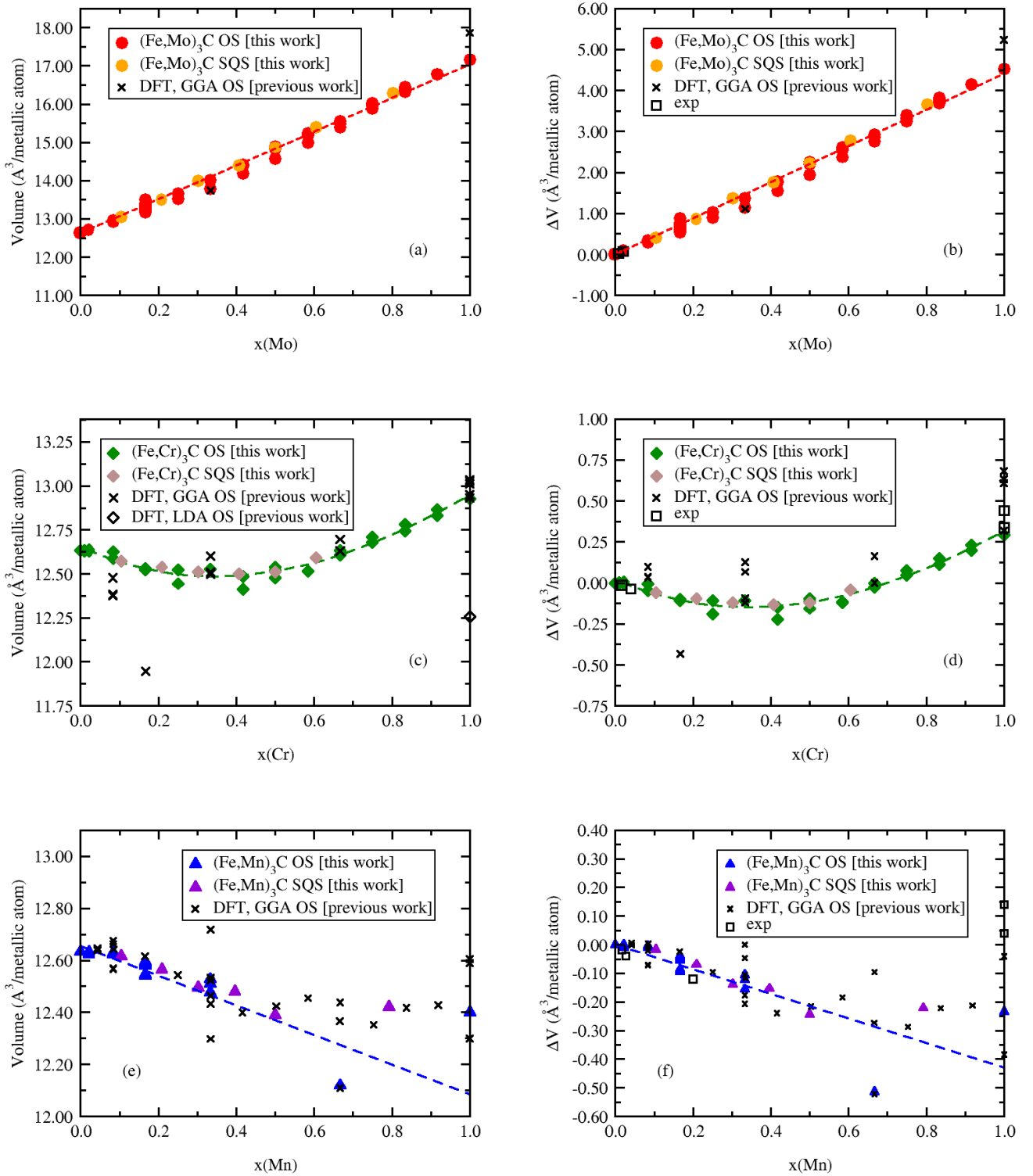


FIGURE 3.2:

On the left side, (a), (c) and (e): Volume per metallic of Mo, Cr and Mn alloyed cementite, respectively, according to the alloying element concentration.

On the right side, (b), (d) and (f): Associated volume change $\Delta V = V(Fe_{1-x}M_xC) - V(Fe_3C)$ for $M=Mo$, Cr or Mn alloyed cementite, respectively, according to the alloying element concentration.

We differentiate $(Fe,M)_3C$ configurations with ordered structures or solute clusters (OS) from configurations with a completely random distribution of solutes (SQS configurations).

The previous DFT data are from Ref. [9, 10, 30, 44, 51, 70, 116, 122, 154, 171, 205, 216, 219] and the experimental data are from Ref. [47, 74, 83, 100]. Regarding experimental values, when the volume of pure Fe_3C is not specified in a given study, we use Wood *et al.* [213] experimental value at room temperature to approximate ΔV .

3.96at% and 5.28at%, for Mo, Cr or Mn alloyed cementite, respectively. They found that Cr and Mn alloying decreases the volume of cementite unit cell, while Mo alloying remarkably increases the unit cell volume. Even if their reported volumes per cell are above our DFT results, their volume changes are in good agreement with our values (see black squares below 10% of alloying elements in Fig. 3.2). Additional isolated experimental data [47, 74, 83, 100] regarding the volume of alloyed cementite phases were also added in this figure. When the volume of Fe₃C is not specified in a given study, we used Wood et al. experimental value at room temperature to approximate ΔV . However, Mn₃C volume changes obtained with this approximation do not agree well with our DFT results.

Recently, Benarosch et al. used X-ray diffraction analysis with Rietveld refinements to access the volume of carbides phases in Fe-Mo-C and Fe-Mn-C model steels at room temperature. They also followed the content in alloying elements of each phases with SEM-EDS (Scanning Electron Microscopy - Energy Dispersive X-ray Spectroscopy). They measured Mo concentrations in cementite included between 1% and 3% and Mn concentrations in cementite included between 1% and 14%. A comparison between their results (private communication [20]), previous experimental data [83] and our ab-initio prediction for the volume change is given Fig. 3.3. Since Benarosch et al. always observed Mo or Mn alloyed cementites and no pure Fe₃C phases in their model steels, we used two different ways to estimate Fe₃C volume. First, we used Wood et al. data for Fe₃C volume to approximate ΔV (black dots Fig. 3.3). According to our DFT results, the volume change admits a linear behavior in the dilute regime upon Mo or Mn alloying. Therefore, we also used a linear regression on Benarosch et al. data to estimate the volume of pure cementite (red or blue dot Fig. 3.3). They observed that Mo and Mn alloying respectively induce an increase and a decrease of cementite volume upon alloying, in agreement with our predictions. The correlation between our results and Benarosch et al. data is not very good. However, please note that this comparison is based on several approximations (on the volume of Fe₃C but also from XRD analyses with very low volume fractions of cementite phases).

3.3.3 Binding enthalpies between Mo, Cr or Mn atoms in cementite

Before addressing Mo, Cr or Mn mixing in cementite, the interaction between two isolated solutes was investigated. The binding enthalpy between two M solutes in Fe_{3k-2}M₂C_k cementite is defined as follow:

$$H_b(Fe_{3k-2}M_2C_k) = 2H(Fe_{3k-1}M_1C_k) - H(Fe_{3k-2}M_2C_k) - H(Fe_{3k}C_k), \quad (3.1)$$

where $H(Fe_{3k-1}M_1C_k)$ is the total enthalpy of a single solute in its ground state, $H(Fe_{3k-2}M_2C_k)$ is the total enthalpy of two solutes in the cementite supercell and $H(Fe_{3k}C_k)$ is the total enthalpy of the supercell without solute. With this convention, positive binding enthalpy stand for attractive behaviors, while negative binding enthalpy stand for repulsion. Fig. 3.4 shows the binding enthalpies between two M (M=Mo, Cr or Mn) solutes in cementite as function of their separation distance. In the case of Mn and Cr solute pairs, all the magnetic configurations were taken into account for the initialization of the calculations of $E(Fe_{3k-2}M_2C_k)$. We investigated all the possible M-M pairs of the same chemical element for the first solute-solute neighbors, as well as a few pairs for larger distances. Figure 3.4 shows that there

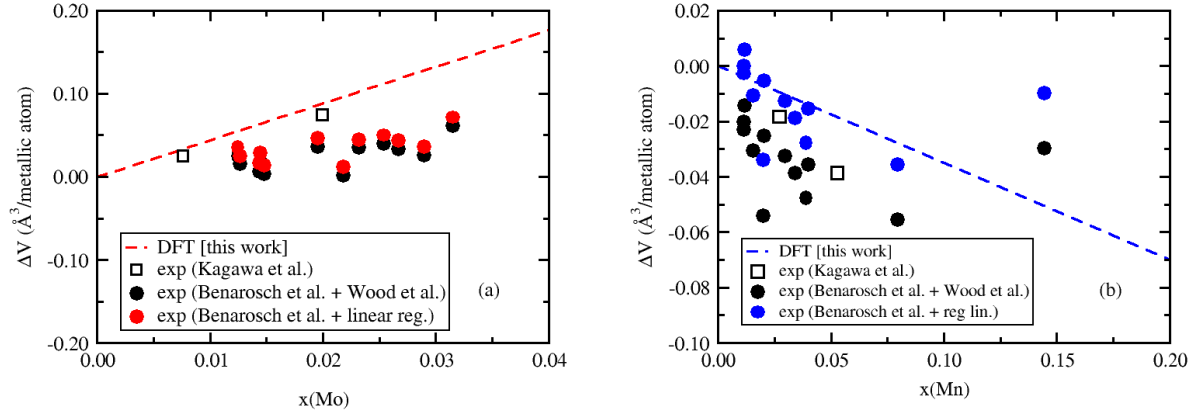


FIGURE 3.3:

(a) and (b): volume change $\Delta V = V(Fe_{1-x}M_xC) - V(Fe_3C)$ for $M=\text{Mo}$ or Mn alloyed cementite, respectively, according to the alloying element concentration.

The previous experimental data are from Ref. [83]. In order to calculate ΔV , the volume of pure Fe_3C was approximated by Wood *et al.* [213] experimental value at room temperature (black dots), and also estimated from a linear regression in the dilute regime (red and blue dots).

The linear regression on our DFT results in the dilute regime is represented by dashed lines.

are some slightly attractive Mo-Mo, Mn-Mn or Cr-Cr pairs for short distances. Mn solutes involved in a pair are always FM with respect to the Fe atoms of cementite, except for the lowest Mn-Mn distance, where both Mn solutes are AF with respect to the Fe atoms. For this shortest distance, it is possible that the Mn-Mn antiferromagnetic coupling with each other becomes the dominant magnetic interaction over the Mn-Mn ferromagnetic coupling tendency in the presence of C atoms. The Cr solutes involved in a Cr-Cr pair in cementite are AF with respect to the Fe atoms. The presence of attractive solute-solute pairs implies that solute clusters might appear in cementite.

3.3.4 Mixing enthalpy of Mo, Cr or Mn alloyed cementite

To investigate further the mixing tendencies of Mo, Cr or Mn in alloyed cementite, we calculated the mixing enthalpies of several $(Fe,M)_3C$ configurations. The mixing enthalpy of $(Fe,M)_3C$ with l solutes M is given by:

$$H_{mix}(Fe_{3k-l}M_lC_k) = \frac{H(Fe_{3k-l}M_lC_k) - (3k-l)H(Fe_3C) - lH(M_3C)}{3k}, \quad (3.2)$$

where $E(Fe_{n_{k-l}}M_lC_k)$ is the total enthalpy of the cementite with l M solutes, whereas $H(Fe_3C)$ and $H(M_3C)$ are the total enthalpies per metallic atom of pure Fe_3C and pure M_3C , respectively. We took ferromagnetic Fe_3C , ferrimagnetic Mn_3C , non-magnetic Mo_3C and non-magnetic Cr_3C as references for $M_{3k}C_k$. The mixing enthalpies of cementite with Mo, Cr or Mn are given in Fig. 3.5. Overall, $(Fe,Mo)_3C$ configurations admit a rather strong, positive mixing enthalpy, which reveals an unmixing tendency. A few ordered configurations have a slightly negative mixing enthalpy. These configurations correspond to cases where enough Mo solutes occupy exclusively special metallic sites. Such configurations admit low configurational entropies and therefore will probably not form, except at low temperature. For Cr

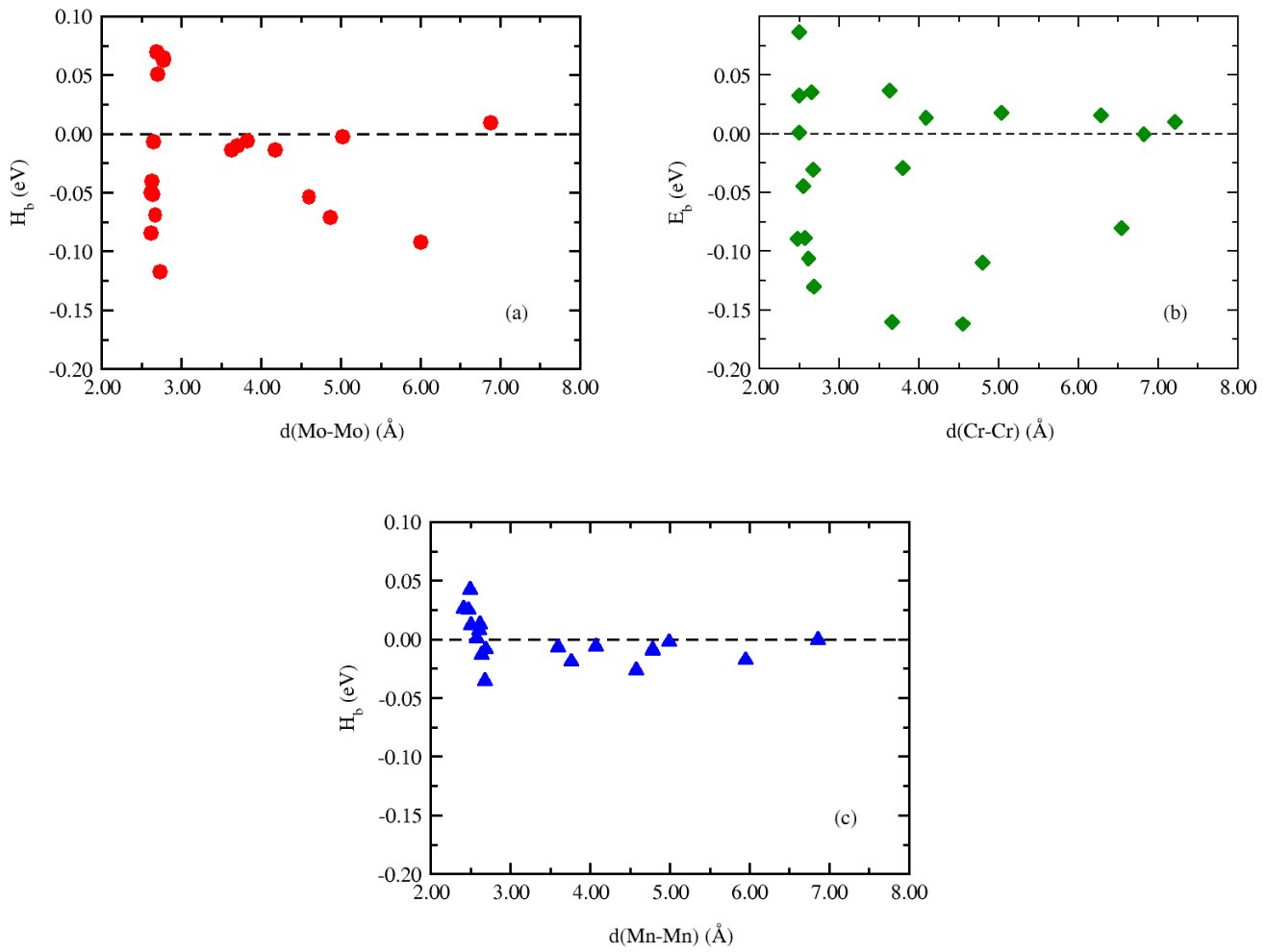


FIGURE 3.4: (a), (b), (c): Binding enthalpy between two Mo, Cr or Mn solutes, respectively according to the distance between solutes in ternary cementite.

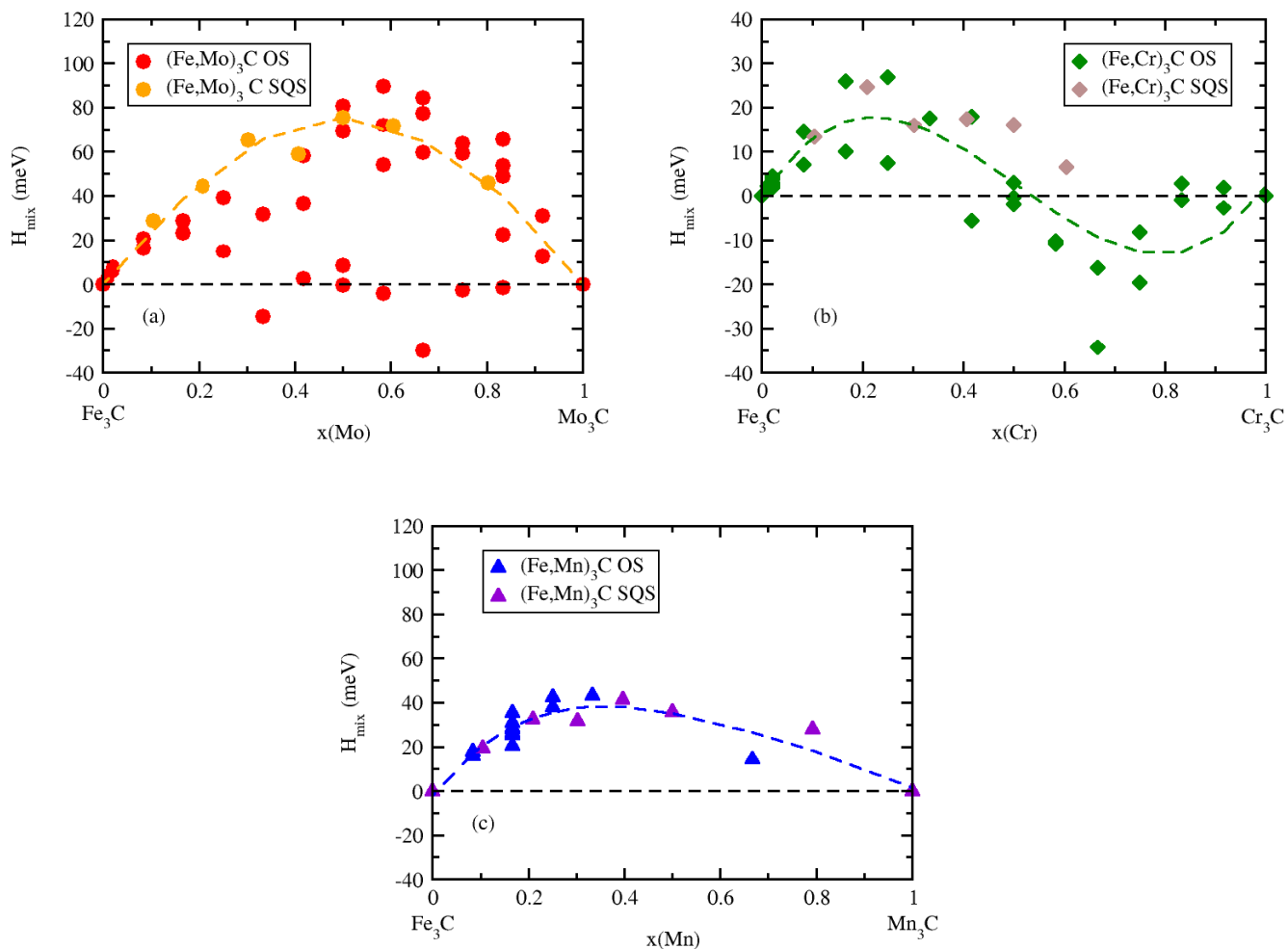


FIGURE 3.5: (a), (b), (c): Mixing enthalpy of $(\text{Fe}, M)_3\text{C}$ ($M = \text{Mo}, \text{Cr}$ or Mn) cementite as a function of the solute concentration (expressed as the fraction of metallic site occupied by the solutes). We differentiate $(\text{Fe}, M)_3\text{C}$ configurations with ordered structures or solute clusters (OS) from configurations with a completely random distribution of solutes (SQS configurations). Ferromagnetic Fe_3C , non-magnetic (NM) $M_3\text{C}$ ($M = \text{Mo}$ or Cr) and Von Appen antiferromagnetic (AF) Mn_3C magnetic configuration described previously are used as reference.

alloyed cementite, we observe a change from a rather weak unmixing tendency for Cr concentration below roughly 50% of metallic sites to a weak mixing tendency for higher Cr concentrations. This trend reversal is related to the Cr-Cr and Cr-C interactions beyond 50% of Cr occupancy in cementite. The calculated Mn alloyed configurations are all positive, implying an unmixing tendency for Mn in cementite. For the three solutes, the unmixing tendencies predicted for small concentrations are coherent with the presence of attractive solute-solute pairs in cementite. At the 1nn distance, the binding enthalpy (positive or negative) is highly configuration dependant for Mo and Cr solutes pairs, but much less for Mn pairs. This may support the emergence of low-energy ordered structures in Mo or Cr alloyed cementite and together with the existence of SQS structures with positive mixing enthalpies.

3.3.5 Enthalpy of substitution of Mo or Mn in Fe₃C

In previous ab-initio studies, the conclusions on the (de)stabilization of carbides by an alloying element are usually based on the enthalpy of formation of the alloyed carbide. Generally, the enthalpy of formation is calculated with respect to each atom ground state. For example, the enthalpy of formation of alloyed cementite Fe_{3k-i}M_iC_k is often given by:

$$H^f(Fe_{3k-i}M_iC_k) = H(Fe_{3k-i}M_iC_k) - (3k - i)H_{Fe}(bcc) - iH_M - kH_C, \quad (3.3)$$

where $H(Fe_{3k-i}M_iC_k)$ is the total enthalpy of cementite with i substitutional M solutes, $H_{Fe}(bcc)$ the total enthalpy per iron atom in ferromagnetic bcc iron, H_M the total enthalpy per atom of the alloying element M in its ground state and H_C the total enthalpy per C atom in graphite. In the case of pure Fe_{3k}C_k cementite, we calculated a formation energy of 0.204 eV/f.u.. Assuming that the system is in a metastable state where the graphite phase is not yet formed and there are just metastable carbides such as cementite, it is more relevant to use the total enthalpy of an isolated C interstitial in the matrix and the total enthalpy of an isolated solute in the matrix as the enthalpy references for H_C and H_M , respectively. This is the same as subtracting the enthalpy of formation of the k C interstitials in the matrix and the i M solutes in the matrix from Eq. 3.3. The revised enthalpy of formation is therefore written:

$$H^f(Fe_{3k-i}M_iC_k)_{\text{wrt matrix}} = H^f(Fe_{3k-i}M_iC_k) - iH^f(M \text{ in bcc Fe}) - kH^f(C_{\text{int}} \text{ in bcc Fe}), \quad (3.4)$$

where $H^f(Fe_{3k-i}M_iC_k)$ is the enthalpy of formation of alloyed cementite with respect to to each component ground state (defined Eq. 3.3). $H^f(M \text{ in bcc Fe})$ and $H^f(C_{\text{int}} \text{ in bcc Fe})$ are the enthalpy of formation of an isolated M solute and the enthalpy of formation of an isolated C octahedral interstitial in bcc iron with respect to M, Fe and C ground states. Hence:

$$H^f(M \text{ in bcc Fe}) = H(bcc Fe + M) - H(bcc Fe) - H_M, \quad (3.5)$$

$$H^f(C_{\text{int}} \text{ in bcc Fe}) = H(bcc Fe + C_{\text{int}}) - H(bcc Fe) - H_C, \quad (3.6)$$

where $H(bcc Fe)$ is the total enthalpy of a bcc Fe supercell, $H(bcc Fe + M)$ is the total enthalpy of the Fe bcc supercell with a M substitutional solute and $H(bcc Fe + C_{\text{int}})$ is the total enthalpy of the Fe bcc supercell with a C octahedral interstitial. Using Eq. 3.4 and Eq. 3.5, we obtained a formation energy of -0.55 eV/f.u.. Contrary to Fe₃C enthalpy of formation with respect to Fe and C ground states, this negative value entails that the formation of pure Fe₃C is energetically favorable in ferrite.

The presence of alloying elements in steels can (de)stabilize carbides. Stabilization of cementite by an alloying element implies that it is energetically favorable for this element to move from the bcc matrix into cementite, while destabilization implies that the alloying element remains in the matrix. The partitioning of alloying element between the matrix and cementite is quantified using the *enthalpy of substitution*. The *enthalpy of substitution* is the enthalpy required for M solutes to transfer from the matrix into cementite. In other words, it is the difference between the enthalpy of formation of alloyed cementite with respect to the matrix and the enthalpy of formation of pure Fe_3C cementite with respect to the matrix. The average enthalpy of substitution of i M atoms in $Fe_{3k-i}M_iC_k$ cementite is defined as:

$$H_{sub} = \frac{\Delta H_{\text{wrt matrix}}^f}{i} = \frac{H_{\text{wrt matrix}}^f(Fe_{3k-i}M_iC_k) - H_{\text{wrt matrix}}^f(Fe_{3k}C_k)}{i}. \quad (3.7)$$

A negative H_{sub} implies that the alloying element stabilizes (partition into) cementite while a positive H_{sub} implies that the alloying element destabilizes cementite and tends to remain in the matrix. If we develop this expression, we obtain:

$$H_{sub} = \frac{H(Fe_{3k-i}M_iC_k) + iH(bcc Fe) - H(Fe_{3k}C_k) - iH(bcc Fe + M)}{i}. \quad (3.8)$$

Thus, the enthalpy of substitution can be seen as a binding enthalpy. In this section, we focus on Mo or Mn substitution in cementite because those are the alloying elements present in Benarosch *et al.* model steels samples [74]. We calculated the enthalpy of substitution of Mo or Mn alloyed cementite. The results are presented Fig. 3.6. The average *enthalpy of substitution* of $(Fe,Mo)_3C$ are mostly positive. It means that the substitution of Mo in cementite is overall unfavorable. A few Mo alloyed cementite configurations have a slightly negative H_{sub} . These configurations correspond to ordered configurations where enough Mo solutes occupy exclusively special metallic sites. Such configurations admit low configurational entropies and therefore will probably not form except at low temperature. All $(Fe,Mn)_3C$ configurations exhibit a negative enthalpy of substitution. Mn substitution in cementite is thereby favorable. According to Benarosch *et al.* SEM-EDS results, the Mo content in cementite can reach a few percent in a Fe-Mo-C model system, while the Mn content can reach up to 14% in a Fe-Mn-C model system. Our calculated enthalpies of substitution are therefore in good agreement with their experimental data.

We can see from the definition of the enthalpy of substitution Eq. 3.7 that if the Mn enthalpy of substitution is negative, it also implies that the formation enthalpy of cementite can be lowered thanks to the Mn alloying, which means that cementite is energetically stabilized by the Mn, while it is the contrary for Mo alloying.

3.4 Structural, magnetic and energetic properties of Fe or Mn alloyed M_2C

3.4.1 Stoichiometric Mo_2C

In low-alloyed steels, several M_2C carbides can precipitate (η - Fe_2C , ϵ - Fe_2C , Mo_2C ,...). Especially, in the presence of Mo, a M_2C phase enriched in molybdenum can appear. These M_2C carbides admit a very high Mo concentration and are therefore often called Mo_2C . Mo_2C carbides are also present in the Mo-C phase diagram [11]. Consequently, we considered that the Mo_2C is the basis of the M_2C carbide in Mo-alloyed

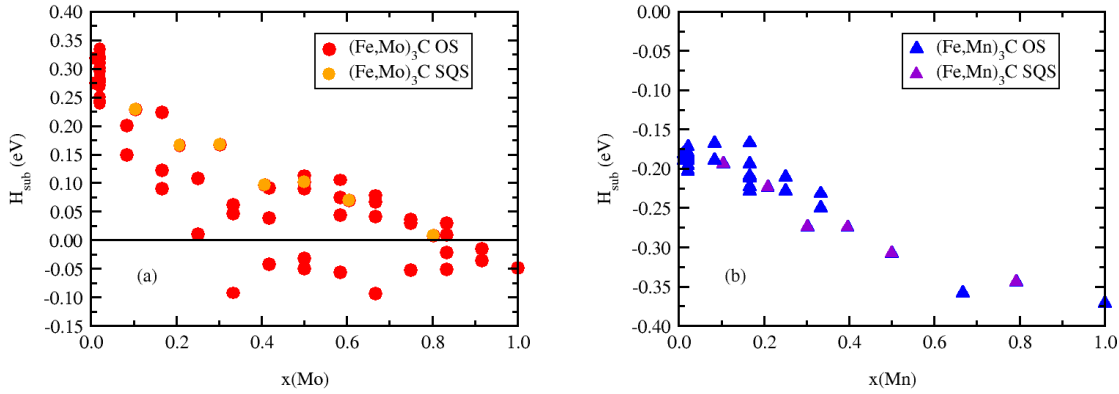


FIGURE 3.6: (a), (b): Average enthalpy of substitution of Mo and Mn in cementite (respectively) according to the Mo or Mn concentration. We differentiate $(\text{Fe,M})_3\text{C}$ ($M = \text{Mo}$ or Mn) configurations with ordered structures or solute clusters (OS) from configurations with a completely random distribution of solutes (SQS configurations).

Method [ref]	Lattice parameters (a,b,c) (\AA)
DFT:	
VASP, PAW, GGA [this work]	4.740 ; 6.063 ; 5.230
VASP, PAW, GGA [208]	4,751 ; 6,065 ; 5,237
VASP, PAW, GGA [148]	5.273 ; 6.029 ; 4.725
VASP, PAW, GGA [161]	4,793 ; 6,030 ; 5,211
VASP, USPP, GGA [1]	4.793 ; 6.030 ; 5.211
CASTEP, USSP, GGA [110]	4.738 ; 6.038 ; 5.210
CASTEP, USPP, GGA [209]	4.707 ; 6.040 ; 5.247
CASTEP, USPP, GGA [112]	4,79 ; 6,01 ; 5,21
CASTEP, USPP, GGA [156]	4.748 ; 6.026 ; 5.204
QE, NCPP, GGA [84]	4.75 ; 6.09 ; 5.26
\varnothing^a , Troullier–Martins, LDA [59]	4.735 ; 6.125 ; 5.260
DACAPO, USPP, GGA [204]	4.825 ; 6.162 ; 5.304
RSPt, FP-LMTO, LDA [71]	4.711 ; 5.988 ; 5.185
GPAW, \varnothing^b , RPBE [120]	4,839 ; 6,173 ; 5,322
QE, USPP, PW91 [135]	4,798 ; 6,127 ; 5,314
Exp:	
Neutron diffraction [143]	4.72 ; 6.00 ; 5.19
Neutron diffraction [31]	4,732 ; 6,037 ; 5,204
Neutron diffraction [41]	4,735 ; 6,025 ; 5,210
X-ray diffraction [139]	4,729 ; 6,028 ; 4,850
Rietveld refinements on XRD profiles [155]	5,213 ; 6,020 ; 4,748

^aUnspecified

^bLocalized basis functions

TABLE 3.2: Lattice parameters of orthorhombic Mo_2C carbide according to theoretical and experimental studies.

ferrite, and that its composition can slightly vary upon alloying. Molybdenum carbide Mo_2C can crystallise as at least three polymorph phases. At high temperatures (above 1960 °C), Mo_2C displays a disordered hexagonal crystal structure, in which the Mo atoms form a hexagonal close packed sublattice and the C atoms randomly occupy half the octahedral interstitial sites [59]. Upon cooling, the hexagonal Mo_2C transitions to more ordered crystal structures. An ϵ - Fe_2N -type Mo_2C structure was experimentally observed [41] for intermediate temperatures (between 1960 and 1350 °C). Below this temperature range, Mo_2C adopts an ζ - Fe_2N -type, orthorhombic crystal structure. The orthorhombic Mo_2C is stable at ambient temperature and pressure [41].

In this work, we chose to focus on the orthorhombic Mo_2C for several reasons:

- (i) This crystal structure was found to be energetically more favorable by all ab-initio studies comparing the relative stability of hexagonal, orthogonally and sometimes trigonal (ϵ - Fe_2N -type) intermediate phases of Mo_2C [1, 59, 71, 110, 112, 161].
- (ii) Considering the annealing temperature of 16MND5 and Benarosch *et al.* model steels, we expect the precipitation of orthorhombic Mo_2C .
- (iii) The distribution of the C atoms in the Mo_2C disordered hexagonal phase is controversial. At the moment, X-ray diffraction analyses and DFT studies from Haines *et al.* [59] and Shi *et al.* [173] have shown that an eclipsed configuration with a Mo–C–Mo–C stacking where half of the C atoms in the second layer and half of the C atoms in the fourth layer are removed is the most likely candidate for the hexagonal Mo_2C .

A schematic view of orthorhombic Mo_2C is given Fig. 3.7. Orthorhombic Mo_2C crystallises in the $Pbcn$ space group (S.G. No. 60) with four formula units per unit cell. In orthorhombic Mo_2C , Mo atoms form a slightly distorted hexagonal-closed packed (hcp) sublattice and the C atoms occupy half the octahedral interstitial sites. Each Mo atom has three almost planar C neighbors while each C atom has six Mo neighbors. Our calculated lattice parameters are in good agreement with previous

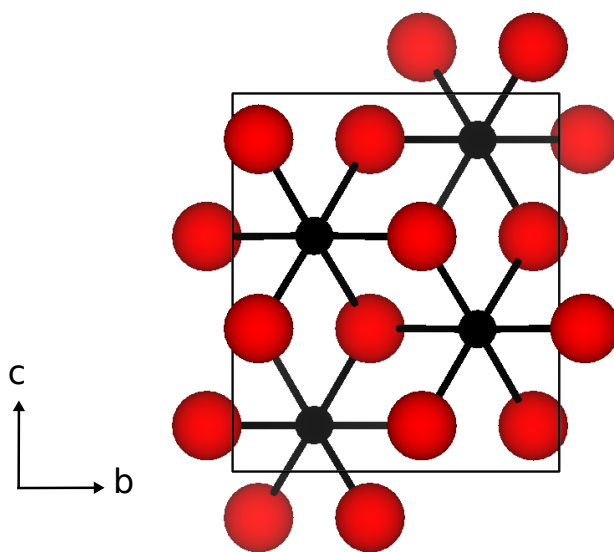


FIGURE 3.7: Crystal structure of Mo_2C . Mo atoms are in red and C atoms are in black.

first-principles and experimental studies (see Table. 3.2). Since we only consider the Mo₂C orthorhombic structure, we will refer to it as Mo₂C from now on.

3.4.2 Magnetism of Fe or Mn alloyed Mo₂C

Mo₂C is non-magnetic. However, this carbide cannot maintain its non-magnetic state upon alloying with magnetic elements such as Fe or Mn. The amplitude of the magnetic moment of one Fe or Mn solute in $2 \times 2 \times 2$ Mo₂C supercell ($x(\text{Fe or Mn}) \approx 1.5\%$) is $2.06 \mu_B$ and $2.35 \mu_B$, respectively. Fig. 3.8 shows the average magnetic moment of (Mo,M)₂C according to the solute M (M=Fe or Mn) concentration. As for cementite, beyond a few solutes in (Mo,M)₂C, an exhaustive study of all magnetic configurations is very CPU expansive. Therefore, we initialized (Mo,Fe)_{2k}C_k and (Mo,Mn)_{2k}C_k calculations with Fe or Mn atoms ferromagnetically coupled with each other and assumed that the results do not deviate too much from the magnetic ground states. Overall, the Fe atoms preserve their initial FM ordering upon relaxation. A few configurations with approximately 40% to 50% of Fe solutes on the metallic sites did not keep a complete FM coupling between Fe (a few Fe atoms adopted an slightly AF or almost-zero magnetic moment). This may be due to a technical issue during self-consistency and atom-relaxation. In any case, such Fe concentrations are less relevant since only a low percent of Fe is found experimentally in the Mo₂C phase. Fe₂C stays completely ferromagnetic, with a $1.74 \mu_B$ magnetic moment per Fe atom. The presence of a C interstitial decreases the magnetic moment magnitude of neighboring Fe atoms. In the case of Mn alloying, Mn solutes stay ferromagnetically coupled and Mn₂C is FM with an $1.92 \mu_B$ magnetic moment per Mn atom.

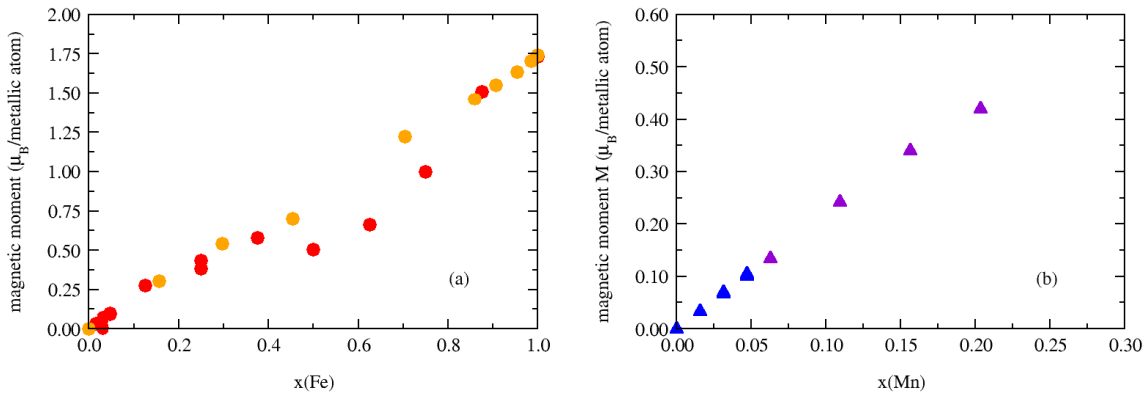


FIGURE 3.8: (a) and (b) Average magnetic moment of metallic atoms in alloyed (Mo,M)₂C according to the alloying element M= Fe or Mn concentration, respectively. We differentiate (Mo,M)₂C configurations with ordered structures or solute clusters (OS) from configurations with a completely random distribution of solutes (SQS configurations).

3.4.3 Volume change in Fe or Mn alloyed Mo₂C

The volume of Mo₂C carbide is $18.781 \text{ \AA}^3/\text{metallic atom}$. Previous ab-initio studies reported values included between $18.283 \text{ \AA}^3/\text{metallic atom}$ and $19.872 \text{ \AA}^3/\text{metallic atom}$ [1, 59, 71, 84, 110, 112, 120, 135, 148, 156, 161, 204, 208, 209], while experimental data for Mo₂C volume are between $18.373 \text{ \AA}^3/\text{metallic atom}$ and $18.625 \text{ \AA}^3/\text{atom}$

[31, 41, 139, 143], with the exception of a $17.282 \text{ \AA}^3/\text{atom}$ value reported by Reddy *et al.* [155]. Our calculated volume is therefore slightly higher than experimental data. This small volume difference might be attributed to an external stress induced by the Mo_2C carbide environment in the experimental samples. It may also be due to the inaccuracy of our DFT approximations, exchange-correlation functional or PAW potential. Please note that as previously with cementite, when only the lattice parameters are given in the literature, we multiplied them to approximate the volume of the orthorhombic cell. The evolution of $(\text{Mo,Fe})_2\text{C}$ and $(\text{Mo,Mn})_2\text{C}$ volumes according to their concentration in alloying elements is given Fig. 3.9. In both cases, the volume of Fe or Mn alloyed M_2C carbide decreases linearly, following a Vegard's law. At a given solute concentration $(\text{Mo,Mn})_2\text{C}$ volume per metallic atom is slightly higher than $(\text{Mo,Fe})_2\text{C}$. This is coherent with the slightly higher magnetic moments calculated in the case of Mn alloying. Lastly, for a given Mo concentration, $(\text{Fe,Mo})_2\text{C}$ volume per metallic atom is always higher than $(\text{Fe,Mo})_3\text{C}$. Logically, large Mo atoms prefer to form Mo_2C rather than Mo_3C where they would have less room. On the other hand, Mn and Fe atoms have similar sizes, and their partitioning behavior between cementite and M_2C carbides is most likely governed by more complex effects, such as magnetism or electronic charge redistribution.

To our knowledge, there is no previous data on alloyed Mo_2C volume in the literature. Recently, Benarosch *et al.* obtained the volume of Fe and Mn alloyed $(\text{Mo,M})_2\text{C}$ carbides in Fe-Mo-C and Fe-Mo-Mn-C steels through a combination of X-ray diffraction, SEM-EDS and Rietveld refinements. However, because of the very small volume phase, they concluded that the precision of their measures is not sufficient enough to exploit the results.

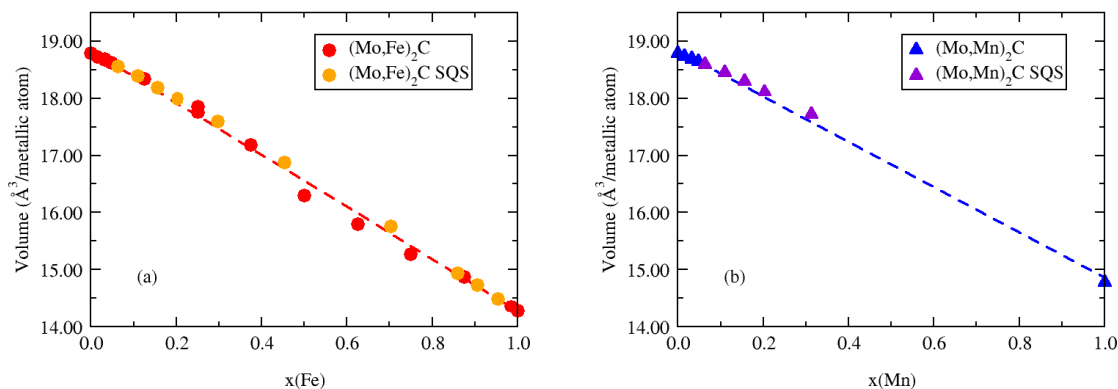


FIGURE 3.9: (a), (b): Volume of alloyed $(\text{Mo,M})_2\text{C}$ carbide according to its alloying element M ($M=\text{Fe}$ or Mn , respectively) concentration (expressed as the fraction of metallic sites occupied by M).

3.4.4 Binding enthalpy between Fe or Mn solutes in Mo_2C

Similarly to the binding enthalpy between two solutes in cementite, the binding enthalpy between two M solutes in $\text{Mo}_{2k-2}\text{M}_2\text{C}_k$ is given by:

$$H_b(\text{Mo}_{2k-2}\text{M}_2\text{C}_k) = 2H(\text{Mo}_{2k-1}\text{M}_1\text{C}_k) - H(\text{Mo}_{2k-2}\text{M}_2\text{C}_k) - H(\text{Mo}_{2k}\text{C}_k), \quad (3.9)$$

where $H(Mo_{2k-1}M_1C_k)$ is the total enthalpy of a single solute M in Mo_2C in its ground state, $H(Mo_{2k-2}M_2C_k)$ is the total enthalpy of two M atoms in Mo_2C and $H(Mo_{2k}C_k)$ is the total enthalpy of Mo_2C without solute. Positive binding enthalpies are associated with attractive behaviors, while negative binding enthalpies are associated with repulsion. As mentioned previously, the magnetic behavior of Mn is very sensitive to its local environment. For this reason, all the possible magnetic configurations of Mn-Mn pairs were taken into account. We calculated the binding enthalpies of all the first solute-solute neighbors, as well as a few pairs for larger distances. The results are presented Fig. 3.10. All the Fe-Fe or Mn-Mn binding enthalpies calculated are positive (denoting an attractive behavior) or almost zero. We obtained some very attractive binding enthalpies for Fe-Fe (up to 0.20 eV) or Mn-Mn (up to 0.12 eV) pairs in Mo_2C . The 0.20 eV and 0.12 eV binding enthalpies calculated for a Fe-Fe and Mn-Mn pair correspond to the same configuration. In this most attractive configuration, the two solutes do not share any 1nn C, and the almost perfect planes containing a solute and its 3 carbon neighbors are parallel to each other. Fe solutes involved in a pair are always FM with respect to each other. For short distances, two Mn solutes are FM with respect to each other in Mo_2C . Beyond 4 Å, Mn solutes hardly interact anymore: their binding enthalpies are almost zero and they can be either FM or AF with respect to each other. Since Fe and Mn solute pairs admit some high binding enthalpies, we also investigated the case of three solutes clusters. In particular, we focused on three Fe or Mn clusters involving very attractive solute pairs. The total binding enthalpy of three solutes M in $Mo_{2k-3}M_3C_k$ is similar the the binding enthalpy of two solutes in $Mo_{2k-2}M_2C_k$. It is defined as:

$$H_b(Mo_{2k-3}M_3C_k) = 3H(Mo_{2k-1}M_1C_k) - H(Mo_{2k-3}M_3C_k) - 2H(Mo_{2k}C_k), \quad (3.10)$$

with $H(Mo_{2k-3}M_3C_k)$ the total enthalpy of the three solutes cluster. The maximum binding enthalpies calculated are 0.35 eV for three Fe solutes clusters and 0.24 eV for three Mn solutes clusters. These results implies that Fe or Mn solute clusters may appear in M_2C carbide.

3.4.5 Mixing enthalpy of Fe or Mn alloyed M_2C

By analogy with Eq. 3.2, the mixing enthalpy of $(Mo,M)_2C$ with l solutes M is written:

$$H_{mix}(Mo_{2k-l}M_lC_k) = \frac{H(Mo_{2k-l}M_lC_k) - (2k-l)H(Mo_2C) - lH(M_2C)}{2k}, \quad (3.11)$$

with $H(Mo_{2k-l}M_lC_k)$ the total enthalpy of l solutes M in $(Mo,M)_2C$, $H(Mo_2C)$ the total enthalpy per metallic atom of pure Mo_2C and $H(M_2C)$ the total enthalpy per metallic atom of pure M_2C . We used non-magnetic Mo_2C , ferromagnetic Fe_2 and ferromagnetic Mn_2C as references for $M_{2k}C_k$. The results are presented Fig. 3.11. We found some positive mixing enthalpies for Fe or Mn alloyed Mo_2C , which indicates an unmixing tendency. This unmixing tendency is coherent with the high binding enthalpies calculated between two or three Fe or Mn solutes in Mo_2C . The mixing enthalpies of Fe alloyed M_2C are higher than the mixing enthalpies of Mn alloyed M_2C , which is consistent with a larger 1nn Fe - Fe attraction.

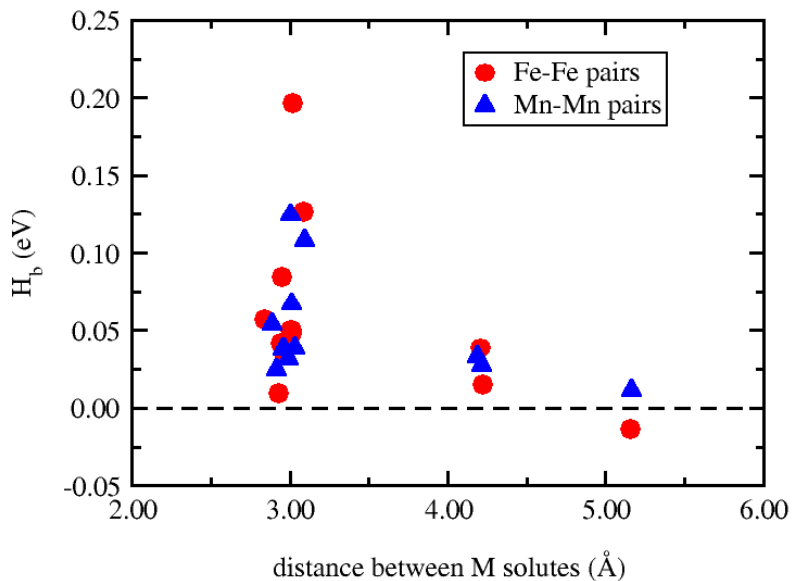


FIGURE 3.10: Binding enthalpy between two M ($M=\text{Fe}$ or Mn) atoms in a $2 \times 2 \times 2$ Mo_2C supercell, as function of the M - M separation distance. Positive binding enthalpy means attraction, negative binding enthalpy means repulsion.

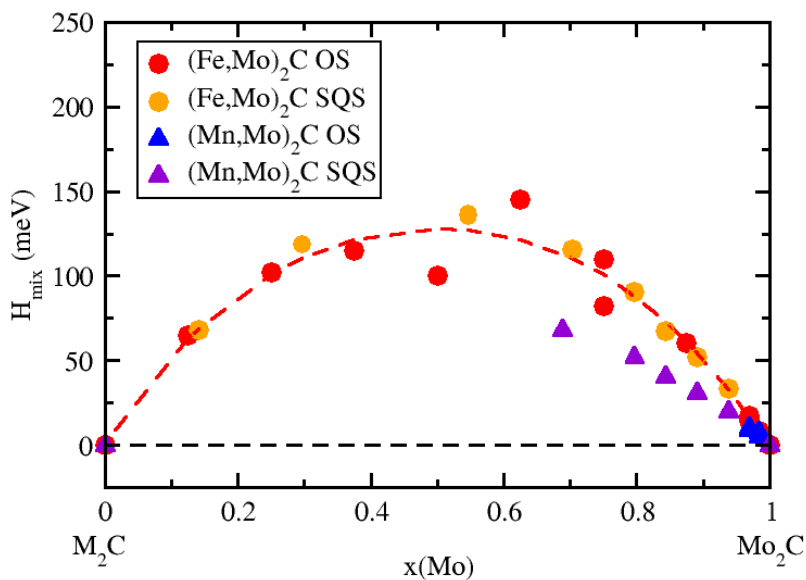


FIGURE 3.11: Mixing enthalpy of $M=\text{Fe}$ or Mn alloyed $(\text{Mo},M)_2\text{C}$ as function of the Mo concentration (expressed as the fraction of metallic sites occupied by Mo). We differentiate $(\text{Mo},M)_2\text{C}$ configurations with ordered structures or solute clusters (OS) from configurations with a completely random distribution of solutes (SQS configurations). Ferromagnetic Fe_2C and Mn_2C , as well as non-magnetic Mo_2C are used as reference.

3.4.6 Enthalpy of substitution of Fe or Mn in Mo_2C

The average enthalpy of substitution of l M (M=Fe or Mn) solutes in Mo_2C carbide is given by:

$$H_{sub}(Mo_{2k-l}M_lC_k) = \frac{H_{wrt\ matrix}^f(Mo_{2k-l}M_lC_k) - H_{wrt\ matrix}^f(Mo_{2k}C_k)}{l} \\ = \frac{H(Mo_{2k-l}M_lC_k) + lH(bcc\ Fe + Mo) - H(Mo_{2k}C_k) - lH(bcc\ Fe + M)}{l}, \quad (3.12)$$

where $H_{wrt\ matrix}^f(Mo_{2k-l}M_lC_k)$ and $H_{wrt\ matrix}^f(Mo_{2k}C_k)$ are the enthalpies of formation of $Mo_{2k-l}M_lC_k$ and $Mo_{2k}C_k$ with respect to the matrix, respectively. The results are presented Fig. 3.12. With the exception of Mn_2C , all the Fe or Mn alloyed configurations have a positive average enthalpy of substitution. This implies that Fe or Mn substitution in Mo_2C is energetically unfavorable. Or, to put it the other way, it is energetically favorable for a Fe or Mn solute in M_2C to move into the matrix and for a Mo atom of the matrix to replace it. In Fe-Mo-C model steels, Benarosch *et al.* reported up to 7% of Fe in Mo_2C . In Fe-Mo-Mn-C model steels, they observed approximately 4% of Fe and 2% of Mn in Mo_2C . However, the Mn content predicted by CALPHAD is significantly higher (18%) than the concentration experimentally observed. According to our results, the enthalpy of substitution of Mn alloyed cementite is significantly lower than the enthalpy of substitution of Fe alloyed cementite. Mn alloying would therefore be less unfavorable than Fe alloying in Mo_2C , in agreement with CALPHAD predictions.

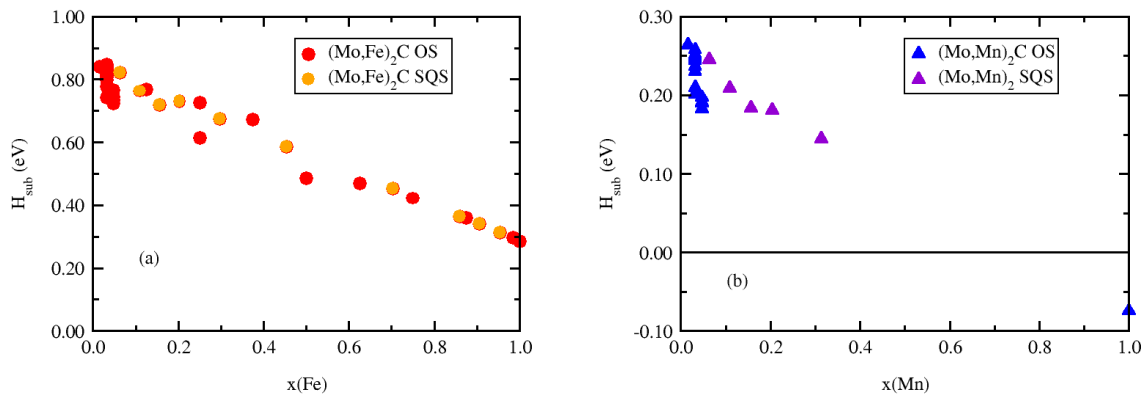


FIGURE 3.12: Average enthalpy of substitution of Fe or Mn in Mo_2C , respectively, according to the Fe or Mn concentration. We differentiate $(Mo,M)_2C$ (M= Fe or Mn) configurations with ordered structures or solute clusters (OS) from configurations with a completely random distribution of solutes (SQS configurations).

3.5 Partitioning of Fe, Mo and Mn between M_3C and M_2C

In the previous section, we discussed the partitioning behavior of an alloying element between cementite or Mo_2C carbides and ferrite. However, we can also estimate the partition of an alloying elements between different carbides in ferrite. For example, Mn average enthalpy of substitution in cementite is always negative, while

Mn average enthalpy of substitution in Mo_2C is mostly positive. Mn would therefore preferably substitute in cementite rather than in Mo_2C , in good agreement with Benarosch *et al.* experimental data. In particular, in Fe-Mn-Mo-C steels, they measured up to 2% of Mn in $(Mo,Mn)_2C$ and up to 8% of Mn in cementite.

In this chapter, we mainly used Thermo-Calc (CALPHAD) data to predict the equilibrium concentration of M_3C and M_2C in alloying elements. However, this very useful tool can also predict the enthalpy or free energy of a given system. For instance, we used CALPHAD data to determine the mixing energy of bcc Fe-Mn alloys (see Figure 3.13). Overall, our first results are in good agreement with theoretical results from Schneider *et al.* [164]. Additional CALPHAD calculations are underway in order to compare, for example our mixing enthalpies for Mo and Mn alloyed M_3C and our mixing enthalpies for Fe and Mn alloyed M_2C in Fe-Mn-C or Fe-Mo-C systems.

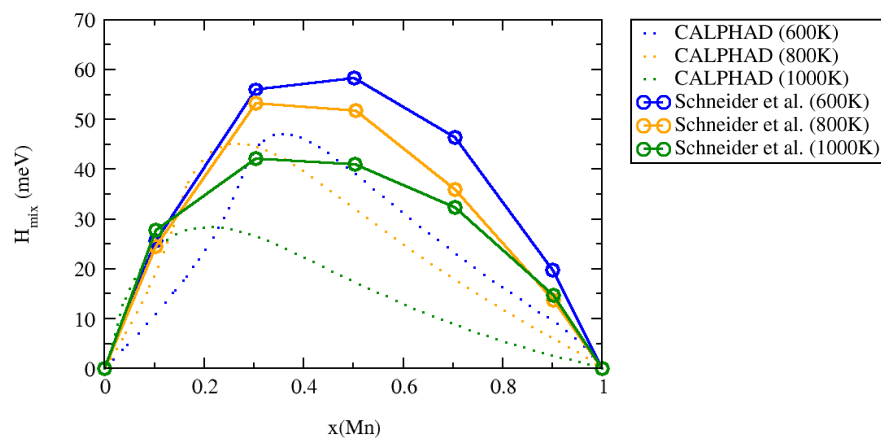


FIGURE 3.13: Comparison between the enthalpy of mixing of Mn alloyed bcc Fe predicted by CALPHAD with theoretical results from Schneider *et al.* [164], for several temperatures.

3.6 Magnetic disorder and vibrational entropy at finite temperatures

The Curie temperature of Fe_3C cementite is low (≈ 473 K) compared to the Curie temperature of bcc Fe (1043 K). However, Benarosch *et al.* tempered their model steels at 923 K and 973 K. As mentioned in the previous chapter, an atomistic study of cementite (and thus alloyed cementite) properties across the magnetic transition is beyond the scope of our study. Nevertheless, we estimated the impact of the paramagnetism in cementite on the enthalpies of substitution of several $(Fe,Mn)_3C$ and $(Fe,Mo)_3C$ configurations. Since Benarosch *et al.* observed up to 14% of Mn in cementite and up to 3% of Mo in cementite, we focused on the dilute configurations (a single solute in the supercell and SQS configurations with a low concentration of solute in the case of Mn alloying). To this end, we performed additional calculations using the previously relaxed magnetically ordered cementite configurations, but with a random distribution of Fe and Mn magnetic moments. Then, we replaced the total enthalpies of the first and third terms of Eq. 3.8 by the total enthalpies of the same cell, but with the Fe (and Mn) atoms in a magnetically random structure. Since Benarosch *et al.* tempering were performed below the Curie temperature of

iron, we kept the the total enthalpies of the bcc Fe matrix with or without solute in its ferromagnetic bcc state. The results are represented in black Fig. 3.14. The calculated enthalpies of substitution of $(\text{Fe,Mn})_3\text{C}$ are lower in the paramagnetic case. This entails that the magnetic disorder further promotes the substitution of Mn in cementite. In the case of Mo alloying, the enthalpies of substitution of alloyed cementite stay positive but are significantly reduced. Mo substitution in cementite is therefore less unfavorable in the paramagnetic case. In other words, the relative behavior of different solutes remains the same, while there is an overall decrease of the substitutional enthalpies.

We also investigated the effect of the vibrational entropy on the free enthalpies of substitution at finite temperature. To that end, we performed phonon calculations via DFT. Such calculations are very CPU expensive because of the low symmetry of the carbides. Consequently, we focused on a very dilute case, at 923 K and 973 K (typical temperatures of tempering). The results are given Fig. 3.15. At finite temperatures, the free enthalpy of substitution of Mo or Mn in cementite increases with the effect of the vibrational entropy. Especially, the free enthalpy of substitution of Mn in cementite is slightly positive at 923 and 973 K. In practice, this effect is compensated by the effect of magnetic disorder. On the other hand, for a Mo solute in cementite at finite temperature, the effect of the magnetic disorder is predominant and the free enthalpy of substitution becomes slightly lower. The free enthalpy of substitution of Mn in Mo_2C also increases with the temperature. On the other hand, the free enthalpy of substitution of Fe in Mo_2C become slightly lower with the effect of the vibrational entropy.

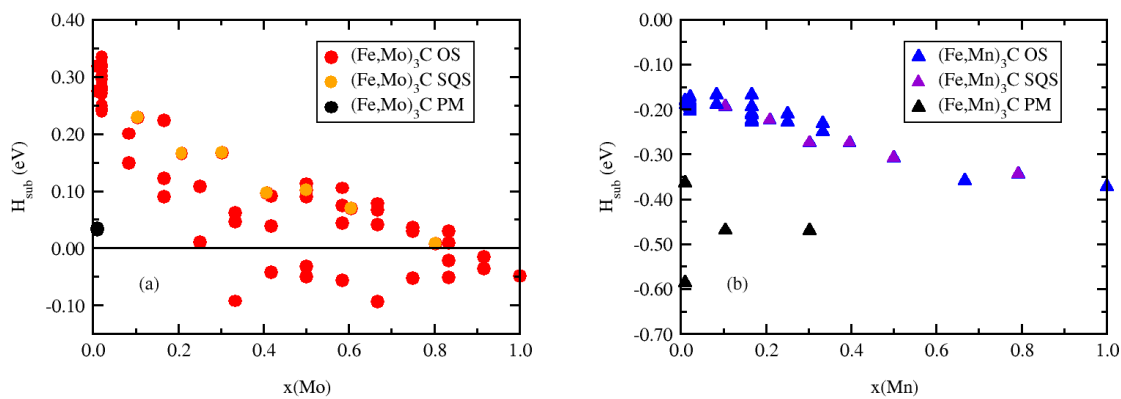


FIGURE 3.14: Average enthalpy of substitution of Mo (a) or Mn (b) in Fe_3C , respectively, according to the Mo or Mn concentration. We differentiate $(\text{Fe,M})_3\text{C}$ ($M = \text{Mo}$ or Mn) configurations with ordered structures or solute clusters (OS) from configurations with a completely random distribution of solutes (SQS configurations). The paramagnetic configurations (PM) are represented in black.

3.7 Summary

We studied several properties of M_3C carbides upon Mo, Mn or Cr alloying, as well as properties of M_2C upon Fe or Mn alloying. DFT calculations were performed for a wide range of alloying concentrations to predict the magnetization and volume change induced by substitutional solutes in these two carbides. The decrease

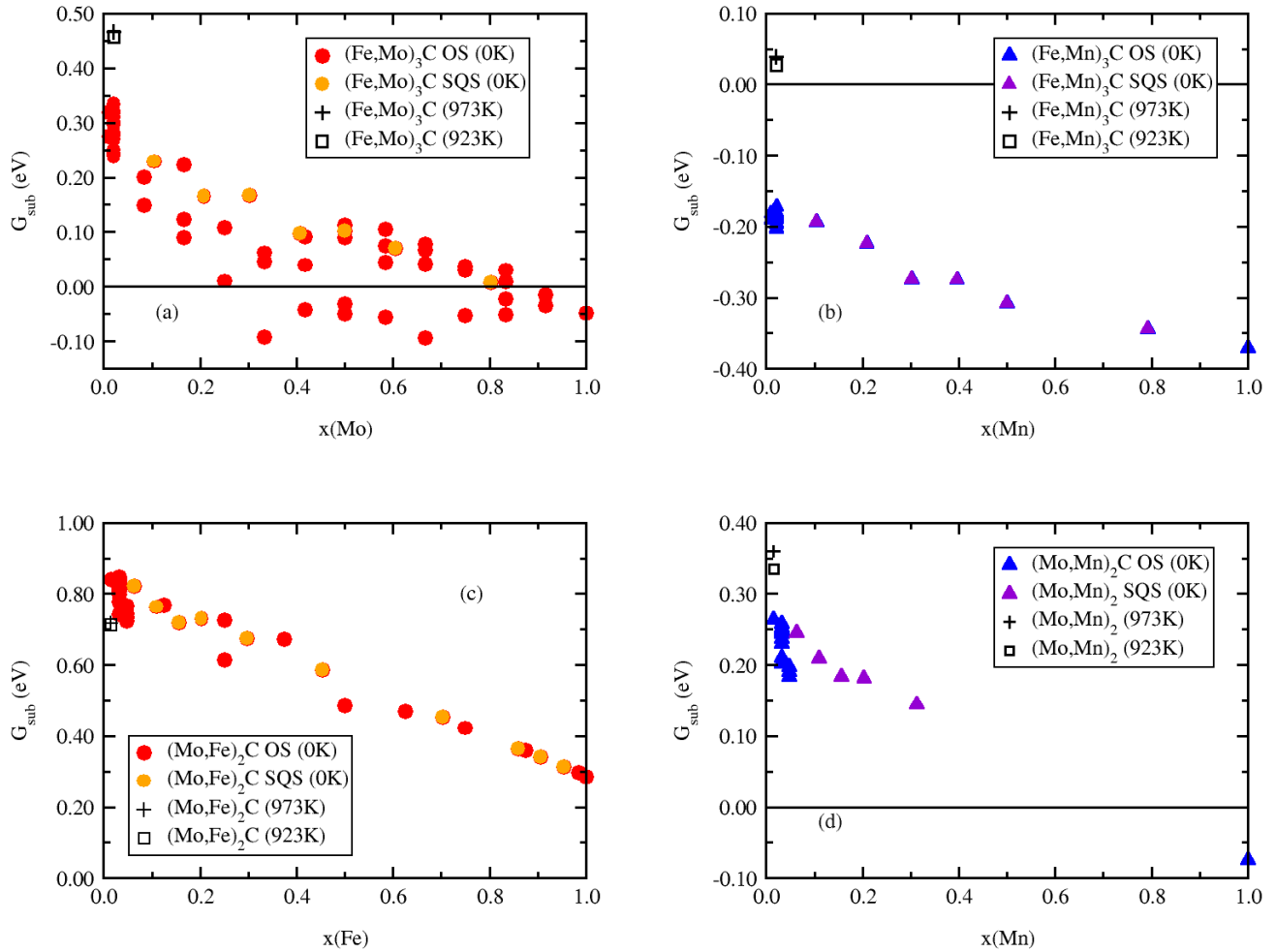


FIGURE 3.15: Average free enthalpy of substitution of Mo (a) or Mn (b) in Fe_3C and Fe (c) and Mn (d) in Mo_2C , respectively, according to the solute concentration. We differentiate configurations with ordered structures or solute clusters (OS) from configurations with a completely random distribution of solutes (SQS configurations). The free enthalpies of substitution calculated at 923 and 973 K are the back squares and the black plus, respectively.

of cementite Curie temperature observed experimentally upon alloying can be associated with the diminution of its average magnetic moment. The volume change caused by Mo substitution in Fe_3C is governed by size effects and follows a Vegard law. On the other hand, the volume change in Mn or Cr alloyed cementite is associated with complex magnetic behaviors. Nonetheless, $(\text{Fe,Mn})_3\text{C}$ and $(\text{Fe,Cr})_3\text{C}$ roughly decrease their volume and magnetization linearly in the dilute regime. Our DFT results are in relatively good agreement with previous experimental data, as well as recent data from Benarosch *et al.*. M_2C volume change upon Fe or Mn alloying also seems to follow a Vegard law. Unfortunately, to this date, there are no experimental data to compare our results with.

The mixing behavior of Mo, Cr or Mn in cementite and Fe and Mn mixing behavior in M_2C were studied. Overall, Mo and Mn display an unmixing tendency in cementite, and Fe and Mn display an unmixing tendency in M_2C . On the other hand, Cr solutes admit an unmixing tendency below 50% of site occupancy, and exhibit a mixing tendency for larger concentrations.

In addition, we used the enthalpy of substitution to predict the partitioning of Mo and Mn in between M_3C and ferrite and the partitioning of Fe and Mn between M_2C and ferrite. In particular, we found that Mn prefers to join the cementite, while it is energetically unfavorable for Fe or Mn to substitute in Mo_2C . This results are overall in agreement with experimental data. We predict that the concentration in Mn is higher than the concentration in Fe in M_2C , in agreement with CALPHAD data but contrary to experimental observations. Finally, the effect of the magnetic disorder and the vibrational entropy are discussed. If we take into account the paramagnetism of cementite, the relative behavior of Mo or Mn remains the same, while there is an overall decrease of the substitutional enthalpies. On the contrary, the effect of the vibrational entropy at finite temperature overall increases the free enthalpy of substitution, except for Fe alloying in Mo_2C .

Chapter 4

Modelling approach for the nucleation of cementite

In this chapter, we implemented a modelling approach in order to investigate the nucleation of cementite in ferrite. We identified an ordered Fe-C structure, with similar atomic organization and the same stoichiometry as cementite, but with Fe atoms residing on bcc-lattice sites (namely α -cementite). Employing this α -cementite as a representation of the cementite carbide, we parameterized effective-interaction and diffusion models using DFT data in order to perform equilibrium and kinetic on-lattice Monte Carlo simulations for the study of cementite precipitation in the α -Fe lattice.

4.1 State of the art

Cementite is a very common carbide, often found in iron alloys and in particular ferritic steels such as 16MND5. Cementite is hard and brittle and can improve the wear resistance. However, it also promotes the emergence of cracks [174]. Therefore, the inhibition of cementite precipitation leads to the improvement of steels toughness. In order to control the presence of cementite in iron-based materials, we must understand the mechanism(s) behind its nucleation. Despite the impact of cementite on steels properties, the study of its nucleation remains challenging. The nucleation and growth of ferrite and cementite has been investigated in Fe-C amorphous films using X-ray diffraction, transmission electron microscopy (TEM) and atom probe tomography [45]. However it is extremely challenging to observe experimentally the nucleation mechanism, as it occurs at the atomic scale. In addition, the precipitation of Fe₃C is frequently an heterogeneous process taking place at grain boundaries. The presence of point defects such as vacancies and/or impurities may also modify the nucleation.

At the atomic scale, numerical methods based on statistical physics can be used to describe precipitation. For instance, Gendt *et al.* and Hin *et al.* studied the precipitation of NbC carbide in α -iron using on-lattice Monte-Carlo simulations [52, 67]. Such approach requires to define an ordered structure with the same organization and the same stoichiometry as the carbide, but with atoms on the rigid lattice sites,

as well as a model describing the energetics of the system. The on-lattice approximation can be justified by the fact that small precipitates must still be coherent with the iron matrix. In other words, coherent precipitates can be seen as precursors of the carbide and used to simulate the first stage of nucleation. Interesting structures suggested in the literature could play the role of a cementite precursor. For example, Zhang *et al.* [218] proposed a metastable intermediate structure (MIS) acting as a 'link' between cementite, ferrite and austenite. However, they did not detail their MIS structure. On the other hand, Schuler *et al.* [169] suggested a structure similar to cementite and coherent with a bcc Fe lattice. They studied the nucleation of this potential cementite precursor using Monte-Carlo simulations and predicted the nucleation of elongated precipitates in the presence of vacancies. Atomic Monte-Carlo methods offer a precise description of the precipitation (formation of clusters, growth...) but they require a knowledge of the interaction between the involved species. Lattice interaction models can be used to describe the main features of the interaction energies between atoms calculated from DFT data. In their study of NbC carbide precipitation, Hin *et al.* [67] used a pair interaction model to reproduce Fe, Nb, C and vacancies (V) interactions. On the other hand, Schuler *et al.* used a many-body model to represent V-C interactions [19, 169].

At the microscopic scale, cementite precipitation has been studied with more phenomenological tools such as the classical nucleation and growth model [50, 146]. This model describes the evolution of the precipitation main characteristics (size, volume fraction, nucleation rate,...). In particular, Perez *et al.* [146] employed a precipitation model based on the nucleation and growth theory to investigate the nucleation of ϵ -carbide and Fe_3C in low-carbon steels.

In this chapter, we present a modelling approach in order to investigate the nucleation of cementite in ferrite. To that end, we identified a new possible representation of cementite on a bcc lattice. Then, we parameterized effective-interaction and diffusion models using DFT data in order to perform equilibrium and kinetic on-lattice Monte Carlo simulations for the study of cementite precipitation in a α -Fe lattice. As a first step, we consider that cementite precipitates in the bcc Fe matrix and neglect the effect of vacancies or grain interfaces.

4.2 An ordered Fe-C structure for the representation of cementite in a bcc lattice: α -cementite

The precipitation of cementite in ferrite requires a very high local C concentration (in the order of 25 at%). This transformation is the result of a complex interplay between displacement of the Fe atoms and a redistribution of the C atoms which can only occur through a well-defined nucleation process. Following the idea that a coherent precipitate would facilitate carbide nucleation in α -Fe, we used ab-initio calculations to find an intermediate structure between ferrite and cementite. We identified a Fe_3C structure similar to cementite, but with Fe atoms in a nearly bcc lattice, while C atoms occupy octahedral interstitial sites and form an ordered structure. This structure is coherent with a bcc Fe lattice, so we called it α -cementite. α -cementite admits a slightly deformed orthorhombic unit cell with its a, b and c lattice parameters equal to 5.11 Å, 6.88 Å and 4.61 Å, respectively. There is a one-to-one relationship between the atoms of true cementite and α -cementite. Fig. 4.1 shows the comparison between both crystal structures.

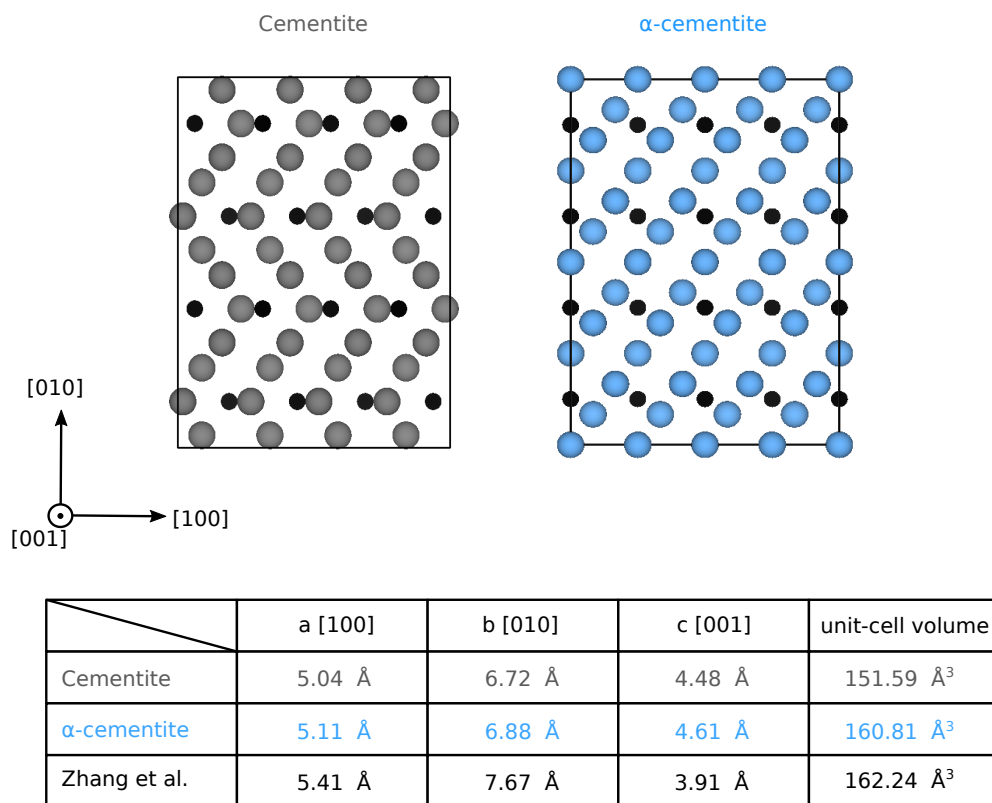


FIGURE 4.1: Comparison between Fe₃C cementite and α -cementite $2 \times 2 \times 2$ supercells crystal structure. Large spheres represent Fe atoms and small black spheres are C atoms.

The orientation relationship (OR) between α -cementite and bcc Fe is given by:

$$\begin{aligned} [100]_{\alpha\text{-cem}} &|| [11\bar{1}]_{bcc} \\ [010]_{\alpha\text{-cem}} &|| [112]_{bcc} \\ [001]_{\alpha\text{-cem}} &|| [\bar{1}\bar{1}0]_{bcc} \end{aligned} \quad (4.1)$$

This OR is similar to the Bagaryatsky OR between cementite and ferrite. The difference between α -cementite and the metastable structure proposed by Zhang *et al.* [218] is not very clear, as the authors did not describe in detail. Nonetheless, their metastable structure lattice parameters are significantly different from our α -cementite lattice parameters (see Fig. 4.1). Similarly, α -cementite volume is higher than Schuler *et al.* [169] suggested precursor for cementite volume (143.33 \AA^3). The transition between α -cementite and cementite occurs through a shear strain in the $([100]_{\alpha\text{-cem}}, [010]_{\alpha\text{-cem}})$ plane plus a small compression (8.5 % in volume).

We studied the relative stability between cementite and α -cementite according to their carbon concentration. The formation energy of both Fe_3C_x structures according to their fractional occupation of C sites x is given Fig. 4.2. Below 75% of C sites occupation, α -cementite is energetically more favorable than cementite. On the other hand, when the C occupation almost reaches 100%, cementite becomes slightly energetically more favorable than α -cementite. In addition, stoichiometric α -cementite ($x = 1$) is energetically more favorable than the cementite representation suggested by Schuler *et al.* α -cementite could therefore act as a metastable precursor of cementite at intra-granular sites in ferrite. Since stoichiometric α -cementite and the true cementite admit a relatively similar formation energy, we used α -cementite as a representation of cementite for our on-lattice MC study. In order to perform MC simulations, we built a thermodynamic model to reproduce carbon interactions and the stability of the α -cementite phase on a bcc rigid lattice.

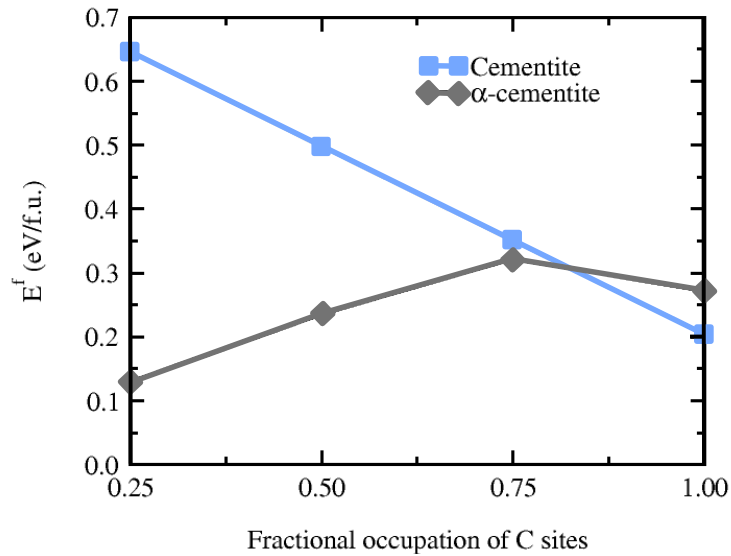


FIGURE 4.2: Comparison between Fe_3C_x cementite and α -cementite formation energies according to the occupation of C x (in eV/f.u.)

4.3 Effective interaction model (EIM) for carbon interactions and precipitation in ferrite

In this section, we detail the development of an on-lattice interaction model that describe the interactions between carbon atoms in ferrite from a collection of ab-initio data. As a first step, we consider that there are no Fe vacancies and that C atoms are located on the interstitial sites of a perfect bcc lattice. A set of C binding (or interaction) energies in the α -Fe matrix with different local C concentrations were calculated using DFT. Then, a thermodynamic cluster-expansion model is parameterized from these DFT data. The model is used as input in equilibrium Monte-Carlo simulations in order to verify its validity.

4.3.1 DFT calculations

There are numerous ab-initio studies on the properties of C interactions in ferrite (represented by bcc Fe with C interstitials). It is well-known that the energetically most favorable position for a carbon interstitial is the octahedral site [3, 38, 46, 48, 81, 159], in agreement with experimental observations [212]. Therefore, we used DFT to calculate the binding energy between C atoms in octahedral interstitial sites in bcc Fe. The total binding energy of n C atoms in bcc iron is defined by:

$$E^b(C_n \text{ in bcc Fe}) = nE^f(C \text{ in bcc Fe}) - E^f(C_n \text{ in bcc Fe}), \quad (4.2)$$

where $E^f(C \text{ in bcc Fe})$ and $E^f(C_n \text{ in bcc Fe})$ are the formation energy of an isolated C interstitial and the formation energy of n C atoms in bcc Fe, respectively. Ultimately, the total binding energy does not depend on the choice of Fe or C reference states involved in the calculation of the formation energy. A positive binding energy implies an attractive interaction (exothermic clustering reaction), while a negative binding energy implies a repulsive interaction (endothermic clustering reaction). We considered two types of C distributions in an α -Fe matrix: (i) C_n octahedral interstitial clusters ($2 \leq n \leq 9$) in bcc Fe and (ii) C atoms in $2 \times 2 \times 2$ α -cementite supercells with various stoichiometries. These two data sets contain 49 and 24 configurations, respectively. The binding energies between 2 C atoms in bcc Fe are given Fig. 4.4. They are in good agreement with previous DFT data from Domain *et al.* [38] and Barouh *et al.* [18]. Domain *et al.* calculations were performed using the VASP code with ultra-soft pseudo-potentials, the Perdew and Zunger functional and the GGA approximation. On the other hand, Barouh *et al.* calculations are based on the GGA as implemented in the SIESTA code. Like Domain *et al.*, we found that neighbouring carbon atoms repel each other but that longer range interactions admit some slightly positive binding energies. The formations of carbon clusters might therefore be possible without the presence of Fe vacancies. Our C-pairs binding energies are overall positively shifted wrt Barouh *et al.* negative values. The total binding energy of C_n clusters and α -cementite with various stoichiometries according to the number of C atoms are represented in Fig. 4.5(a) and Fig. 4.5(b), respectively. The total binding energy of the C_n clusters are mostly repulsive or almost zero. However, we also reported a few configurations with positive binding energies, which confirms our previous assertion regarding the possible formation of C clusters in bcc Fe without defects. α -cementite type configurations are attractive and significantly higher (i.e. energetically more favorable) than all the calculated C clusters in bcc iron. The highest total binding energy per carbon atom was obtained for stoichiometric α -cementite.

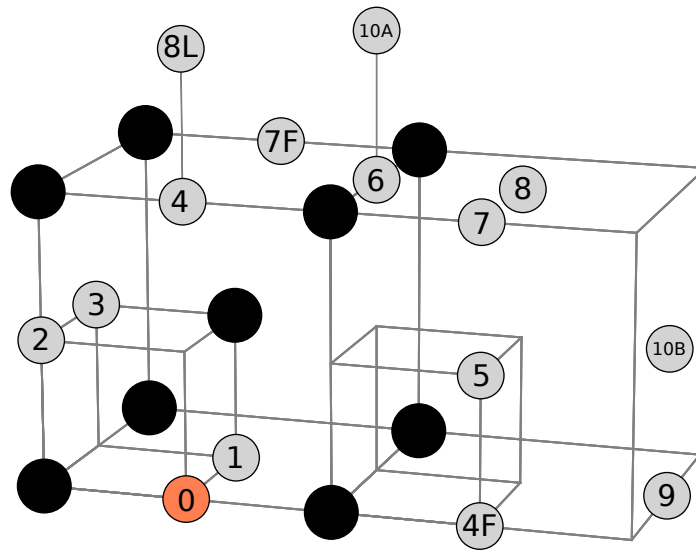


FIGURE 4.3: Schematic view of the nearest-neighbors (nn) octahedral sites in a bcc Fe lattice. Black circles are Fe atoms. Grey circles denote the nn of a given octahedral site (red circle labeled "0"). Note that there are two nonequivalent 4nn, 7nn, 8nn and 10nn. For example, there is an Fe atom between the octahedral site "0" and its 4nn "F", while there is no Fe atom between the octahedral site "0" and its 4nn.

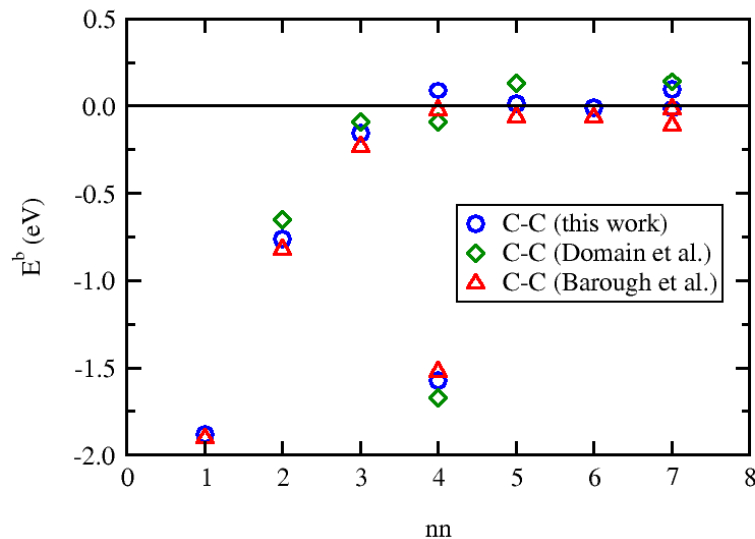


FIGURE 4.4: Binding energy (in eV) of C_2 pairs in $4 \times 4 \times 4$ bcc Fe supercells as function of the nn distance between the C atoms (as described in Fig. 4.3). Our results (blue circles) are compared with previous ab-initio data from Domain *et al.* [38] and Barouh *et al.* [18].

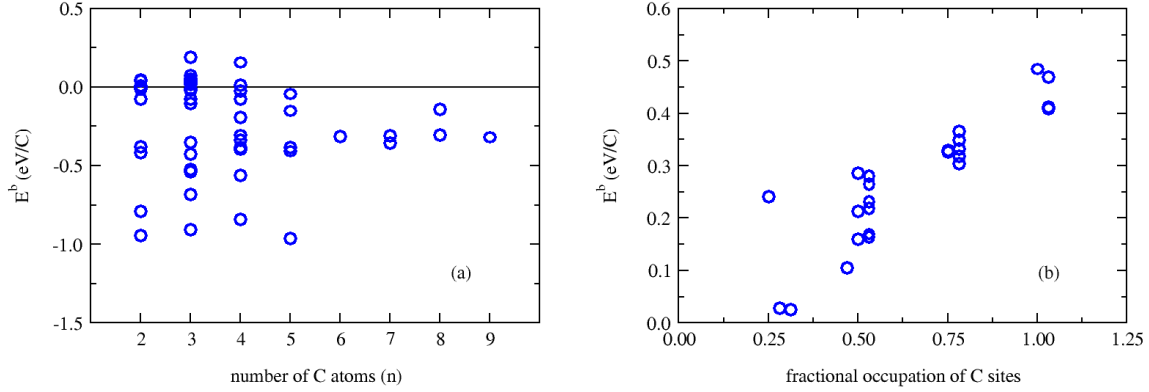


FIGURE 4.5: (a): Total binding energy (in eV/C) of C_n clusters in bcc Fe and as function of the number of C atoms in the cluster (n).
 (b): Total binding energy (in eV/C) of α -cementite with various stoichiometries according to the fraction of C sites occupied.

4.3.2 Parameterization of the EIM from DFT data

We used a cluster expansion model to express the total binding energy between C atoms occupying the interstitial octahedral sites in a perfect bcc lattice:

$$E^b = \frac{1}{2!} \sum_{i,j} n_i^C n_j^C v^{\eta(ij)} + \frac{1}{3!} \sum_{i,j,k} n_i^C n_j^C n_k^C v^{\eta(ijk)} + \frac{1}{4!} \sum_{i,j,k,l} n_i^C n_j^C n_k^C n_l^C v^{\eta(ijkl)} + \dots, \quad (4.3)$$

where n_i^C is occupation number of the octahedral site i ($n_i^C = 1$ if the site is occupied by a C atom and 0 if the site is empty). $v^{\eta(ij)}$ is the pair-interaction between C atoms located in the sites i and j according to their distance η_{ij} . Similarly, $v^{\eta(ijk)}$ is the three-body interaction between C atoms located in the i , j and k sites with η_{ijk} a three-components vector giving the distances between i and j , j and k and k and i . The four-body interaction is given by $v^{\eta(ijkl)}$, with $\eta(ijkl)$ the neighbor distance between each pair of sites.

Since we calculated some positive (attractive) C-C pairs in bcc iron, we started with a simple pair interaction Hamiltonian, taking into account C-C interactions up to the 7nn shell. This pair-interaction model also includes the energetically unfavorable 4nn and 7nn octahedral sites in the bcc lattice. It turned out that such straightforward Hamiltonian cannot reproduce the DFT binding energies with accuracy. In particular, this kind of Hamiltonian wrongly predicted that some carbon clusters had a higher binding energy than α -cementite. We therefore added some multiple-body interactions in order to obtain an effective interaction model in good agreement with DFT data. This many-body Hamiltonian takes into account the symmetries of the system and differentiates non-equivalent interactions in bcc Fe. During the parameterization of the model, we focused on the energetically more favorable configurations. In particular, since 1nn, 2nn and 3nn C-C interactions are highly repulsive, we only fitted DFT configurations without C-C distances below the 4nn (38 configurations among the two data sets). The resulting interactions for the many-body Hamiltonian are presented Table 4.2. The pair-interaction terms are just the DFT pair binding energies. Four positive three-body terms were introduced to stabilize α -cementite type configurations, while three negative three-body terms and

one negative four-body term were introduced to destabilize some carbon clusters in bcc iron. As the distances between C atoms in α -cementite are relatively large (beyond the 5nn), some three-body stabilizing interactions terms take into account distances up to the 10nn shell.

4.3. Effective interaction model (EIM) for carbon interactions and precipitation in γ_9 ferrite

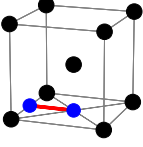
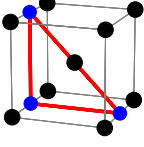
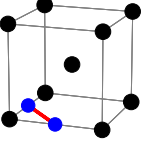
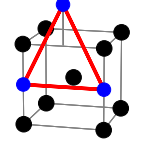
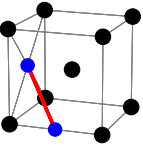
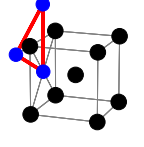
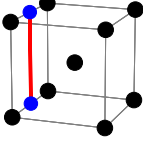
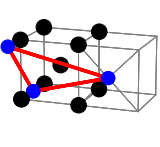
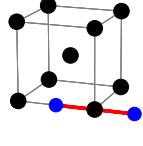
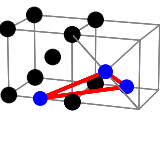
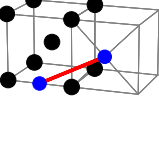
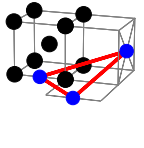
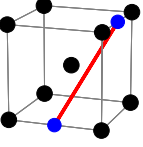
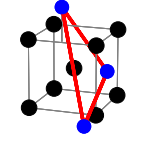
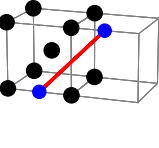
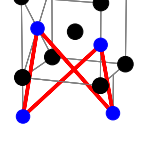
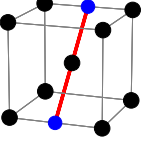
Schematic view	Parameter (eV)	Schematic view	Parameter (eV)
	$v^1 = -1.883$		$v^{447F} = -0.049$
	$v^2 = -0.761$		$v^{455C} = -0.050$
	$v^3 = -0.153$		$v^{455D} = -0.050$
	$v^4 = 0.087$		$v^{71010C} = 0.120$
	$v^{4F} = -1.575$		$v^{557} = 0.041$
	$v^5 = 0.015$		$v^{71010D} = 0.050$
	$v^6 = -0.011$		$v^{5610} = 0.060$
	$v^7 = 0.045$		$v^{555577} = -0.230$
	$v^{7F} = -0.018$		

TABLE 4.2: Schematic view and value (in eV) of each interaction parameter of the thermodynamic model. Fe atoms are in black and C atoms are in blue.

To ensure the consistency of our Hamiltonian, the M-body interactions must show some sort of convergence with M. To this end, we first compare the many-body interactions with the highest pair interaction (v^1). All the three-body interactions are lower than $0.06 \times v^1$. The four-body interaction is $0.12 \times v^1$, which is a bit high compared to the highest three-body interaction v^{71010B} . This four-body interaction was introduced to destabilize some C_n clusters involving 5nn and 7nn C atoms. The correlation between DFT total binding energies and the total binding energies predicted by our many-body Hamiltonian are given Fig. 4.6. Overall, the total binding energies of energetically favorable configurations are in good agreement with DFT data. In particular, the predicted total binding energy for stoichiometric α -cementite (0.52 eV/C) is close to the DFT value (0.48 eV/C). In the case of repulsive configurations, the correlation between DFT data and the model is less good as some C clusters are predicted to be much more unfavorable.

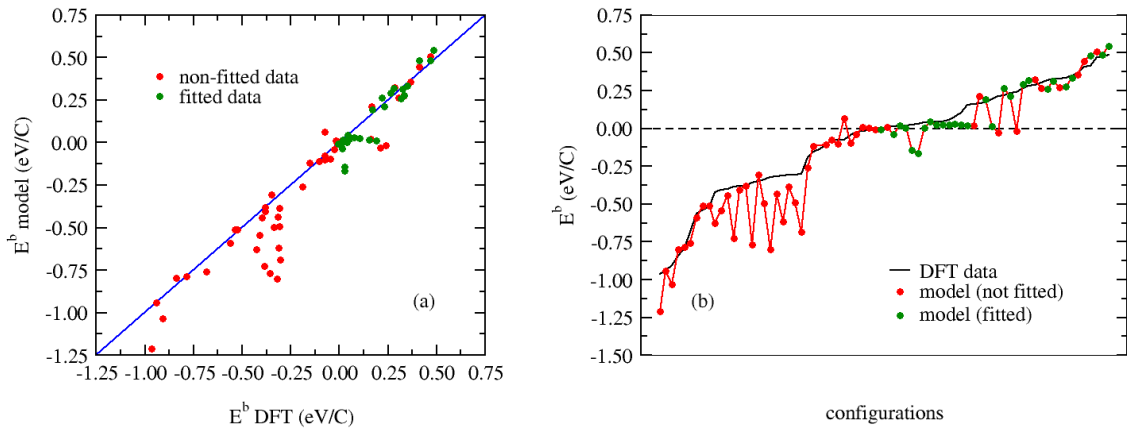


FIGURE 4.6: (a) and (b): Correlation between the total binding energies predicted by our thermodynamic model and DFT data (in eV/C). Only configurations without 1nn, 2nn or 3nn (in green) were used for the fitting of the model interactions while configurations with C-C distances below the 4nn (in red) were not considered for the fitting of the model parameters.

4.3.3 Equilibrium properties

The thermodynamic model obtained from DFT data can be coupled with on-lattice Monte Carlo simulations to study the formation of carbon precipitates in ferrite. To that end, we consider a rigid bcc lattice and its associated interstitial octahedral sublattice, with periodic boundary conditions. Atomic Monte-Carlo simulations based on a Metropolis algorithm (see Sec. 1.2) are carried out to investigate the equilibrium properties of the system. Monte-Carlo simulations explore all the possible configurations and can reveal unexpected stable cluster or precipitate configurations. Such simulations are therefore useful to check the validity of our thermodynamic model.

4.3.3.1 Characterization of the precipitates

We performed equilibrium MC simulations starting from a random C solid solution in bcc Fe, with C concentration included between 0.5 and 5 atomic percent and temperatures varying between 300 K and 1000 K. The carbon concentration and the temperature are fixed during the simulation (canonical ensemble). Simulation boxes typically contain $2 \times N^3$ bcc Fe atoms, with $72 \leq N \leq 80$. Stoichiometric Fe_3C

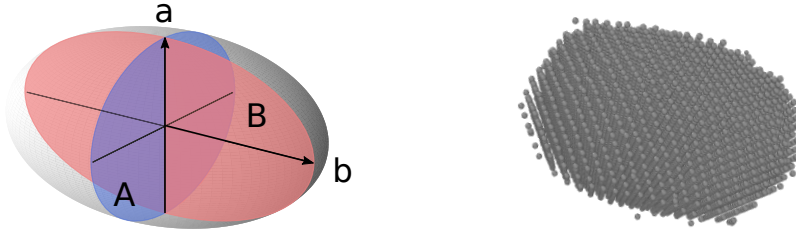


FIGURE 4.7: Schematic view (and example) of our elongated, spheroid equilibrium shape for α -cementite precipitate.

α -cementite is the only equilibrium precipitate predicted by MC simulations (no unexpected ordered structure were observed). The precipitates admit an oblate (flattened) spheroid shape with its minor axis in the $[110]_{\alpha\text{-cem}} \parallel [101]_{\text{bcc}}$ direction. A schematic view of the elongated, spheroidal equilibrium shape is given by Fig. 4.7. To investigate further the evolution of the precipitates shape, we applied equilibrium MC simulation to an α -cementite sphere with a large radius (36 Å) at temperatures included between 300 K and 900 K. We observed that the precipitates significantly flattened in the $[110]_{\alpha\text{-cem}} \parallel [101]_{\text{bcc}}$ direction with the increasing temperature. At low temperature (e.g. 300 K), the precipitates kept a faceted spherical shape. However, additional equilibrium MC simulations initialized with more elongated shapes have shown that this faceted sphere shape is a local minimum and that elongated spheroidal precipitates are energetically more favorable (in average +0.01 eV/C), even at low temperatures.

4.3.3.2 Interface energy

We investigated several relevant interfaces between α -cementite and the matrix. The interface energy between an isolated precipitate and the matrix is given by:

$$E_{\text{int}} = \frac{E_{\text{tot}} - E_{\text{precipitate}} - E_{\text{matrix}}}{A}, \quad (4.4)$$

where E_{tot} is the total energy of the system, $E_{\text{precipitate}}$ is the total energy of the bulk precipitate and E_{matrix} is the total energy of bulk the matrix. A is the interface area between the precipitate and the matrix. We performed equilibrium MC simulations to study the evolution of thick (> 25 Å) α -cementite slices with several orientations in bcc Fe. The initial simulation box can be tricky to build: the α -cementite slices must imperatively respect the periodicity of the simulation box, while remaining sufficiently thick. The distance between the α -cementite slice and its own image by periodicity must also be large enough (typically larger than 40 Å). As a first step, we focus on the most relevant (such as the interfaces between the $[100]$, $[010]$ or $[001]$ directions of α -cementite and the bcc matrix) or easy-to-build interfaces. The interface energies obtained from the equilibrium MC simulations are presented Fig. 4.8. The lower interface energy is in the $[110]_{\alpha\text{-cem}} \parallel [101]_{\text{bcc}}$ interface, which corresponds to the minor axis of the α -cementite spheroid precipitates. Consequently, α -cementite precipitates display larger interfacial areas with the bcc Fe matrix in this direction. The interface energy obtained through the Gibbs-Thomson formula (in black) is slightly higher than the other calculated interface energies at low temperatures, but

exceedingly high beyond 700 K. Our calculated interface energies can be compared with previous data for the cementite/ferrite interface. Guziewski *et al.* [55, 56], Kim *et al.* [89] and Kawakami *et al.* [87] used DFT to investigate the cementite/ferrite interface energy in the Bagaryatskyi OR (similar to the α -cementite/cementite OR). They calculated an interface energy of 0.52, 0.628 and 0.615 J/m², respectively. The experimental value for cementite/ferrite interface energy is 0.7 ± 0.3 J/m² [184]. α -cementite and cementite interface energies are therefore of the same order.

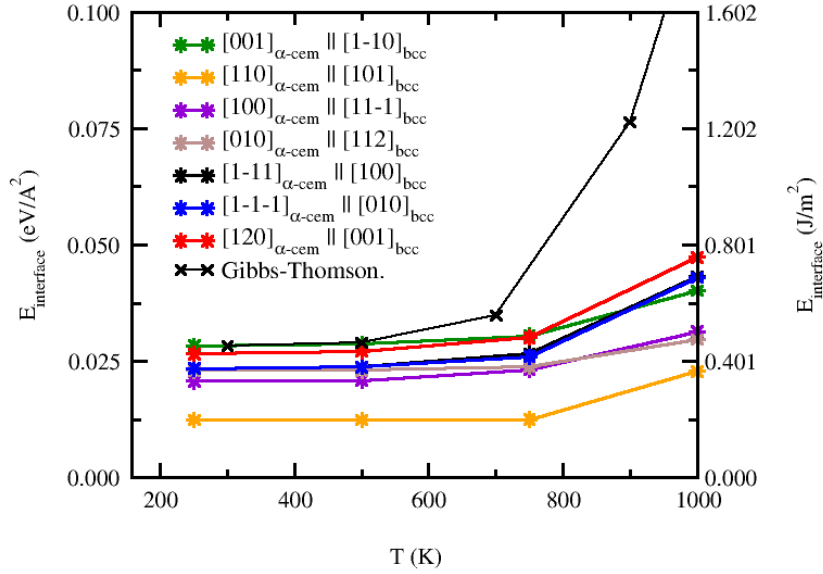


FIGURE 4.8: Interface energy between slices of α -cementite and a bcc Fe matrix with C atoms according to the slices orientation.

4.3.3.3 Solubility limit of C in the matrix in equilibrium with α -cementite

The solubility limit of C atoms in the solid solution in equilibrium with α -cementite is given by:

$$[C]_{matrix,eq} = \exp\left(\frac{-\Delta H}{k_B T}\right), \quad (4.5)$$

with ΔH the solution enthalpy of a C atom in bcc Fe, taking as reference the α -cementite. The C solubility limit and the solution energy obtained from MC simulations are given Fig. 4.9(a). The solubility limits obtained from Monte Carlo simulations can be divided into two categories: (i) the carbon concentrations in solid solutions in equilibrium with α -cementite precipitates with finite interfaces (spheroid-shaped precipitates obtained from random solid solution or α -cementite spheres) or (ii) the carbon concentrations in solid solutions in equilibrium with α -cementite with infinite interfaces (typically slices of α -cementite in the simulation boxes). In both cases, the solubility limit of C is in good agreement with the ones expected from Eq. 4.5 and DFT data taking into account the vibrational entropy. However, the solubility limit obtained for solid solutions in equilibrium with α -cementite admitting finite interfaces is almost two times the solubility limit obtained for solid solution in equilibrium with α -cementite with infinite interfaces. During the growth phase, the solute concentration in the matrix can increase in the vicinity of a precipitate because

of the Gibbs-Thomson effect, following:

$$[C]_{matrix} = [C]_{matrix,eq} \times \exp\left(\frac{2\gamma V_{at}}{k_B T r}\right), \quad (4.6)$$

where $[C]_{matrix,eq}$ is the equilibrium solute concentration (the concentration in solute far from the precipitate, or the concentration in solid solution in equilibrium with α -cementite with an infinite interface) and γ is the interface free energy. This formula is valid for a spherical precipitate with radius of curvature r and a volume per atom V_{at} . In our case, the α -cementite precipitates have a spheroid shape. Nevertheless, for each temperature, we used the radius of a sphere with the same volume to approximate $[C]_{matrix}$ in Eq. 4.6. The results are represented by the black crosses Fig. 4.9(a). For temperatures below 800-700 K, the Gibbs-Thomson effect seems sufficient to explain the difference in solubility limits. However, for higher temperatures, the predicted solubility is more than 100 times higher. The solubility limit of α -cementite can also be compared with the solubility limit of carbon in ferrite in equilibrium with cementite (see Fig. 4.9(b)). α -cementite solubility limit is in good agreement with cementite solubility limit expected from Eq. 4.6 and DFT data taking into account the vibrational entropy. On the other hand, both CALPHAD and experimental data for C solubility limit in ferrite in equilibrium with cementite are lower than the DFT prediction. Interestingly, experimental data from Zhou *et al.* are closer to our calculated solubility limit at low temperatures, while CALPHAD data are closer to our calculated solubility limits at very high temperature. Please note that CALPHAD predictions are generally less reliable at low temperature. We might consider several explanations behind the discrepancy between our calculated solubility limit and experimental data. For instance, the experimental data may be associated to paramagnetic and/or slightly off-stoichiometric cementite. They may also be affected by some impurity effects.

4.4 Kinetics of α -cementite nucleation

4.4.1 C diffusion model in ferrite

In order to investigate the kinetics of α -cementite precipitation, we also built a diffusion model for C migration in ferrite. It is well-known that the minimum energy path for the diffusion of an isolated C in bcc Fe goes from an octahedral site to a nearest one, with the tetragonal site situated halfway as the saddle point. According to our results, the associated energy barrier is 0.86 eV, in good agreement with previous DFT studies [38, 81] and experimental data [210]. The case of a single C interstitial is sufficient to describe dilute concentrations of carbon in bcc iron. However, we want to simulate the precipitation of α -cementite for which C-C distances are greater or equal to the 5nn (3.14 Å). This diffusion model should also reproduce the diffusion of C interstitials in the α -cementite precipitates structure. In that respect, our C diffusion model must account for C migration in bcc Fe lattice zones locally enriched in carbon. To that end, we determine the energy barriers of various C jumps in bcc Fe with C atoms in octahedral interstitial sites, according to their local environment in carbon (see Sec. 1.1.2 for more details on the calculations). As close C neighbors (1nn) are very repulsive (see Fig. 4.4), we focus on initial and final configurations with C-C distances greater or equal than the 2nn (1.98 Å). Our calculated energy

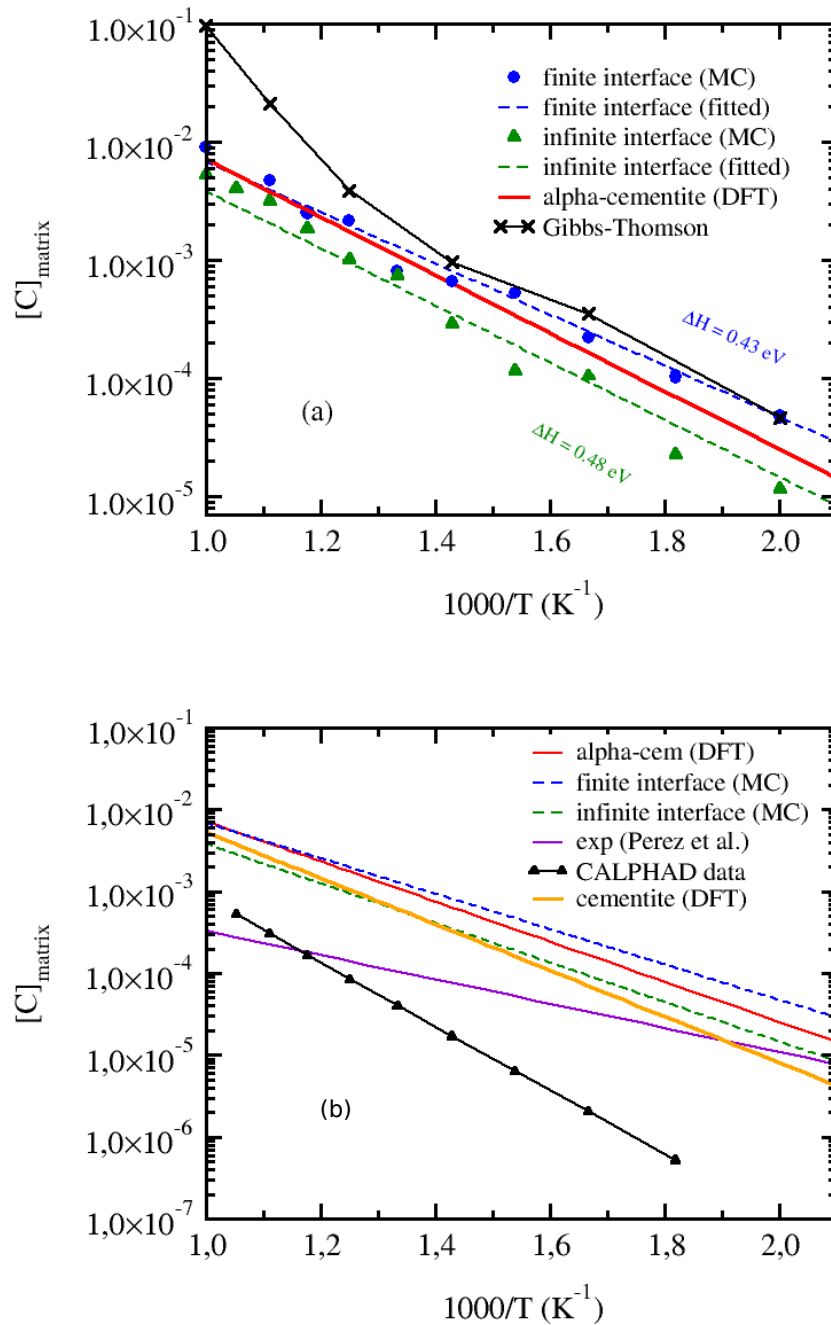


FIGURE 4.9: (a) Comparison between the solubility limit of C in a bcc Fe matrix in equilibrium with α -cementite obtained from equilibrium MC simulations and from Eq. 4.6 with DFT data. (b) Comparison between the solubility limit of C in a bcc Fe matrix in equilibrium with α -cementite and the solubility limit of C in a bcc Fe matrix in equilibrium with cementite according to DFT prediction and experimental data.

barriers are included between 0.01 eV and 1.83 eV. Fig. 4.10 represents the average energy barrier E_m^b for all our calculated C jumps according to the total number of C neighbors up to the 5nn shell in the initial (blue) or final (red) position. Let us take a C atom in an initial position, with a given C local concentration. Overall, the energy barrier of this jumping C atom decreases with the number of C neighbors in the initial position and increases with the number of C neighbors in the final position. This is because in general, if the number of neighboring C atoms is high, the configuration is energetically unfavorable and the C atom tends to jump to a more favorable position with less C neighbors. On the other hand, if the final position of the C atoms after its jumps admits a high number of C neighbors, the associated energy barrier will be relatively high.

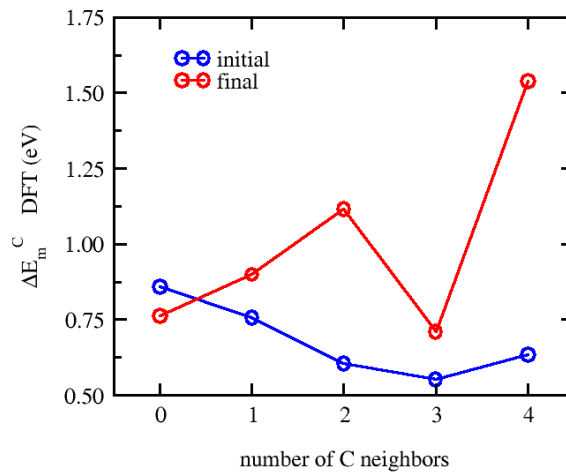


FIGURE 4.10: Average energy barrier of a jumping C atom according its total number of C neighbors (up to the 5nn shell) before (blue) and after (red) the jump.

A simple model to approximate carbon migration barrier in bcc [65] is given by:

$$\Delta E_C^m(if) = \frac{E_f - E_i}{2} + \Delta E_0^C, \quad (4.7)$$

where E_i and E_f are the energies of the system with the jumping C in its initial and final positions, respectively. To ensure the consistency of our modelling approach, we use the binding energies predicted by our thermodynamic (EIM) model for E_i and E_f . ΔE_0^C is usually a constant for such models. In our case, we defined ΔE_0^C as the migration energy of an isolated C atom in bcc Fe ($\Delta E_0^C = 0.86$ eV). The correlation between the migration barriers predicted by this straightforward model and our DFT data is not very good: the Pearson coefficient, R^2 is equal to 0.52. The accuracy of this model relies heavily on the accuracy of the thermodynamic model. If we replace E_i and E_f in Eq. 4.7 by their corresponding DFT values, the correlation between the energy barrier calculated with Eq. 2.4 and DFT data becomes significantly better ($R^2=0.88$). Therefore, even if our thermodynamic model predicts with accuracy the energy of attractive carbon configurations and the stability of α -cementite, the errors on E_i and E_f can build up, leading to a poor approximation of the migration barrier. In particular, the correlation between $E_f - E_i$ predicted by the thermodynamic

model and DFT data is $R^2 = 0.71$. In order to increase the precision of the diffusion model, we added some correlation terms to Eq. 4.7. The new diffusion model is written:

$$\Delta E_C^m(if) = \frac{E_f - E_i}{2} + \Delta E_0^C + \sum_S \alpha_S \frac{N_{C_i}^S + N_{C_f}^S}{2}, \quad (4.8)$$

where $N_{C_i}^S$ and $N_{C_f}^S$ are the number of C neighbors in the S shell wrt to the initial or final position occupied by the jumping atom, respectively. The parameters α_S of each S shell were fitted from our DFT database of migration energies, with cut-off for the S shell varying between the 3nn and the 10nn. R^2 converges to 0.67 for a 5nn distance cut-off. For this reason, we will only use four α_S parameters for our diffusion model ($2 \leq S \leq 5$). The values of the α_s parameters are 0.061, -0.062, 0.011 and -0.088 (eV) for $s = 2, 3, 4$ and 5 , respectively. The correlation between the diffusion model given Eq. 4.8 with these parameters and DFT values for the C energy barriers is presented Fig. 4.11. The new model admits an higher accuracy ($R^2 = 0.67$) and the correlation with DFT values is satisfactory. Improving further this diffusion model is challenging. Taking into account the carbon environment at the saddle point is an option. However, this entails that one must acquire information on the local environment of the saddle-point at each KMC step, which might be very time-consuming. Consequently, we performed KMC simulations using the new diffusion model (Eq. 4.8) coupled with the thermodynamic model.

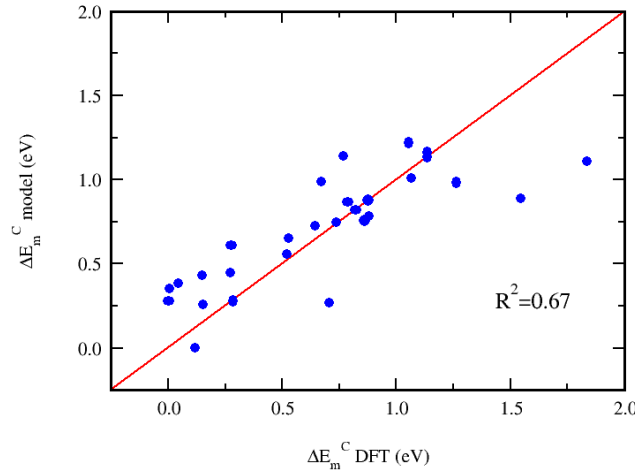


FIGURE 4.11: Comparison between the diffusion model and DFT values for C migration barriers in bcc Fe with different local environment in carbon (in eV).

4.4.2 Kinetic Monte-Carlo simulations

Our C diffusion model in ferrite was implemented in a kinetic Monte-Carlo code in order to study the kinetics of α -cementite nucleation. Unfortunately, our kinetic Monte-Carlo simulations result to be very time consuming. As of today, our longest simulation only reached a few nano-seconds. Despite this small time, we still observed the apparition of small α -cementite nuclei suggesting a rather small critical size for nucleation in these conditions (9-13 C atoms) for high C concentrations (3 atomic percent of carbon or more). Nonetheless, further optimization of the MC

code is needed.

The data obtained directly from DFT calculations (C diffusion coefficients, cementite-matrix interface energies) and from equilibrium and kinetic MC simulations (C solubility limits, average free interface energy) can also be used as input data to parameterize a classical nucleation and growth model.

4.5 Summary

In this Chapter, we implemented a modelling approach to study cementite nucleation in ferrite. We identified an ordered Fe-C structure, with similar atomic organization and the same stoichiometry as Fe₃C cementite, but with Fe atoms residing on bcc-lattice sites. We used this so-called α -cementite as a representation of the cementite carbide, and parameterized effective-interaction and diffusion models using DFT data in order to perform equilibrium and kinetic on-lattice Monte Carlo simulations for the study of cementite precipitation in the α -Fe lattice. As a result, the stoichiometric α -cementite is the only precipitate observed. Our α -cementite precipitates admit an elongated, spheroidal shape. The first α -cementite / ferrite interface energies obtained from equilibrium Monte-Carlo are in the same order of magnitude as previous DFT data, or experimental data for cementite / ferrite interfaces. On the other hand, C solubility limits in the bcc Fe matrix in equilibrium with the α -cementite precipitates are in agreement with DFT predictions, but they are significantly higher than experimental data for C solubility limits in ferrite in equilibrium with cementite at high temperatures.

Our first kinetic Monte-Carlo simulations are promising, but further optimization of our MC code is needed. The data obtained from DFT calculations and MC simulations will also be used as input data to parameterize a classical nucleation and growth model.

Conclusions and perspectives

The purpose of this thesis was to push forward the understanding of carbides properties. Many features of them are difficult to access experimentally because the volume fraction of carbide phases in steels is generally small and difficult to isolate from the surrounding matrix. In addition, it is extremely challenging to observe directly atomic-scale phenomena such as the property changes induced upon alloying, diffusion and nucleation mechanisms. In this thesis, we employed various models and simulation techniques to address two very common carbides: cementite (M_3C) and M_2C .

We investigated point defects and C diffusion in Fe_3C cementite carbide. First, we used DFT calculations to determine the formation energy of all possible C interstitial sites in cementite, as well as the energy barriers of a large variety of jumps between the lowest-energy interstitial configurations. Then, our DFT data were used as input in a statistical model (as implemented in the KineCluE code) in order to compute carbon diffusion coefficients in cementite. The obtained values are in good agreement with previous experiments measuring the growth rate of cementite.

At variance with experiments, the modelling approach provides information on the migration mechanisms involved at the atomic scale. The diffusion mechanism inferred from a previous MD simulation relied on a high concentration of C Frenkel pairs in cementite. However, the formation energy of a C interstitial is significantly lower than the formation energy of a C Frenkel pair in cementite. Besides, in the carburization experiments the vapor phase acts as a source to provide C interstitials, leading to the growth of cementite. Therefore, the formation energy associated with the creation of a C interstitial is not included in the activation energy of this process. For these reasons, our study proposes that C diffuse via an interstitial mechanism.

We also investigated the effect of an alloying element (Mo, Cr or Mn) on the diffusion properties of C in weakly-alloyed cementite. To this end, we analysed the interaction between a C interstitial and a substitutional solute in cementite. We found that Mn can decrease C diffusion by at most a factor 10 at temperatures up to 500 K and solutes concentration up to a few at%. On the other hand, we predict no significant effect for Mo or Cr weakly-alloyed cementite.

The second part of this thesis focus on alloyed M_3C and M_2C . We used DFT calculations to predict the property changes induced in cementite upon Mo, Cr or Mn alloying, as well as the property changes induced in Mo_2C upon Fe or Mn alloying. Special attention has been paid to the comparison with experimental data. We found that the decrease of cementite Curie temperature observed experimentally upon alloying can be associated with the diminution of its average magnetic moment. The volume change induced by Mo alloying in cementite is governed by size effects and follows a Vegard's law, while the volume change in Mn or Cr alloyed cementite is associated with complex electronic and magnetic behaviors. Nonetheless, $(Fe,Mn)_3C$ and $(Fe,Cr)_3C$ magnetization and volume roughly decrease linearly in the dilute regime. Our DFT predicted alloyed cementite volumes overall agree

with previous experimental data, as well as recent data from Benarosch *et al.*. M_2C volume change upon Fe or Mn alloying also appears to follow a Vegard's law. Unfortunately, to this date, there are no experimental data to compare our results with. The enthalpy of substitution can be used to predict the partitioning of alloying elements between carbides and ferrite. In particular, we found that it is energetically more favorable for Mn to substitute in cementite, while it is not the case for Mo. These results are in good agreement with the high Mn concentration (up to 14%) and low Mo concentration (a few percent) experimentally observed in M_3C in Fe-Mn-C, Fe-Mo-C or Fe-Mn-Mo-C model steels after tempering at 923 K and 973 K. We also predicted that it is more favorable for Mn to partition in Mo_2C than Fe, in agreement with CALPHAD predictions.

Finally, we implemented a modelling approach to study cementite nucleation in ferrite. We identified an ordered Fe-C structure, with similar atomic organization and the same stoichiometry as the cementite, but with Fe atoms residing on bcc-lattice sites. This structure may constitute a possible precursor for cementite precipitates. Employing this α -cementite as a representation of the cementite carbide, we parameterized effective-interaction and diffusion models using DFT data in order to perform equilibrium and kinetic on-lattice Monte Carlo simulations for the study of cementite precipitation in the α -Fe lattice. As a result, the stoichiometric α -cementite is the only precipitate observed. The α -cementite / ferrite interface energies obtained from equilibrium Monte-Carlo are in the same order of magnitude as previous DFT data, or experimental data for cementite / ferrite interfaces. On the other hand, C solubility limits in the bcc Fe matrix in equilibrium with the α -cementite precipitates are in agreement with DFT predictions, but significantly higher than experimental data for C solubility limits in ferrite in equilibrium with cementite at high temperatures. The data obtained from DFT calculations and MC simulations will also be used as input data to parameterize a classical nucleation and growth model.

During this three-years work, we provided various atomic-scale insights into the properties of carbides. However, as usual in research, the work on this topic is far from being over. For instance, our work on C diffusion in cementite could be extended. As explained above, based on our DFT results in stoichiometric cementite and considering the carburization experimental set-up, we proposed an interstitial mechanism for C diffusion in cementite. Yet, there may be a competition between this mechanism and the Frenkel-pair mechanism proposed in the literature, especially in the case of under-stoichiometric cementite and/or high temperature. In particular, according to both experimental and theoretical studies, C vacancy concentration in cementite could reach up to a few percent. The carbon and metal vacancies may play a significant role to drive atomic diffusion, which is a very interesting perspective for a future study. Overall, the modelling approach based on DFT calculations coupled with statistical tools could be used to study the diffusion in other carbides ($M_{23}C_6, \dots$).

The Curie temperature of cementite and other carbides is generally significantly lower the Curie temperature of ferrite. In this work, we discussed effect of magnetic disorder in 'pure' Fe_3C (Chap. 2) and in Mo or Mn alloyed cementite in the dilute regime (Chap. 3). However, an accurate investigation of the impact of magnetic excitation and transition can be an interesting future work. Similarly, the effect of the vibrational entropy in M_3C and M_2C was only briefly discussed. Overall, finite temperature effect on carbides are still poorly known and represent a very interesting subject of study.

In Chap. 3 and Chap. 4, cementite and M_2C carbides were considered as infinite phases. However, the interface between a carbide and ferrite can play an important role in various carbide properties. Therefore, the role of carbides / ferrite interfaces is an important perspective for future studies. Furthermore, our work on alloyed M_3C and M_2C could be extended to other carbide phases (such as the ζ -carbide observed in Benarosch *et al.* model steels).

In our last chapter, we presented a modelling approach to study the nucleation of cementite. The presence of vacancies can affect the precipitation of carbides. We could therefore modify our models to take into account the effect of vacancies. As a first step, we considered that cementite precipitates in the Fe matrix. However, according to experimental data, cementite precipitation is frequently heterogeneous. Our effective-interaction model and diffusion model should therefore be extended to take into account the presence of grain boundaries.

There is still a long way to go before we understand perfectly the properties of carbides. Nonetheless, computational modelling is an useful tool to overcome experimental challenges and access the properties of these complicated phases. As a result, the number of theoretical studies on carbides is increasing slowly but surely, and it has been a privilege to contribute.

Synthèse en français

La formation de carbures tels que le M_3C (cémentite) ou le M_2C peut affecter fortement les propriétés mécaniques des aciers. Ce phénomène a un impact significatif lorsque les aciers sont utilisés comme matériaux de structure pour diverses applications technologiques. En particulier, la présence de certains carbures dans les aciers ferritiques utilisés dans l'industrie nucléaire (par exemple l'acier 16MND5 présent dans les cuves des réacteurs à eau pressurisée) pourrait conduire à leur fragilisation.

Cette thèse s'inscrit dans un projet multi-échelles couplant métallurgie appliquée et recherche fondamentale appelé ECEC (Étude amont sur la Cinétique d'Évolution des Carbures). L'objectif de ce projet est de mieux comprendre le lien entre la microstructure de l'acier 16MND5 et ses propriétés mécaniques, en commençant par des systèmes simplifiés (aciers modèles). A cet effet, deux thèses ont été initiées en 2018. La première, menée par Anna Benarosch, s'appuie sur une démarche expérimentale couplée à une modélisation semi-empirique (calcul CALPHAD) afin de construire un modèle thermocinétique d'évolution de la précipitation des carbures dans les aciers bainitiques. Cette étude a été réalisée sur des aciers modèles simplifiés tels que les alliages ternaires Fe-C-Mo ou les alliages quaternaires Fe-Mo-Mn-C. Néanmoins, beaucoup de données fondamentales restent difficiles voire impossibles à obtenir expérimentalement. En effet, les carbures ne représentent qu'une faible fraction volumique des échantillons et ils sont difficiles à isoler de la matrice environnante. De plus, il est extrêmement difficile d'observer directement des phénomènes se produisant à l'échelle atomique comme la diffusion, la nucléation ou les changements de propriétés induits par la présence d'éléments d'alliage dans les carbures. Des outils de modélisation informatique peuvent être utilisés pour étudier ces propriétés. Par exemple, la structure cristalline mais aussi les propriétés magnétiques, électroniques et élastiques de la cémentite [13, 28, 35, 43, 60, 62, 79, 80, 117, 133], ainsi que du Mo_2C [59, 71, 84, 110, 148, 161, 204, 209] ont été largement étudiées en utilisant la Théorie de la Fonctionnelle de la Densité ou DFT (Density Functional Theory). Cependant, de nombreuses propriétés de ces carbures sont encore inconnues. En particulier, les mécanismes d'agglomération et de diffusion du carbone jouent un rôle essentiel lors des processus de nucléation et de croissance des carbures dans le fer- α , ou lors de la transition entre deux carbures de nature différente. Ces propriétés dépendantes de l'environnement local sont encore mal connues. De plus, la présence d'éléments d'alliage (tels que Mo, Cr ou Mn) dans les aciers peut favoriser la précipitation des carbures. Or, jusqu'à présent, on les propriétés des carbures alliés demeurent relativement méconnues. L'objectif de cette thèse est d'étudier ces questions ouvertes. Pour cela, nous avons principalement utilisé des calculs DFT couplés à une modélisation statistique.

Les principaux outils de simulation utilisés dans cette thèse sont décrits dans le

Chapitre 1. En particulier, les principes fondamentaux des calculs DFT et des simulations de Monte-Carlo (MC) y sont résumés. Dans ce premier chapitre, nous introduisons également certaines méthodes et des détails de calcul spécifiques. Enfin, nous donnons l'expression de diverses grandeurs physiques qui seront utilisées dans les chapitres suivants.

Les résultats de cette thèse sont regroupés en trois chapitres différents (Chapitre 2 à 3), comprenant chacun un état de l'art et un résumé détaillés.

Dans le Chapitre 1, nous avons étudié la stabilité relative de divers défauts (lacunes de carbone, interstitiels de carbone, paires de Frenkel de carbone) dans la cémentite stœchiométrique (Fe_3C). Nous nous sommes aussi intéressés à la diffusion du carbone dans la cémentite pure et faiblement alliée (respectivement Fe_3C et $(\text{Fe}_{1-x}\text{M}_x)_3\text{C}$ avec $\text{M} = \text{Mo}, \text{Cr}$ ou Mn). Des calculs DFT systématiques ont été effectués afin de déterminer l'énergie de formation de tous les interstitiels de carbone identifiés, ainsi que les barrières d'énergie d'une grande variété de sauts entre les configurations interstitielles de basse énergie. Le code open-source KineCluE [166, 168] a ensuite été utilisé pour calculer les coefficients de diffusion du carbone dans la cémentite en utilisant les résultats DFT comme données d'entrée. Les coefficients de diffusion obtenus dans la cémentite Fe_3C sont en bon accord avec les données expérimentales présentes dans la littérature et tirées d'expériences de carburisation. De plus, cette étude fournit des informations sur les mécanismes de migration du carbone à l'échelle atomique qui ne sont pas directement accessibles par les expériences. Ainsi, nous avons mis en évidence deux mécanismes élémentaires de diffusion : soit un saut direct d'un C interstitiel d'un site octaédrique à un autre, soit un saut indirect où le C interstitiel se déplace et prend la place d'un C intrinsèque, tandis que ce dernier migre vers un site interstitiel voisin.

Même si nos coefficients de diffusions sont comparables aux résultats obtenus dans la littérature par Levchenko et al. [104] à travers des simulations semi-empirique de dynamique moléculaire (MD), les mécanismes à l'origine de la diffusion du carbone sont différents. En effet, le mécanisme précédemment déduit de simulations MD repose sur une concentration élevée de paires de Frenkel de carbone (au moins localement). Or, l'énergie de formation des paires de Frenkel de carbone issue de nos calculs DFT est environ trois fois plus élevée que les résultats MD, ce qui implique que le mécanisme proposé par Levchenko et al. a une probabilité plus faible de se produire. Ainsi, nous considérons que le carbone diffuse via des mécanismes interstitiels impliquant des sauts entre les sites interstitiels octaédriques. De plus, dans le cadre des expériences de carburisation, la phase vapeur agit comme une 'source' et vient fournir des interstitiels de carbone conduisant à la croissance de la cémentite. L'énergie de formation associée à la création des atomes de C interstitiels n'est donc pas comprise dans l'énergie d'activation du processus de diffusion.

Dans un second temps, nous avons aussi étudié les effets possibles des éléments d'alliage (jusqu'à quelques pourcents de Mo, Cr ou Mn) sur les propriétés de diffusion du C dans la cémentite. Pour cela, nous avons d'abord calculé et analysé l'énergie d'interaction entre un C interstitiel et l'un des trois solutés de substitution. Autour de chacun des soluté (Mo, Cr ou Mn), il existe des sites énergétiquement favorable (attractifs) pour un interstitiel de carbone. Pour un soluté de Mo, Mn ou Cr, la localisation de ces sites est respectivement régie par l'effet de taille, le magnétisme du soluté ou la redistribution de charges électroniques. Concernant l'influence des solutés substitutionnels sur les coefficients de diffusion du carbone, la présence de Mn peut ralentir la diffusion jusqu'à un facteur 10 pour des températures atteignant

500 K et des concentrations de soluté jusqu'à quelques pourcents atomiques. Dans le cas de solutés de Mo ou de Cr, nous ne prévoyons aucun effet sur la diffusivité du carbone pour les faibles concentrations en élément d'alliage considérées.

En tant que première étape dans l'étude de la diffusion dans la cémentite, nous n'avons considéré que la cémentite stœchiométrique (M_3C). Cependant, selon certaines études expérimentales et théoriques, la concentration en lacunes de C dans la cémentite pourrait atteindre jusqu'à quelques pourcents. Les lacunes pourraient donc jouer un rôle significatif dans la diffusion du carbone, ce qui représente une perspective d'étude intéressante. Ainsi, pour la cémentite sous-stœchiométrique et/ou à haute température, on pourrait imaginer une 'concurrence' entre notre mécanisme de diffusion interstitiel et le mécanisme de paire de Frenkel proposé précédemment par Levchenko et ses co-auteurs.

Ces résultats ont fait l'objet d'une publication dans *Physical Review Material* [26].

L'objectif du chapitre 2 est d'étudier plusieurs propriétés de la cémentite alliée en Mo, Mn ou Cr (M_3C), ainsi que les propriétés du carbure M_2C allié en Fe ou Mn. A cet effet, des calculs DFT ont été effectués pour une large gamme de concentrations en éléments d'alliage. En particulier, nous avons déterminé le changement de volume et de moment magnétique de la cémentite alliée en Mo, Cr ou Mn. Nous avons constaté que le volume de cémentite alliée en Mo augmente linéairement avec la concentration en soluté, suivant une loi de Vegard. En parallèle, nous observons une dilution magnétique due au moment magnétique très faible (presque non-magnétique) des solutés de Mo. Par conséquent, les effets de taille régissent le changement de volume de la cémentite lors de l'alliage en Mo. D'un autre côté, le volume de la cémentite alliée en Mn suit de près le changement de moment magnétique, ce qui indique clairement un effet magnéto-volumique. Dans la cémentite, les solutés de Mn admettent un spin inférieur aux valeurs de spin du Fe et parallèle à ceux-ci pour les faibles concentrations (<10%). Au-delà de cette limite, le spin de certains solutés de Mn bascule et devient antiferromagnétique par rapport au spin des atomes de Fe en raison de du couplage antiferromagnétique entre solutés de Mn. Le cas de la cémentite alliée en Cr est moins trivial. Même si les atomes de Cr sont légèrement plus gros que les atomes de Fe, le volume de la cémentite alliée en Cr diminue jusqu'à environ 30% d'occupation en Cr. Cette diminution du volume est associée à une diminution du moment magnétique moyen. En dessous de cette teneur en Cr de 30%, les solutés de Cr sont couplés de manière antiferromagnétique avec les atomes de Fe de la cémentite. Pour des concentrations de Cr plus importantes, la cémentite devient progressivement non magnétique, tandis que son volume augmente. Le volume de cémentite alliée en Cr est donc régi par un effet magnéto-volumique pour des concentrations de Cr plus faibles, et par des effets de taille pour des concentrations de Cr plus élevées. Le changement de volume de la cémentite alliée peut être comparé aux résultats expérimentaux obtenus à partir d'analyses par diffraction des rayons X en utilisant des raffinements de Rietveld [20, 83]. Dans l'ensemble, nous observons la même tendance globale entre nos résultats DFT et les données expérimentales. De même, la diminution de la température de Curie de la cémentite alliée au Cr ou au Mn observée expérimentalement [175, 194, 196] lors de l'alliage est corrélée à la diminution du moment magnétique moyen prédit à partir de nos résultats DFT.

L'enthalpie de substitution peut être utilisée pour prédire la répartition des éléments d'alliage entre les carbures et la matrice. Dans le cadre de notre étude, nous avons calculé l'enthalpie de substitution du Mo ou du Mn entre la ferrite et la cémentite,

et l'enthalpie de substitution du Fe ou du Mn entre la ferrite et le carbure Mo_2C . D'après nos calculs, le Mn préfère rejoindre la cémentite alors qu'il est énergétiquement défavorable pour le Fe ou le Mn de se substituer dans le Mo_2C . Ces résultats sont globalement en accord avec les données expérimentales. D'autre part, nous prédisons que la concentration en Mn est supérieure à la concentration en Fe dans le M_2C , en accord avec les données CALPHAD mais contrairement aux observations expérimentales.

La température de Curie des carbures est souvent faible par rapport à celle du fer cubique centré. A ce titre, l'effet du désordre magnétique et l'effet de l'entropie vibrationnelle dans ces carbures sont brièvement discutés. Si l'on tient compte du paramagnétisme de la cémentite, le comportement relatif des solutés de Mo ou Mn reste identique et s'accompagne d'une diminution des enthalpies de substitution. Au contraire, à température finie, l'effet de l'entropie vibrationnelle augmente l'enthalpie libre de substitution, sauf dans le cas de soluté de Fe dans le Mo_2C .

Le dernier chapitre de résultat (Chapitre 3) présente une approche de modélisation pour étudier la nucléation de la cémentite dans la ferrite. Pour commencer, nous avons identifié une structure Fe-C ordonnée, avec une organisation atomique similaire et la même stœchiométrie que la cémentite Fe_3C , mais avec des atomes de Fe résidant sur les sites du réseau cubique centré. Par la suite, nous appelons cette structure cémentite- α et l'utilisons comme représentation de la cémentite sur ce réseau. Dans un second temps, nous avons paramétré des modèles d'interaction et de diffusion à l'aide de données DFT afin d'effectuer des simulations Monte Carlo d'équilibre et cinétiques sur réseau pour l'étude de la précipitation de cémentite dans le réseau Fe- α . La cémentite- α stœchiométrique est le seul précipité observé lors des simulation Monte-Carlo à l'équilibre. Nos précipités de cémentite- α admettent une forme allongée et sphéroïdale. Les énergies d'interface entre la ferrite et la cémentite- α obtenues à partir de simulations Monte-Carlo à l'équilibre sont du même ordre de grandeur que les données expérimentales ou DFT sur les interfaces ferrite/cémentite présentes dans la littérature. Les limites de solubilité du C dans le fer cubique centré à l'équilibre avec les précipités de cémentite- α sont en accord avec les prédictions DFT, mais elles sont significativement plus élevées que les données expérimentales pour les limites de solubilité du C dans la ferrite en équilibre avec la cémentite à haute température. Nos premières simulations Monte-Carlo cinétiques sont prometteuses, mais une optimisation de notre code MC cinétique est nécessaire. A court terme, les résultats obtenus à partir des calculs DFT et des simulations MC seront également utilisées comme données d'entrée pour paramétrer un modèle phénoménologique de nucléation, croissance et coalescence.

Les principaux résultats obtenus au cours de cette thèse et les perspectives qu'ils soulèvent sont résumés dans une conclusion présente en fin de manuscrit. Parmi les perceptives soulevées lors de cette thèse, nos travaux sur la diffusion du C dans la cémentite pourraient être étendus. En effet, sur la base de nos résultats DFT dans la cémentite stœchiométrique et compte tenu du dispositif expérimental de carburation, nous proposons un mécanisme interstitiel pour la diffusion du C dans la cémentite. Or, il pourrait exister une compétition entre ce mécanisme et le mécanisme des paires de Frenkel proposé dans la littérature, notamment dans le cas de cémentite sous-stœchiométrique et/ou à haute température. En particulier, selon des études expérimentales et théoriques, la concentration de lacunes de C dans la cémentite pourrait atteindre quelques pourcents. Les lacunes de carbone et de métal

peuvent jouer un rôle important dans la diffusion atomique, ce qui est une perspective très intéressante pour une future étude. La température de Curie de la cémentite et des autres carbures est généralement significativement inférieure à la température de Curie de la ferrite. Dans ce travail, nous avons discuté de l'effet du désordre magnétique dans la cémentite Fe_3C « pure » (Chapitre 1) et dans la cémentite alliée à Mo ou Mn dans le régime dilué (Chapitre 2). Cependant, une étude précise de l'impact de l'excitation magnétique et de la transition peut être un travail futur intéressant. De même, l'effet de l'entropie vibrationnelle dans le M_3C et le M_2C n'a été que brièvement discuté. Globalement, l'effet de la température sur ces propriétés des carbures est encore mal connu et représente un sujet d'étude très intéressant.

Dans les Chapitre 2 et Chapitre 3, la cémentite et le carbure M_2C ont été considérés comme des phases infinies. Cependant, l'interface entre un carbure et la ferrite peut jouer un rôle important dans les propriétés du celui-ci. Par conséquent, le rôle des interfaces carbures/ferrite est une perspective importante pour les études futures. De plus, nos travaux sur le M_3C et le M_2C alliés pourraient être étendus à d'autres phases carbures. Dans notre dernier chapitre de résultat (Chapitre 4), nous avons présenté une approche de modélisation pour étudier la nucléation de la cémentite. La présence de lacunes peut affecter la précipitation des carbures. Nos modèles pourraient donc être modifiés pour tenir compte de l'effet des lacunes. Dans un premier temps, nous avons considéré que la cémentite précipite dans la matrice de Fe. Cependant, selon les données expérimentales, la précipitation de la cémentite est souvent hétérogène. Notre modèle d'interaction effectif et notre modèle de diffusion devraient aussi être étendus pour tenir compte de la présence de joints de grains.

Bibliography

- [1] F. Z. Abderrahim, H. I. Faraoun, and T. Ouahrani.
In: Physica B: Condensed Matter 407.18 (Sept. 2012), pp. 3833–3838.
DOI: [10.1016/j.physb.2012.05.070](https://doi.org/10.1016/j.physb.2012.05.070).
URL: <https://doi.org/10.1016/j.physb.2012.05.070>.
- [2] H. Abe, T. Suzuki, and S. Okada.
In: Transactions of the Japan Institute of Metals 25.4 (1984), pp. 215–225.
DOI: [10.2320/matertrans1960.25.215](https://doi.org/10.2320/matertrans1960.25.215).
URL: <https://doi.org/10.2320/matertrans1960.25.215>.
- [3] S. Ahlawat et al.
In: Computational Materials Science 170 (Dec. 2019), p. 109167.
DOI: [10.1016/j.commatsci.2019.109167](https://doi.org/10.1016/j.commatsci.2019.109167).
URL: <https://doi.org/10.1016/j.commatsci.2019.109167>.
- [4] S. A. Al-Salman, G. W. Lorimer, and N. Ridley.
In: Acta Metallurgica 27.8 (Aug. 1979), pp. 1391–1400.
DOI: [10.1016/0001-6160\(79\)90208-6](https://doi.org/10.1016/0001-6160(79)90208-6).
URL: [https://doi.org/10.1016/0001-6160\(79\)90208-6](https://doi.org/10.1016/0001-6160(79)90208-6).
- [5] S. A. Al-Salman, G. W. Lorimer, and N. Ridley.
In: Metallurgical Transactions A 10.11 (Nov. 1979), pp. 1703–1709.
DOI: [10.1007/bf02811704](https://doi.org/10.1007/bf02811704). URL: <https://doi.org/10.1007/bf02811704>.
- [6] S. Alconchel, F. Sapiña, and E. Martínez.
In: Dalton Transactions 16 (2004), pp. 2463–2468.
- [7] A. T. Aldred et al. In: Physical Review B 14 (1 1976), pp. 228–234.
DOI: [10.1103/PhysRevB.14.228](https://doi.org/10.1103/PhysRevB.14.228).
URL: <https://link.aps.org/doi/10.1103/PhysRevB.14.228>.
- [8] A. R. Allnatt. In: Journal of Physics C: Solid State Physics 15.27 (Sept. 1982), pp. 5605–5613. DOI: [10.1088/0022-3719/15/27/016](https://doi.org/10.1088/0022-3719/15/27/016).
URL: <https://doi.org/10.1088/0022-3719/15/27/016>.
- [9] C. K. Ande and M. H. F. Sluiter. In: Metallurgical and Materials Transactions A 43.11 (June 2012), pp. 4436–4444.
DOI: [10.1007/s11661-012-1229-y](https://doi.org/10.1007/s11661-012-1229-y).
URL: <https://doi.org/10.1007/s11661-012-1229-y>.
- [10] C. K. Ande and M. H. F. Sluiter.
In: Acta Materialia 58.19 (Nov. 2010), pp. 6276–6281.
DOI: [10.1016/j.actamat.2010.07.049](https://doi.org/10.1016/j.actamat.2010.07.049).
URL: <https://doi.org/10.1016/j.actamat.2010.07.049>.
- [11] J.-O. Andersson. In: Calphad 12.1 (Jan. 1988), pp. 1–8.
DOI: [10.1016/0364-5916\(88\)90024-7](https://doi.org/10.1016/0364-5916(88)90024-7).
URL: [https://doi.org/10.1016/0364-5916\(88\)90024-7](https://doi.org/10.1016/0364-5916(88)90024-7).

- [12] J.-O. Andersson et al. In: *Calphad* 26.2 (June 2002), pp. 273–312.
DOI: [10.1016/s0364-5916\(02\)00037-8](https://doi.org/10.1016/s0364-5916(02)00037-8).
URL: [https://doi.org/10.1016/s0364-5916\(02\)00037-8](https://doi.org/10.1016/s0364-5916(02)00037-8).
- [13] A. K. Arzhnikov, L. V. Dobysheva, and C. Demangeat.
In: *Journal of Physics: Condensed Matter* 19.19 (2007), p. 196214.
DOI: [10.1088/0953-8984/19/19/196214](https://doi.org/10.1088/0953-8984/19/19/196214).
URL: <https://doi.org/10.10882F0953-89842F192F192F196214>.
- [14] S. S. Babu, K. Hono, and T. Sakurai.
In: *Applied Surface Science* 67.1-4 (Apr. 1993), pp. 321–327.
DOI: [10.1016/0169-4332\(93\)90333-7](https://doi.org/10.1016/0169-4332(93)90333-7).
URL: [https://doi.org/10.1016/0169-4332\(93\)90333-7](https://doi.org/10.1016/0169-4332(93)90333-7).
- [15] S. S. Babu, K. Hono, and T. Sakurai.
In: *Metallurgical and Materials Transactions A* 25.3 (Mar. 1994), pp. 499–508.
DOI: [10.1007/bf02651591](https://doi.org/10.1007/bf02651591). URL: <https://doi.org/10.1007/bf02651591>.
- [16] A. Bakaev et al.
In: *Journal of Nuclear Materials* 444.1-3 (Jan. 2014), pp. 237–246.
DOI: [10.1016/j.jnucmat.2013.09.053](https://doi.org/10.1016/j.jnucmat.2013.09.053).
URL: <https://doi.org/10.1016/j.jnucmat.2013.09.053>.
- [17] O. Barbour et al. In: *Journal of Nuclear Materials* 539 (Oct. 2020), p. 152333.
DOI: [10.1016/j.jnucmat.2020.152333](https://doi.org/10.1016/j.jnucmat.2020.152333).
URL: <https://doi.org/10.1016/j.jnucmat.2020.152333>.
- [18] C. Barouh et al. In: *Physical Review B* 90.5 (Aug. 2014).
DOI: [10.1103/physrevb.90.054112](https://doi.org/10.1103/physrevb.90.054112).
URL: <https://doi.org/10.1103/physrevb.90.054112>.
- [19] C. Barouh et al. In: *Physical Review B* 92.10 (Sept. 2015).
DOI: [10.1103/physrevb.92.104102](https://doi.org/10.1103/physrevb.92.104102).
URL: <https://doi.org/10.1103/physrevb.92.104102>.
- [20] A. Benarosch. In: *Private communication, CEA* (2020).
- [21] F. M. Beremin. In: *Metallurgical Transactions A* 12.5 (1981), pp. 723–731.
- [22] V. A. Bišs and T. Wada.
In: *Metallurgical Transactions A* 16.1 (1985), pp. 109–114.
- [23] P. E. Blöchl. In: *Physical Review B* 50.24 (Dec. 1994), pp. 17953–17979.
ISSN: 0163-1829. DOI: [10.1103/PhysRevB.50.17953](https://doi.org/10.1103/PhysRevB.50.17953).
URL: <https://link.aps.org/doi/10.1103/PhysRevB.50.17953>.
- [24] P. Bocquet, D. Buisine, and L. Dunand-Roux.
In: *Revue de Métallurgie* 90.9 (1993), pp. 1088–1088.
- [25] J. Bouchard. In: *Annales de Chimie*. Vol. 2. 1967, pp. 353–366.
- [26] O. Buggenhoudt et al.
In: *Physical Review Materials* 5 (6 June 2021), p. 063401.
DOI: [10.1103/PhysRevMaterials.5.063401](https://doi.org/10.1103/PhysRevMaterials.5.063401).
URL: <https://link.aps.org/doi/10.1103/PhysRevMaterials.5.063401>.
- [27] J. Chance and N. Ridley.
In: *Metallurgical Transactions A* 12.7 (July 1981), pp. 1205–1213.
DOI: [10.1007/bf02642334](https://doi.org/10.1007/bf02642334). URL: <https://doi.org/10.1007/bf02642334>.
- [28] W Chiou. In: *Surface Science* 530.1-2 (Apr. 2003), pp. 88–100.
DOI: [10.1016/s0039-6028\(03\)00352-2](https://doi.org/10.1016/s0039-6028(03)00352-2).
URL: [https://doi.org/10.1016/s0039-6028\(03\)00352-2](https://doi.org/10.1016/s0039-6028(03)00352-2).

- [29] H.-J. Choe et al.
In: *Journal of Magnetism and Magnetic Materials* 417 (Nov. 2016), pp. 1–5.
DOI: [10.1016/j.jmmm.2016.05.008](https://doi.org/10.1016/j.jmmm.2016.05.008).
URL: <https://doi.org/10.1016/j.jmmm.2016.05.008>.
- [30] XY. Chong et al.
In: *Computational Materials Science* 87 (May 2014), pp. 19–25.
DOI: [10.1016/j.commatsci.2014.01.054](https://doi.org/10.1016/j.commatsci.2014.01.054).
URL: <https://doi.org/10.1016/j.commatsci.2014.01.054>.
- [31] A. N. Christensen. In: *Acta Chem. Scand., Ser. A* 31 (1977), 509–511.
- [32] E. V. Clougherty, K. H. Lothrop, and J. A. Kafalas.
In: *Nature* 191.4794 (Sept. 1961), pp. 1194–1194. DOI: [10.1038/1911194a0](https://doi.org/10.1038/1911194a0).
URL: <https://doi.org/10.1038/1911194a0>.
- [33] M. F. Collins and G. G. Low.
In: *Proceedings of the Physical Society* 86.3 (1965), pp. 535–548.
DOI: [10.1088/0370-1328/86/3/313](https://doi.org/10.1088/0370-1328/86/3/313).
URL: <https://doi.org/10.1088/0370-1328/86/3/313>.
- [34] E. A. Devi, R. Chinnappan, and C. S. Sundar.
In: *Physical Review B* 98.14 (Oct. 2018). DOI: [10.1103/physrevb.98.144104](https://doi.org/10.1103/physrevb.98.144104).
URL: <https://doi.org/10.1103/physrevb.98.144104>.
- [35] A. Dick et al. In: *Physical Review B* 84.12 (Sept. 2011).
DOI: [10.1103/physrevb.84.125101](https://doi.org/10.1103/physrevb.84.125101).
URL: <https://doi.org/10.1103/physrevb.84.125101>.
- [36] P. A. M. Dirac.
In: *Mathematical Proceedings of the Cambridge Philosophical Society* 26.3 (1930), 376–385. DOI: [10.1017/S0305004100016108](https://doi.org/10.1017/S0305004100016108).
- [37] S. P. Dodd et al. In: *Physica Status Solidi (a)* 198.2 (Aug. 2003), pp. 272–281.
DOI: [10.1002/pssa.200306613](https://doi.org/10.1002/pssa.200306613).
URL: <https://doi.org/10.1002/pssa.200306613>.
- [38] C. Domain, C. S. Becquart, and J. Foct.
In: *Physical Review B* 69.14 (Apr. 2004). DOI: [10.1103/physrevb.69.144112](https://doi.org/10.1103/physrevb.69.144112).
URL: <https://doi.org/10.1103/physrevb.69.144112>.
- [39] L. T. Domasevich et al. In: *Inorg. Matter* 13 (1977), p. 1733.
- [40] D. J. Dyson and K. W. Andrews.
In: *Journal of the Iron and Steel Institute* 202.4 (1964), p. 325.
- [41] T. Epicier et al. In: *Acta Metallurgica* 36.8 (Aug. 1988), pp. 1903–1921.
DOI: [10.1016/0001-6160\(88\)90293-3](https://doi.org/10.1016/0001-6160(88)90293-3).
URL: [https://doi.org/10.1016/0001-6160\(88\)90293-3](https://doi.org/10.1016/0001-6160(88)90293-3).
- [42] P. Eyméoud and P. Maugis.
In: *Journal of Magnetism and Magnetic Materials* 513 (Nov. 2020), p. 167223.
DOI: [10.1016/j.jmmm.2020.167223](https://doi.org/10.1016/j.jmmm.2020.167223).
URL: <https://doi.org/10.1016/j.jmmm.2020.167223>.
- [43] H. I. Faraoun et al. In: *Journal of Applied Physics* 99.9 (May 2006), p. 093508.
DOI: [10.1063/1.2194118](https://doi.org/10.1063/1.2194118). URL: <https://doi.org/10.1063/1.2194118>.
- [44] E. J. Fasiska and G. A. Jeffrey.
In: *Acta Crystallographica* 19.3 (Sept. 1965), pp. 463–471.
DOI: [10.1107/s0365110x65003602](https://doi.org/10.1107/s0365110x65003602).
URL: <https://doi.org/10.1107/s0365110x65003602>.

- [45] A. Fillon et al. In: *Scripta Materialia* 95 (Jan. 2015), pp. 35–38.
DOI: [10.1016/j.scriptamat.2014.09.025](https://doi.org/10.1016/j.scriptamat.2014.09.025).
URL: <https://doi.org/10.1016/j.scriptamat.2014.09.025>.
- [46] C. J. Först et al. In: *Physical Review Letters* 96.17 (May 2006).
DOI: [10.1103/physrevlett.96.175501](https://doi.org/10.1103/physrevlett.96.175501).
URL: <https://doi.org/10.1103/physrevlett.96.175501>.
- [47] D. Fruchart et al.
In: *Journal of Solid State Chemistry* 51.2 (Feb. 1984), pp. 246–252.
DOI: [10.1016/0022-4596\(84\)90340-2](https://doi.org/10.1016/0022-4596(84)90340-2).
URL: [https://doi.org/10.1016/0022-4596\(84\)90340-2](https://doi.org/10.1016/0022-4596(84)90340-2).
- [48] C.C. Fu et al. In: *Solid State Phenomena* 139 (Apr. 2008), pp. 157–164.
DOI: [10.4028/www.scientific.net/ssp.139.157](https://doi.org/10.4028/www.scientific.net/ssp.139.157).
URL: <https://doi.org/10.4028/www.scientific.net/ssp.139.157>.
- [49] C.C. Fu et al. In: *Physical Review B* 91.9 (Mar. 2015).
DOI: [10.1103/physrevb.91.094430](https://doi.org/10.1103/physrevb.91.094430).
URL: <https://doi.org/10.1103/physrevb.91.094430>.
- [50] T. Furuhashi, K. Kobayashi, and T. Maki.
In: *ISIJ International* 44.11 (2004), pp. 1937–1944.
DOI: [10.2355/isijinternational.44.1937](https://doi.org/10.2355/isijinternational.44.1937).
URL: <https://doi.org/10.2355/isijinternational.44.1937>.
- [51] Y. Gao et al. In: *Materials Letters* 100 (June 2013), pp. 170–172.
DOI: [10.1016/j.matlet.2013.02.095](https://doi.org/10.1016/j.matlet.2013.02.095).
URL: <https://doi.org/10.1016/j.matlet.2013.02.095>.
- [52] D. Gendt. Theses. Université Paris Saclay, 2001.
URL: <http://www.theses.fr/2001PA112131>.
- [53] H. J. Goldschmidt. In: *J. Iron Steel Inst* 160 (1948), p. 345.
- [54] O. I. Gorbatov et al.
In: *Journal of Nuclear Materials* 475 (July 2016), pp. 140–148.
DOI: [10.1016/j.jnucmat.2016.04.013](https://doi.org/10.1016/j.jnucmat.2016.04.013).
URL: <https://doi.org/10.1016/j.jnucmat.2016.04.013>.
- [55] M. Guziowski, S. P. Coleman, and C. R. Weinberger.
In: *Acta Materialia* 119 (Oct. 2016), pp. 184–192.
DOI: [10.1016/j.actamat.2016.08.017](https://doi.org/10.1016/j.actamat.2016.08.017).
URL: <https://doi.org/10.1016/j.actamat.2016.08.017>.
- [56] M. Guziowski, S. P. Coleman, and C. R. Weinberger.
In: *Acta Materialia* 144 (Feb. 2018), pp. 656–665.
DOI: [10.1016/j.actamat.2017.10.070](https://doi.org/10.1016/j.actamat.2017.10.070).
URL: <https://doi.org/10.1016/j.actamat.2017.10.070>.
- [57] R. Hafner et al. In: *Physical Review B* 65 (18 May 2002), p. 184432.
DOI: [10.1103/PhysRevB.65.184432](https://doi.org/10.1103/PhysRevB.65.184432).
URL: <https://link.aps.org/doi/10.1103/PhysRevB.65.184432>.
- [58] J. Häglund, G. Grimvall, and T. Jarlborg.
In: *Physical Review B* 44.7 (Aug. 1991), pp. 2914–2919.
DOI: [10.1103/physrevb.44.2914](https://doi.org/10.1103/physrevb.44.2914).
URL: <https://doi.org/10.1103/physrevb.44.2914>.

- [59] J. Haines et al.
In: *Journal of Physics: Condensed Matter* 13.11 (Mar. 2001), pp. 2447–2454.
DOI: [10.1088/0953-8984/13/11/303](https://doi.org/10.1088/0953-8984/13/11/303).
URL: <https://doi.org/10.1088/0953-8984/13/11/303>.
- [60] B. Hallstedt et al. In: *Calphad* 34.1 (Mar. 2010), pp. 129–133.
DOI: [10.1016/j.calphad.2010.01.004](https://doi.org/10.1016/j.calphad.2010.01.004).
URL: <https://doi.org/10.1016/j.calphad.2010.01.004>.
- [61] G. Henkelman, B. P. Uberuaga, and H. Jónsson.
In: *The Journal of Chemical Physics* 113.22 (Dec. 2000), pp. 9901–9904.
DOI: [10.1063/1.1329672](https://doi.org/10.1063/1.1329672). URL: <https://doi.org/10.1063/1.1329672>.
- [62] K. O. E. Henriksson, N. Sandberg, and J. Wallenius.
In: *Applied Physics Letters* 93.19 (Nov. 2008), p. 191912.
DOI: [10.1063/1.3026175](https://doi.org/10.1063/1.3026175). URL: <https://doi.org/10.1063/1.3026175>.
- [63] F. H. Herbstein and J. Smuts.
In: *Acta Crystallographica* 17.10 (Oct. 1964), pp. 1331–1332.
DOI: [10.1107/s0365110x64003346](https://doi.org/10.1107/s0365110x64003346).
URL: <https://doi.org/10.1107/s0365110x64003346>.
- [64] H. C. Herper, E. Hoffmann, and P. Entel.
In: *Physical Review B* 60 (6 1999), pp. 3839–3848.
DOI: [10.1103/PhysRevB.60.3839](https://doi.org/10.1103/PhysRevB.60.3839).
URL: <https://link.aps.org/doi/10.1103/PhysRevB.60.3839>.
- [65] R. Herschberg et al. In: *Acta Materialia* 165 (Feb. 2019), pp. 638–653.
DOI: [10.1016/j.actamat.2018.11.025](https://doi.org/10.1016/j.actamat.2018.11.025).
URL: <https://doi.org/10.1016/j.actamat.2018.11.025>.
- [66] M. Hillert and M. D. Sharp. In: *Jernkontorets Ann.* 137 (1953), p. 785.
- [67] C. Hin et al. In: *Acta Materialia* 56.19 (2008), pp. 5535–5543.
- [68] L. J. E. Hofer and E. M. Cohn. In: *Journal of the American Chemical Society* 81.7 (Apr. 1959), pp. 1576–1582. DOI: [10.1021/ja01516a016](https://doi.org/10.1021/ja01516a016).
URL: <https://doi.org/10.1021/ja01516a016>.
- [69] P. Hohenberg and W. Kohn.
In: *Physical Review* 136 (3B Nov. 1964), B864–B871.
DOI: [10.1103/PhysRev.136.B864](https://doi.org/10.1103/PhysRev.136.B864).
URL: <https://link.aps.org/doi/10.1103/PhysRev.136.B864>.
- [70] L. Huang et al. In: *Physica Status Solidi (b)* 253.8 (Apr. 2016), pp. 1623–1628.
DOI: [10.1002/pssb.201552675](https://doi.org/10.1002/pssb.201552675).
URL: <https://doi.org/10.1002/pssb.201552675>.
- [71] H. W. Hugosson et al. In: *Physical Review B* 63.13 (Mar. 2001).
DOI: [10.1103/physrevb.63.134108](https://doi.org/10.1103/physrevb.63.134108).
URL: <https://doi.org/10.1103/physrevb.63.134108>.
- [72] Y. Iijima.
In: *Journal of Alloys and Compounds* 234.2 (Feb. 1996), pp. 290–294.
DOI: [10.1016/0925-8388\(95\)02104-3](https://doi.org/10.1016/0925-8388(95)02104-3).
URL: [https://doi.org/10.1016/0925-8388\(95\)02104-3](https://doi.org/10.1016/0925-8388(95)02104-3).
- [73] Y.-R. Im et al. In: *Journal of nuclear materials* 297.2 (2001), pp. 138–148.
- [74] A. Inoue and T. Masumoto. In: 13.8 (Aug. 1979), pp. 711–715.
DOI: [10.1016/0036-9748\(79\)90142-x](https://doi.org/10.1016/0036-9748(79)90142-x).
URL: [https://doi.org/10.1016/0036-9748\(79\)90142-x](https://doi.org/10.1016/0036-9748(79)90142-x).

- [75] K. J. Irvine and F. B. Pickering.
In: Journal of the Iron and Steel Institute 194 (1960), pp. 137–153.
- [76] J. H. Jang, I. G. Kim, and H. K. D. H. Bhadeshia.
In: Materials Science Forum 638–642 (Jan. 2010), pp. 3319–3324.
DOI: [10.4028/www.scientific.net/msf.638-642.3319](https://doi.org/10.4028/www.scientific.net/msf.638-642.3319).
URL: <https://doi.org/10.4028/www.scientific.net/msf.638-642.3319>.
- [77] S.-H. Jhi et al. In: Physical Review Letters 86.15 (Apr. 2001), pp. 3348–3351.
DOI: [10.1103/physrevlett.86.3348](https://doi.org/10.1103/physrevlett.86.3348).
URL: <https://doi.org/10.1103/physrevlett.86.3348>.
- [78] C. Jiang. In: Applied Physics Letters 92.4 (Jan. 2008), p. 041909.
DOI: [10.1063/1.2838345](https://doi.org/10.1063/1.2838345). URL: <https://doi.org/10.1063/1.2838345>.
- [79] C. Jiang, B. P. Uberuaga, and S. G. Srinivasan.
In: Acta Materialia 56.13 (Aug. 2008), pp. 3236–3244.
DOI: [10.1016/j.actamat.2008.03.012](https://doi.org/10.1016/j.actamat.2008.03.012).
URL: <https://doi.org/10.1016/j.actamat.2008.03.012>.
- [80] C. Jiang et al. In: Journal of Applied Physics 103.4 (Feb. 2008), p. 043502.
DOI: [10.1063/1.2884529](https://doi.org/10.1063/1.2884529). URL: <https://doi.org/10.1063/1.2884529>.
- [81] D. E. Jiang and E. A. Carter. In: Physical Review B 67.21 (June 2003).
DOI: [10.1103/physrevb.67.214103](https://doi.org/10.1103/physrevb.67.214103).
URL: <https://doi.org/10.1103/physrevb.67.214103>.
- [82] H. Jónsson, G. Mills, and K. W. Jacobsen. In:
Classical and Quantum Dynamics in Condensed Phase Simulations.
Ed. by World Scientific. June 1998. DOI: [10.1142/9789812839664_0016](https://doi.org/10.1142/9789812839664_0016).
URL: https://doi.org/10.1142/9789812839664_0016.
- [83] A. Kagawa and T. Okamoto.
In: Transactions of the Japan Institute of Metals 20.11 (1979), pp. 659–666.
DOI: [10.2320/matertrans1960.20.659](https://doi.org/10.2320/matertrans1960.20.659).
URL: <https://doi.org/10.2320/matertrans1960.20.659>.
- [84] E. Karaca et al.
In: Journal of Alloys and Compounds 788 (June 2019), pp. 842–851.
DOI: [10.1016/j.jallcom.2019.02.243](https://doi.org/10.1016/j.jallcom.2019.02.243).
URL: <https://doi.org/10.1016/j.jallcom.2019.02.243>.
- [85] P. Karen et al. In: Acta Chemica Scandinavica 45 (1991), pp. 549–557.
- [86] L. Kaufman and H. Bernstein. Ed. by United States: Academic Press Inc.
1970.
- [87] K. Kawakami and T. Matsumiya.
In: ISIJ International 53.4 (2013), pp. 709–713.
DOI: [10.2355/isijinternational.53.709](https://doi.org/10.2355/isijinternational.53.709).
URL: <https://doi.org/10.2355/isijinternational.53.709>.
- [88] F. X. Kayser and Y. Sumitomo.
In: Journal of Phase Equilibria 18.5 (Sept. 1997), pp. 458–464.
DOI: [10.1007/bf02647702](https://doi.org/10.1007/bf02647702). URL: <https://doi.org/10.1007/bf02647702>.
- [89] J. Kim, K. Kang, and S. Ryu.
In: International Journal of Plasticity 83 (Aug. 2016), pp. 302–312.
DOI: [10.1016/j.ijplas.2016.04.016](https://doi.org/10.1016/j.ijplas.2016.04.016).
URL: <https://doi.org/10.1016/j.ijplas.2016.04.016>.

- [90] D. J. M. King et al. In: *Physical Review B* 98.2 (July 2018), p. 024418.
DOI: [10.1103/physrevb.98.024418](https://doi.org/10.1103/physrevb.98.024418).
URL: <https://doi.org/10.1103/physrevb.98.024418>.
- [91] C. Kittel and P. McEuen. In: *Introduction to solid state physics*. Vol. 8. Wiley New York, 1996.
- [92] T. P. C. Klaver, R. Drautz, and M. W. Finnis.
In: *Physical Review B* 74.9 (Sept. 2006). DOI: [10.1103/physrevb.74.094435](https://doi.org/10.1103/physrevb.74.094435).
URL: <https://doi.org/10.1103/physrevb.74.094435>.
- [93] M. Ko, T. Sakuma, and T. Nishizawa.
In: *Journal of the Japan Institute of Metals* 40.6 (1976), pp. 593–601.
DOI: [10.2320/jinstmet1952.40.6_593](https://doi.org/10.2320/jinstmet1952.40.6_593).
URL: https://doi.org/10.2320/jinstmet1952.40.6_593.
- [94] W. Kohn and L. J. Sham.
In: *Physical Review* 140 (4A Nov. 1965), A1133–A1138.
DOI: [10.1103/PhysRev.140.A1133](https://doi.org/10.1103/PhysRev.140.A1133).
URL: <https://link.aps.org/doi/10.1103/PhysRev.140.A1133>.
- [95] M. A. Konyaeva and N. I. Medvedeva.
In: *Physics of the Solid State* 51.10 (Oct. 2009), pp. 2084–2089.
DOI: [10.1134/s1063783409100151](https://doi.org/10.1134/s1063783409100151).
URL: <https://doi.org/10.1134/s1063783409100151>.
- [96] G. Kresse and J. Furthmüller.
In: *Comput. Mater. Sci.* 6.1 (July 1996), pp. 15–50. ISSN: 09270256.
DOI: [10.1016/0927-0256\(96\)00008-0](https://doi.org/10.1016/0927-0256(96)00008-0).
URL: <http://linkinghub.elsevier.com/retrieve/pii/0927025696000080>.
- [97] G. Kresse and J. Furthmüller.
In: *Physical Review B* 54.16 (Oct. 1996), pp. 11169–11186. ISSN: 0163-1829.
DOI: [10.1103/PhysRevB.54.11169](https://doi.org/10.1103/PhysRevB.54.11169).
URL: <https://link.aps.org/doi/10.1103/PhysRevB.54.11169>.
- [98] G. Kresse and J. Hafner. In: *Physical Review B* 47.1 (Jan. 1993), pp. 558–561.
ISSN: 0163-1829. DOI: [10.1103/PhysRevB.47.558](https://doi.org/10.1103/PhysRevB.47.558).
URL: <https://link.aps.org/doi/10.1103/PhysRevB.47.558>.
- [99] K. Kuo. In: *Acta metallurgica* 1.3 (1953), pp. 301–304.
- [100] K. Kuo and L. E. Persson.
In: *Journal of the Iron and Steel Institute* 178.1 (1954), pp. 39–44.
- [101] Landolt-Börnstein. In: *Diffusion in Solid Metals and Alloys*.
Ed. by H. Mehrer. Springer-Verlag, 1990. DOI: [10.1007/b37801](https://doi.org/10.1007/b37801).
URL: <https://doi.org/10.1007/b37801>.
- [102] A. Leineweber, S. L. Shang, and Z. K. Liu.
In: *Acta Materialia* 86 (Mar. 2015), pp. 374–384.
DOI: [10.1016/j.actamat.2014.11.046](https://doi.org/10.1016/j.actamat.2014.11.046).
URL: <https://doi.org/10.1016/j.actamat.2014.11.046>.
- [103] K. Lejaeghere et al. In: *Physical Review B* 83.18 (May 2011).
DOI: [10.1103/physrevb.83.184201](https://doi.org/10.1103/physrevb.83.184201).
URL: <https://doi.org/10.1103/physrevb.83.184201>.
- [104] E. Levchenko et al. In: *Acta Materialia* 57.3 (Feb. 2009), pp. 846–853.
DOI: [10.1016/j.actamat.2008.10.025](https://doi.org/10.1016/j.actamat.2008.10.025).
URL: <https://doi.org/10.1016/j.actamat.2008.10.025>.

- [105] M. Levesque et al. In: Physical Review B 84.18 (Nov. 2011).
DOI: [10.1103/physrevb.84.184205](https://doi.org/10.1103/physrevb.84.184205).
URL: <https://doi.org/10.1103/physrevb.84.184205>.
- [106] J. Li et al.
In: Physics and Chemistry of Minerals 29.3 (Apr. 2002), pp. 166–169.
DOI: [10.1007/s00269-001-0224-4](https://doi.org/10.1007/s00269-001-0224-4).
URL: <https://doi.org/10.1007/s00269-001-0224-4>.
- [107] Y. Li et al.
In: Journal of Alloys and Compounds 509.17 (Apr. 2011), pp. 5242–5249.
DOI: [10.1016/j.jallcom.2011.02.009](https://doi.org/10.1016/j.jallcom.2011.02.009).
URL: <https://doi.org/10.1016/j.jallcom.2011.02.009>.
- [108] H. Lipson and N. J. Petch. In: J. Iron Steel Inst., London 142.95 (1940).
- [109] J. Lis, J. Morgiel, and A. Lis.
In: Materials Chemistry and Physics 81.2-3 (Aug. 2003), pp. 466–468.
DOI: [10.1016/s0254-0584\(03\)00053-1](https://doi.org/10.1016/s0254-0584(03)00053-1).
URL: [https://doi.org/10.1016/s0254-0584\(03\)00053-1](https://doi.org/10.1016/s0254-0584(03)00053-1).
- [110] H. Liu et al. In: Scripta Materialia 60.11 (June 2009), pp. 949–952.
DOI: [10.1016/j.scriptamat.2009.02.010](https://doi.org/10.1016/j.scriptamat.2009.02.010).
URL: <https://doi.org/10.1016/j.scriptamat.2009.02.010>.
- [111] P. Liu et al. In: Physical Review B 90.2 (July 2014).
DOI: [10.1103/physrevb.90.024103](https://doi.org/10.1103/physrevb.90.024103).
URL: <https://doi.org/10.1103/physrevb.90.024103>.
- [112] YZ. Liu et al. In: Ceramics International 41.4 (May 2015), pp. 5239–5246.
DOI: [10.1016/j.ceramint.2014.10.167](https://doi.org/10.1016/j.ceramint.2014.10.167).
URL: <https://doi.org/10.1016/j.ceramint.2014.10.167>.
- [113] ZI-K. Liu et al.
In: Metallurgical Transactions A 22.8 (Aug. 1991), pp. 1745–1752.
DOI: [10.1007/bf02646498](https://doi.org/10.1007/bf02646498). URL: <https://doi.org/10.1007/bf02646498>.
- [114] A. E. Lord and D. N. Beshers.
In: Acta Metallurgica 14.12 (Dec. 1966), pp. 1659–1672.
DOI: [10.1016/0001-6160\(66\)90018-6](https://doi.org/10.1016/0001-6160(66)90018-6).
URL: [https://doi.org/10.1016/0001-6160\(66\)90018-6](https://doi.org/10.1016/0001-6160(66)90018-6).
- [115] H. Lux and A. Ignatowicz. In: Chem. Ber. 101 (1968), p. 809.
- [116] Z. Q. Lv et al. In: Journal of Magnetism and Magnetic Materials 323.7 (Apr. 2011), pp. 915–919. DOI: [10.1016/j.jmmm.2010.11.067](https://doi.org/10.1016/j.jmmm.2010.11.067).
URL: <https://doi.org/10.1016/j.jmmm.2010.11.067>.
- [117] Z. Q. Lv et al.
In: Computational Materials Science 44.2 (Dec. 2008), pp. 690–694.
DOI: [10.1016/j.commatsci.2008.05.006](https://doi.org/10.1016/j.commatsci.2008.05.006).
URL: <https://doi.org/10.1016/j.commatsci.2008.05.006>.
- [118] V. Massardier et al. In: Metallurgical and Materials Transactions A 36.7 (July 2005), pp. 1745–1755. DOI: [10.1007/s11661-005-0039-x](https://doi.org/10.1007/s11661-005-0039-x).
URL: <https://doi.org/10.1007/s11661-005-0039-x>.
- [119] R. B. McLellan and M. L. Wasz.
In: Journal of Physics and Chemistry of Solids 54.5 (May 1993), pp. 583–586.
DOI: [10.1016/0022-3697\(93\)90236-k](https://doi.org/10.1016/0022-3697(93)90236-k).
URL: [https://doi.org/10.1016/0022-3697\(93\)90236-k](https://doi.org/10.1016/0022-3697(93)90236-k).

- [120] A. J. Medford et al. In: *Journal of Catalysis* 290 (June 2012), pp. 108–117.
DOI: [10.1016/j.jcat.2012.03.007](https://doi.org/10.1016/j.jcat.2012.03.007).
URL: <https://doi.org/10.1016/j.jcat.2012.03.007>.
- [121] N. I. Medvedeva, D. C. Van Aken, and J. E. Medvedeva.
In: *Journal of Physics: Condensed Matter* 23.32 (July 2011), p. 326003.
DOI: [10.1088/0953-8984/23/32/326003](https://doi.org/10.1088/0953-8984/23/32/326003).
URL: <https://doi.org/10.1088/0953-8984/23/32/326003>.
- [122] N. I. Medvedeva, L. E. Kar'kina, and A. L. Ivanovskii.
In: *Physics of the Solid State* 48.1 (Jan. 2006), pp. 15–19.
DOI: [10.1134/s1063783406010045](https://doi.org/10.1134/s1063783406010045).
URL: <https://doi.org/10.1134/s1063783406010045>.
- [123] N. I. Medvedeva et al.
In: *The Physics of Metals and Metallography* 105.6 (June 2008), pp. 568–573.
DOI: [10.1134/s0031918x08060069](https://doi.org/10.1134/s0031918x08060069).
URL: <https://doi.org/10.1134/s0031918x08060069>.
- [124] D. Meinhardt and O. Krisement. In: *Arch. Eisenhuettenw.* 33 (July 1962).
URL: <https://www.osti.gov/biblio/4672679>.
- [125] S. V. Meschel and O. J. Kleppa.
In: *Journal of Alloys and Compounds* 257.1 (1997), pp. 227–233.
DOI: [https://doi.org/10.1016/S0925-8388\(97\)00023-6](https://doi.org/10.1016/S0925-8388(97)00023-6). URL: <https://www.sciencedirect.com/science/article/pii/S0925838897000236>.
- [126] L. Messina et al. In: *Acta Materialia* 191 (June 2020), pp. 166–185.
DOI: [10.1016/j.actamat.2020.03.038](https://doi.org/10.1016/j.actamat.2020.03.038).
URL: <https://doi.org/10.1016/j.actamat.2020.03.038>.
- [127] M. K. Miller and G. D. W. Smith.
In: *Metal Science* 11.7 (July 1977), pp. 249–253.
DOI: [10.1179/msc.1977.11.7.249](https://doi.org/10.1179/msc.1977.11.7.249).
URL: <https://doi.org/10.1179/msc.1977.11.7.249>.
- [128] A. A. Mirzoev, M. M. Yalalov, and D. A. Mirzaev.
In: *The Physics of Metals and Metallography* 101.4 (Apr. 2006), pp. 341–348.
DOI: [10.1134/s0031918x06040065](https://doi.org/10.1134/s0031918x06040065).
URL: <https://doi.org/10.1134/s0031918x06040065>.
- [129] G. Miyamoto et al. In: *Acta Materialia* 55.15 (Sept. 2007), pp. 5027–5038.
DOI: [10.1016/j.actamat.2007.05.023](https://doi.org/10.1016/j.actamat.2007.05.023).
URL: <https://doi.org/10.1016/j.actamat.2007.05.023>.
- [130] H. J. Monkhorst and J. D. Pack.
In: *Physical Review B* 13.12 (June 1976), pp. 5188–5192. ISSN: 0556-2805.
DOI: [10.1103/PhysRevB.13.5188](https://doi.org/10.1103/PhysRevB.13.5188).
URL: <https://link.aps.org/doi/10.1103/PhysRevB.13.5188>.
- [131] J. P. Morniroli and M. Gantois.
In: *Journal of Applied Crystallography* 16.1 (1983), pp. 1–10.
- [132] M. Nastar, V. Y. Dobretsov, and G. Martin. In: *Phil. Mag. A* 80 (2000), p. 155.
DOI: <https://doi.org/10.1080/01418610008212047>. URL: <https://www.tandfonline.com/doi/abs/10.1080/01418610008212047>.
- [133] M. Nikolussi et al. In: *Scripta Materialia* 59.8 (Oct. 2008), pp. 814–817.
DOI: [10.1016/j.scriptamat.2008.06.015](https://doi.org/10.1016/j.scriptamat.2008.06.015).
URL: <https://doi.org/10.1016/j.scriptamat.2008.06.015>.

- [134] D. Odkhuu et al.
In: Journal of the Korean Physical Society 69.8 (Oct. 2016), pp. 1335–1340.
DOI: [10.3938/jkps.69.1335](https://doi.org/10.3938/jkps.69.1335).
URL: <https://doi.org/10.3938/jkps.69.1335>.
- [135] C. de Oliveira et al.
In: The Journal of Physical Chemistry C 118.44 (Oct. 2014), pp. 25517–25524.
DOI: [10.1021/jp507947b](https://doi.org/10.1021/jp507947b). URL: <https://doi.org/10.1021/jp507947b>.
- [136] P. Olsson, C. Domain, and J. Wallenius.
In: Physical Review B 75.1 (Jan. 2007). DOI: [10.1103/physrevb.75.014110](https://doi.org/10.1103/physrevb.75.014110).
URL: <https://doi.org/10.1103/physrevb.75.014110>.
- [137] P. Olsson, T. P. C. Klaver, and C. Domain.
In: Physical Review B 81.5 (Feb. 2010). DOI: [10.1103/physrevb.81.054102](https://doi.org/10.1103/physrevb.81.054102).
URL: <https://doi.org/10.1103/physrevb.81.054102>.
- [138] L. Onsager. In: Physical Review 37 (4 Feb. 1931), pp. 405–426.
DOI: [10.1103/PhysRev.37.405](https://doi.org/10.1103/PhysRev.37.405).
URL: <https://link.aps.org/doi/10.1103/PhysRev.37.405>.
- [139] S. Otani and Y. Ishizawa.
In: Journal of Crystal Growth 154.1-2 (Sept. 1995), pp. 202–204.
DOI: [10.1016/0022-0248\(95\)00243-x](https://doi.org/10.1016/0022-0248(95)00243-x).
URL: [https://doi.org/10.1016/0022-0248\(95\)00243-x](https://doi.org/10.1016/0022-0248(95)00243-x).
- [140] B. Ozturk et al.
In: Metallurgical Transactions A 13.10 (Oct. 1982), pp. 1871–1873.
DOI: [10.1007/bf02647845](https://doi.org/10.1007/bf02647845). URL: <https://doi.org/10.1007/bf02647845>.
- [141] B. Ozturk et al. In: Solid State Ionics 12 (Mar. 1984), pp. 145–151.
DOI: [10.1016/0167-2738\(84\)90141-3](https://doi.org/10.1016/0167-2738(84)90141-3).
URL: [https://doi.org/10.1016/0167-2738\(84\)90141-3](https://doi.org/10.1016/0167-2738(84)90141-3).
- [142] D. E. Parsons, T. F. Malis, and J. D. Boyd.
In: Journal of Heat Treating 3.3 (June 1984), pp. 213–219.
DOI: [10.1007/bf02833263](https://doi.org/10.1007/bf02833263). URL: <https://doi.org/10.1007/bf02833263>.
- [143] E. Parthé and V. Sadogopan.
In: Acta Crystallographica 16.3 (Mar. 1963), pp. 202–205.
DOI: [10.1107/s0365110x63000487](https://doi.org/10.1107/s0365110x63000487).
URL: <https://doi.org/10.1107/s0365110x63000487>.
- [144] W. Pascheto and G. P. Johari. In: Metallurgical and Materials Transactions A 27.9 (Sept. 1996), pp. 2461–2469. DOI: [10.1007/bf02652340](https://doi.org/10.1007/bf02652340).
URL: <https://doi.org/10.1007/bf02652340>.
- [145] J. P. Perdew, K. Burke, and M. Ernzerhof.
In: Physical Review Letters 77.18 (Oct. 1996), pp. 3865–3868.
DOI: [10.1103/PhysRevLett.77.3865](https://doi.org/10.1103/PhysRevLett.77.3865).
URL: <https://link.aps.org/doi/10.1103/PhysRevLett.77.3865>.
- [146] M. Perez and A. Deschamps.
In: Materials Science and Engineering: A 360.1 (Nov. 2003), pp. 214–219.
DOI: [10.1016/s0921-5093\(03\)00431-3](https://doi.org/10.1016/s0921-5093(03)00431-3).
URL: [https://doi.org/10.1016/s0921-5093\(03\)00431-3](https://doi.org/10.1016/s0921-5093(03)00431-3).

- [147] C. Philippot et al.
In: Computational Materials Science 106 (Aug. 2015), pp. 64–68.
DOI: [10.1016/j.commatsci.2015.04.020](https://doi.org/10.1016/j.commatsci.2015.04.020).
URL: <https://doi.org/10.1016/j.commatsci.2015.04.020>.
- [148] C. Pistonesi et al. In: Surface Science 602.13 (July 2008), pp. 2206–2211.
DOI: [10.1016/j.susc.2008.04.039](https://doi.org/10.1016/j.susc.2008.04.039).
URL: <https://doi.org/10.1016/j.susc.2008.04.039>.
- [149] G. Rahman et al. In: Physical Review B 81.18 (May 2010), p. 184423.
DOI: [10.1103/physrevb.81.184423](https://doi.org/10.1103/physrevb.81.184423).
URL: <https://doi.org/10.1103/physrevb.81.184423>.
- [150] V. B. Rajkumar and K. C. Hari Kumar.
In: Journal of Alloys and Compounds 611 (Oct. 2014), pp. 303–312.
DOI: [10.1016/j.jallcom.2014.05.030](https://doi.org/10.1016/j.jallcom.2014.05.030).
URL: <https://doi.org/10.1016/j.jallcom.2014.05.030>.
- [151] S. Raoul, B. Marini, and A. Pineau.
In: Journal of nuclear materials 257.2 (1998), pp. 199–205.
- [152] M. Rapposch et al. In: Monatshefte für Chemie/Chemical Monthly 116.11 (1985), pp. 1237–1245.
- [153] N. A. Razik et al.
In: Metallurgical Transactions A 7.2 (Feb. 1976), pp. 209–214.
DOI: [10.1007/bf02644458](https://doi.org/10.1007/bf02644458). URL: <https://doi.org/10.1007/bf02644458>.
- [154] V. I. Razumovskiy and G. Ghosh.
In: Computational Materials Science 110 (Dec. 2015), pp. 169–181.
DOI: [10.1016/j.commatsci.2015.08.006](https://doi.org/10.1016/j.commatsci.2015.08.006).
URL: <https://doi.org/10.1016/j.commatsci.2015.08.006>.
- [155] K. M. Reddy et al.
In: Journal of alloys and compounds 494.1-2 (2010), pp. 386–391.
- [156] J. Ren et al. In: Surface Science 596.1-3 (Dec. 2005), pp. 212–221.
DOI: [10.1016/j.susc.2005.09.018](https://doi.org/10.1016/j.susc.2005.09.018).
URL: <https://doi.org/10.1016/j.susc.2005.09.018>.
- [157] N. Ridley, M. A. Malik, and G. W. Lorimer.
In: Materials Characterization 25.1 (July 1990), pp. 125–141.
DOI: [10.1016/1044-5803\(90\)90025-f](https://doi.org/10.1016/1044-5803(90)90025-f).
URL: [https://doi.org/10.1016/1044-5803\(90\)90025-f](https://doi.org/10.1016/1044-5803(90)90025-f).
- [158] J. R. Rinebolt. In: Trans. Am. Soc. Met. 43 (1951), pp. 1175–1214.
- [159] M. Ruda, D. Farkas, and G. Garcia.
In: Computational Materials Science 45.2 (Apr. 2009), pp. 550–560.
DOI: [10.1016/j.commatsci.2008.11.020](https://doi.org/10.1016/j.commatsci.2008.11.020).
URL: <https://doi.org/10.1016/j.commatsci.2008.11.020>.
- [160] N. Sandberg, K. O. E. Henriksson, and J. Wallenius.
In: Physical Review B 78.9 (Sept. 2008). DOI: [10.1103/physrevb.78.094110](https://doi.org/10.1103/physrevb.78.094110).
URL: <https://doi.org/10.1103/physrevb.78.094110>.
- [161] J. R. dos Santos Politi et al.
In: Physical Chemistry Chemical Physics 15.30 (2013), p. 12617.
DOI: [10.1039/c3cp51389k](https://doi.org/10.1039/c3cp51389k). URL: <https://doi.org/10.1039/c3cp51389k>.

- [162] A. Schneider, C.C. Fu, and C. Barreteau.
In: *Physical Review B* 98.9 (Sept. 2018). DOI: [10.1103/physrevb.98.094426](https://doi.org/10.1103/physrevb.98.094426).
URL: <https://doi.org/10.1103/physrevb.98.094426>.
- [163] A. Schneider and G. Inden. In: *Calphad* 31.1 (Mar. 2007), pp. 141–147.
DOI: [10.1016/j.calphad.2006.07.008](https://doi.org/10.1016/j.calphad.2006.07.008).
URL: <https://doi.org/10.1016/j.calphad.2006.07.008>.
- [164] A. Schneider et al. In: *Physical Review B* 103.2 (Jan. 2021).
DOI: [10.1103/physrevb.103.024421](https://doi.org/10.1103/physrevb.103.024421).
URL: <https://doi.org/10.1103/physrevb.103.024421>.
- [165] A. Schneider et al. In: *Physical Review Letters* 124.21 (May 2020).
DOI: [10.1103/physrevlett.124.215901](https://doi.org/10.1103/physrevlett.124.215901).
URL: <https://doi.org/10.1103/physrevlett.124.215901>.
- [166] T. Schuler, L. Messina, and M. Nastar.
In: *Computational Materials Science* 170 (2019), p. 109191.
DOI: [10.1016.j.commatsci.2019.109191](https://doi.org/10.1016/j.commatsci.2019.109191).
URL: <https://doi.org/10.1016/j.commatsci.2019.109191>.
- [167] T. Schuler, L. Messina, and M. Nastar. 2019.
URL: <https://github.com/lukamessina/kineclue>.
- [168] T. Schuler, M. Nastar, and L. Messina.
In: *Physical Review Materials* 4 (2 Feb. 2020), p. 020401.
DOI: [10.1103/PhysRevMaterials.4.020401](https://doi.org/10.1103/PhysRevMaterials.4.020401).
URL: <https://link.aps.org/doi/10.1103/PhysRevMaterials.4.020401>.
- [169] T. Schuler et al. In: *Physical Review Letters* 115.1 (June 2015).
DOI: [10.1103/physrevlett.115.015501](https://doi.org/10.1103/physrevlett.115.015501).
URL: <https://doi.org/10.1103/physrevlett.115.015501>.
- [170] Thomas Schuler. Theses. Université Paris Sud - Paris XI, Sept. 2015.
URL: <https://tel.archives-ouvertes.fr/tel-01424176>.
- [171] I. R. Shein, N. I. Medvedeva, and A. L. Ivanovskii.
In: *Physica Status Solidi (b)* 244.6 (June 2007), pp. 1971–1981.
DOI: [10.1002/pssb.200642400](https://doi.org/10.1002/pssb.200642400).
URL: <https://doi.org/10.1002/pssb.200642400>.
- [172] M. G. Shelyapina et al.
In: *Journal of Alloys and Compounds* 383.1-2 (Nov. 2004), pp. 157–161.
DOI: [10.1016/j.jallcom.2004.04.036](https://doi.org/10.1016/j.jallcom.2004.04.036).
URL: <https://doi.org/10.1016/j.jallcom.2004.04.036>.
- [173] X.-R. Shi et al. In: *Surface Science* 603.6 (Mar. 2009), pp. 852–859.
DOI: [10.1016/j.susc.2009.01.041](https://doi.org/10.1016/j.susc.2009.01.041).
URL: <https://doi.org/10.1016/j.susc.2009.01.041>.
- [174] K. Shibanuma, S. Aihara, and S. Ohtsuka.
In: *ISIJ International* 54.7 (2014), pp. 1719–1728.
DOI: [10.2355/isijinternational.54.1719](https://doi.org/10.2355/isijinternational.54.1719).
URL: <https://doi.org/10.2355/isijinternational.54.1719>.
- [175] T. Shigematsu.
In: *Journal of the Physical Society of Japan* 39.4 (Oct. 1975), pp. 915–920.
DOI: [10.1143/jpsj.39.915](https://doi.org/10.1143/jpsj.39.915). URL: <https://doi.org/10.1143/jpsj.39.915>.

- [176] T. Shigematsu.
In: Journal of the Physical Society of Japan 37.4 (Oct. 1974), pp. 940–945.
DOI: [10.1143/jpsj.37.940](https://doi.org/10.1143/jpsj.37.940). URL: <https://doi.org/10.1143/jpsj.37.940>.
- [177] D. V. Shtansky and G. Inden.
In: Acta Materialia 45.7 (July 1997), pp. 2861–2878.
DOI: [10.1016/s1359-6454\(96\)00375-8](https://doi.org/10.1016/s1359-6454(96)00375-8).
URL: [https://doi.org/10.1016/s1359-6454\(96\)00375-8](https://doi.org/10.1016/s1359-6454(96)00375-8).
- [178] C. G. Shull and M. K. Wilkinson.
In: Physical Review 97 (2 1955), pp. 304–310. DOI: [10.1103/PhysRev.97.304](https://doi.org/10.1103/PhysRev.97.304).
URL: <https://link.aps.org/doi/10.1103/PhysRev.97.304>.
- [179] J. R. G. da Silva and R. B. McLellan.
In: Materials Science and Engineering 26.1 (Nov. 1976), pp. 83–87.
DOI: [10.1016/0025-5416\(76\)90229-9](https://doi.org/10.1016/0025-5416(76)90229-9).
URL: [https://doi.org/10.1016/0025-5416\(76\)90229-9](https://doi.org/10.1016/0025-5416(76)90229-9).
- [180] D. Simonovic et al. In: Physical Review B 81.5 (Feb. 2010).
DOI: [10.1103/physrevb.81.054116](https://doi.org/10.1103/physrevb.81.054116).
URL: <https://doi.org/10.1103/physrevb.81.054116>.
- [181] S. W. J. Smith, W. White, and S. G. Barker. In:
Proceedings of the Physical Society of London 24.1 (Dec. 1911), pp. 62–69.
DOI: [10.1088/1478-7814/24/1/310](https://doi.org/10.1088/1478-7814/24/1/310).
URL: <https://doi.org/10.1088/1478-7814/24/1/310>.
- [182] L. Stork et al.
In: Zeitschrift für Naturforschung B 65.10 (2010), pp. 1235–1239.
DOI: [doi:10.1515/znb-2010-1009](https://doi.org/10.1515/znb-2010-1009).
URL: <https://doi.org/10.1515/znb-2010-1009>.
- [183] J. Takahashi et al. In: Tetsu-to-Hagane 93.2 (2007), pp. 145–149.
DOI: [10.2355/tetsutohagane.93.145](https://doi.org/10.2355/tetsutohagane.93.145).
URL: <https://doi.org/10.2355/tetsutohagane.93.145>.
- [184] K. Takai and R. Watanuki. In: ISIJ International 43.4 (2003), pp. 520–526.
DOI: [10.2355/isijinternational.43.520](https://doi.org/10.2355/isijinternational.43.520).
URL: <https://doi.org/10.2355/isijinternational.43.520>.
- [185] Y. N. Taran and A. M. Nesterenko.
In: Metal Science and Heat Treatment 19.11 (1977), pp. 970–973.
- [186] <https://thermocalc.com/>. Accessed: 2010-12-20.
- [187] R. C. Thomson and M. K. Miller.
In: Acta Materialia 46.6 (Mar. 1998), pp. 2203–2213.
DOI: [10.1016/s1359-6454\(97\)00420-5](https://doi.org/10.1016/s1359-6454(97)00420-5).
URL: [https://doi.org/10.1016/s1359-6454\(97\)00420-5](https://doi.org/10.1016/s1359-6454(97)00420-5).
- [188] R. C. Thomson and M. K. Miller.
In: Applied Surface Science 87-88 (Mar. 1995), pp. 185–193.
DOI: [10.1016/0169-4332\(94\)00496-x](https://doi.org/10.1016/0169-4332(94)00496-x).
URL: [https://doi.org/10.1016/0169-4332\(94\)00496-x](https://doi.org/10.1016/0169-4332(94)00496-x).
- [189] A. Togo and I. Tanaka. In: Scripta Materialia 108 (Nov. 2015), pp. 1–5.
DOI: [10.1016/j.scriptamat.2015.07.021](https://doi.org/10.1016/j.scriptamat.2015.07.021).
URL: <https://doi.org/10.1016/j.scriptamat.2015.07.021>.

- [190] L. Toth. In: Transition Metal Carbides and Nitrides. Elsevier Science, 2014. ISBN: 9780323157223.
URL: <https://books.google.fr/books?id=BPQgk0ufPHIC>.
- [191] A. Tsuzuki et al.
In: Journal of Materials Science 19.8 (Aug. 1984), pp. 2513–2518.
DOI: 10.1007/bf00550805. URL: <https://doi.org/10.1007/bf00550805>.
- [192] A. L. Udovsky and D. A. Vasilyev.
In: Journal of Physics: Conference Series 1658 (Oct. 2020), p. 012066.
DOI: 10.1088/1742-6596/1658/1/012066.
URL: <https://doi.org/10.1088/1742-6596/1658/1/012066>.
- [193] A. I. Ul'yanov et al.
In: The Physics of Metals and Metallography 115.5 (May 2014), pp. 437–445.
DOI: 10.1134/s0031918x14050123.
URL: <https://doi.org/10.1134/s0031918x14050123>.
- [194] M. Umemoto, Silvio E. Kruger, and Hideyuki Ohtsuka.
In: Materials Science and Engineering: A 742 (Jan. 2019), pp. 162–168.
DOI: 10.1016/j.msea.2018.10.115.
URL: <https://doi.org/10.1016/j.msea.2018.10.115>.
- [195] M. Umemoto et al. In: Scripta Materialia 45.4 (Aug. 2001), pp. 391–397.
DOI: 10.1016/s1359-6462(01)01016-8.
URL: [https://doi.org/10.1016/s1359-6462\(01\)01016-8](https://doi.org/10.1016/s1359-6462(01)01016-8).
- [196] M Umemoto et al.
In: Metallurgical and Materials Transactions A 32.8 (2001), pp. 2127–2131.
- [197] Unknown. In: Note Technique, IRSN (2015).
- [198] Unknown. In: Note Technique, ASN (2017).
- [199] Unknown. In: Note Technique, IRSN (2015).
- [200] T. A. Velikanova et al.
In: Powder Metallurgy and Metal Ceramics 50.7 (2011), pp. 442–451.
- [201] B. Vieillard-Baron and Y. Meyzaud.
In: Techniques de l'ingénieur. Génie nucléaire (1998).
- [202] E. Vincent, C. S. Becquart, and C. Domain.
In: Nuclear Instruments and Methods in Physics Research Section B 228.1-4 (Jan. 2005), pp. 137–141. DOI: 10.1016/j.nimb.2004.10.035.
URL: <https://doi.org/10.1016/j.nimb.2004.10.035>.
- [203] G. H. Vineyard.
In: Journal of Physics and Chemistry of Solids 3.1-2 (Jan. 1957), pp. 121–127.
DOI: 10.1016/0022-3697(57)90059-8.
URL: [https://doi.org/10.1016/0022-3697\(57\)90059-8](https://doi.org/10.1016/0022-3697(57)90059-8).
- [204] A. Vojvodic. In: Catalysis Letters 142.6 (Apr. 2012), pp. 728–735.
DOI: 10.1007/s10562-012-0820-6.
URL: <https://doi.org/10.1007/s10562-012-0820-6>.
- [205] J. Von Appen, B. Eck, and R. Dronskowski.
In: Journal of computational chemistry 31.14 (2010), pp. 2620–2627.
- [206] D. Walker et al.
In: American Mineralogist 100.11-12 (Nov. 2015), pp. 2610–2624.
DOI: 10.2138/am-2015-5306.
URL: <https://doi.org/10.2138/am-2015-5306>.

- [207] C. S. Wang, B. M. Klein, and H. Krakauer.
In: *Physical Review Letters* 54 (16 Apr. 1985), pp. 1852–1855.
DOI: [10.1103/PhysRevLett.54.1852](https://doi.org/10.1103/PhysRevLett.54.1852).
URL: <https://link.aps.org/doi/10.1103/PhysRevLett.54.1852>.
- [208] T. Wang et al. In: *Surface Science* 651 (Sept. 2016), pp. 195–202.
DOI: [10.1016/j.susc.2016.04.017](https://doi.org/10.1016/j.susc.2016.04.017).
URL: <https://doi.org/10.1016/j.susc.2016.04.017>.
- [209] X. Wang, M. Yan, and H. Chen.
In: *Journal of Materials Science & Technology* 25 (2009), pp. 419–422.
- [210] C. A. Wert. In: *Physical Review* 79.4 (Aug. 1950), pp. 601–605.
DOI: [10.1103/physrev.79.601](https://doi.org/10.1103/physrev.79.601).
URL: <https://doi.org/10.1103/physrev.79.601>.
- [211] D. G. Westlake.
In: *Journal of the Less Common Metals* 107.2 (1985), pp. 189–202.
ISSN: 0022-5088. DOI: [https://doi.org/10.1016/0022-5088\(85\)90078-5](https://doi.org/10.1016/0022-5088(85)90078-5).
URL: <https://www.sciencedirect.com/science/article/pii/0022508885900785>.
- [212] G. K. Williamson and R. E. Smallman.
In: *Acta Crystallographica* 6.4 (Apr. 1953), pp. 361–362.
DOI: [10.1107/s0365110x5300096x](https://doi.org/10.1107/s0365110x5300096x).
URL: <https://doi.org/10.1107/s0365110x5300096x>.
- [213] I. G. Wood et al.
In: *Journal of Applied Crystallography* 37.1 (Jan. 2004), pp. 82–90.
DOI: [10.1107/s0021889803024695](https://doi.org/10.1107/s0021889803024695).
URL: <https://doi.org/10.1107/s0021889803024695>.
- [214] T. Xiao et al.
In: *Journal of Materials Chemistry* 11.12 (Oct. 2001), pp. 3094–3098.
DOI: [10.1039/b104011c](https://doi.org/10.1039/b104011c). URL: <https://doi.org/10.1039/b104011c>.
- [215] J.-P. Yang et al.
In: *Journal of Central South University* 23.9 (Sept. 2016), pp. 2173–2181.
DOI: [10.1007/s11771-016-3274-y](https://doi.org/10.1007/s11771-016-3274-y).
URL: <https://doi.org/10.1007/s11771-016-3274-y>.
- [216] Y. Yang et al.
In: *Physical Chemistry Chemical Physics* 19.48 (2017), pp. 32341–32348.
DOI: [10.1039/c7cp06598a](https://doi.org/10.1039/c7cp06598a). URL: <https://doi.org/10.1039/c7cp06598a>.
- [217] E. P. Yelsukov et al. In: *Journal of Magnetism and Magnetic Materials* 258-259 (Mar. 2003), pp. 513–515. DOI: [10.1016/s0304-8853\(02\)01129-0](https://doi.org/10.1016/s0304-8853(02)01129-0).
URL: [https://doi.org/10.1016/s0304-8853\(02\)01129-0](https://doi.org/10.1016/s0304-8853(02)01129-0).
- [218] X. Zhang et al. In: 99 (Oct. 2015), pp. 281–289.
DOI: [10.1016/j.actamat.2015.07.075](https://doi.org/10.1016/j.actamat.2015.07.075).
URL: <https://doi.org/10.1016/j.actamat.2015.07.075>.
- [219] C. T. Zhou et al.
In: *Computational Materials Science* 45.4 (June 2009), pp. 986–992.
DOI: [10.1016/j.commatsci.2009.01.002](https://doi.org/10.1016/j.commatsci.2009.01.002).
URL: <https://doi.org/10.1016/j.commatsci.2009.01.002>.

- [220] C. Zhu et al. In: Ultramicroscopy 107.9 (Sept. 2007), pp. 808–812.
DOI: [10.1016/j.ultramic.2007.02.033](https://doi.org/10.1016/j.ultramic.2007.02.033).
URL: <https://doi.org/10.1016/j.ultramic.2007.02.033>.
- [221] Jing Zhu, X. W. Wang, and Steven G. Louie.
In: Physical Review B 45 (16 Apr. 1992), pp. 8887–8893.
DOI: [10.1103/PhysRevB.45.8887](https://doi.org/10.1103/PhysRevB.45.8887).
URL: <https://link.aps.org/doi/10.1103/PhysRevB.45.8887>.